

Defect Chemistry in Alkali Peroxides and Superoxides

Von der Fakultät Chemie der Universität Stuttgart

zur Erlangung der Würde eines

Doktors der Naturwissenschaften (Dr. rer. nat.)

genehmigte Abhandlung

Vorgelegt von

Oliver Gerbig

aus Darmstadt

Hauptberichter:	Prof. Dr. J. Maier
Mitberichter:	Prof. Dr. J. Bill
Prüfungsvorsitzender:	Prof. Dr. J. van Slageren
Tag der Einreichung:	28. Februar 2014
Tag der mündlichen Prüfung:	7. Mai 2014

Max-Planck-Institut für Festkörperforschung

Stuttgart

2014

Erklärung

Die vorliegende Doktorarbeit wurde vom Autor selbst in der Abteilung von Prof. J. Maier am Max-Planck-Institut für Festkörperforschung im Zeitraum von Januar 2010 bis März 2014 angefertigt. Der Inhalt ist die eigene Arbeit des Autors, Ausnahmen sind gekennzeichnet und wurden noch nicht zur Erlangung einer Qualifizierung oder eines Titels an der einer akademischen Institution eingereicht.

Stuttgart, den 28. Februar 2014

Oliver Gerbig

Declaration

The work described in this thesis was carried out by the author in the Department of Prof. J. Maier at the Max Planck Institute for Solid State Research from January 2010 to March 2014. The content is the original work of the author except where indicated otherwise and has not been previously submitted to obtain any other degree or qualification at any academic institution.

Stuttgart, 28th February 2014

Oliver Gerbig

Table of Contents

1	Introduction and Motivation	1
1.1	Inorganic Peroxides and Superoxides	1
1.2	Solid State Defect Chemistry	4
2	Experimental	6
2.1	Powder Preparation	6
2.1.1	Lithium Peroxide.....	6
2.1.2	Sodium Peroxide	7
2.1.3	Potassium Peroxide	7
2.1.4	Potassium, Rubidium and Cesium Superoxide	8
2.2	Electrochemical Techniques	8
2.2.1	Pellet Preparation for Electrochemical Measurements	8
2.2.2	Direct Current Polarization Measurement	10
2.2.3	Electrochemical Impedance Spectroscopy.....	11
2.2.4	Conductivity Relaxation Measurement	12
2.2.5	Electromotive Force Measurement	13
2.3	Chemical, Thermal, Thermochemical, Microstructural and Magnetic Characterization Techniques	15
2.3.1	Scanning Electron Microscopy	15
2.3.2	Differential Scanning Calometry	16
2.3.3	Thermogravimetric Measurement.....	16
2.3.4	X-ray diffraction	16
2.3.5	Inductive Coupled Plasma – Optical Emission Spectroscopy	16
2.3.6	Raman Spectroscopy.....	16
2.3.7	Infrared Spectroscopy	16
2.3.8	Electron Paramagnetic Resonance Spectroscopy.....	17
2.4	Oxygen Isotope Exchange and Gas Phase Analysis	17
3	Results and Discussion	19

3.1	Lithium Peroxide	19
3.1.1	Chemical Characterization and Thermal Stability of Li_2O_2	19
3.1.2	Electrochemical characterization	23
3.1.3	Defect Chemistry	30
3.1.4	Chemical oxygen exchange kinetics in Li_2O_2	41
3.1.5	Li_2O_2 -Au composite	42
3.2	Sodium Peroxide	44
3.2.1	Chemical characterization and Crystallographic Structure	44
3.2.2	Electrochemical characterization	45
3.2.3	Defect Chemistry	49
3.3	Potassium Peroxide	52
3.3.1	Chemical characterization	52
3.3.2	Thermodynamic Stability of K_2O_2	53
3.3.3	Electrochemical characterization	54
3.4	Potassium Superoxide	58
3.4.1	Chemical characterization and Crystallographic Structure	58
3.4.2	Electrochemical characterization	59
3.5	Rubidium and Cesium Superoxide	68
3.5.1	Chemical Characterization, Thermodynamic Stability and Crystallographic Structure	68
3.5.2	Electrochemical Characterization	71
3.6	Electromotive Force Measurements of Alkali Superoxides	74
3.7	Oxygen Isotope Exchange	78
3.8	Concluding Discussion	85
4	Summary	90

Zusammenfassung

Während Bildung und Transport von Punktdefekten in Oxiden an vielen Beispielen untersucht wurde, ist die Defektchemie der Metall-Peroxide und Superoxide praktisch unbekannt. Diese Thematik ist sowohl von grundlegendem Interesse (was sind die relevanten Ladungsträger, ergeben sich durch die Peroxid- und Superoxidionen Unterschiede zu Oxiden etc.) als auch von technologischer Bedeutung für neuartige elektrochemische Energiespeicher.

Bei der elektrischen Entladung von Alkalimetall-Sauerstoff-Batterien mit nicht-wässrigen Elektrolyten reagieren Sauerstoff und Alkalimetall-Ionen unter Aufnahme der Elektronen aus dem elektrischen Stromkreis zu Alkalimetallperoxiden oder -superoxiden. Im Vergleich zu herkömmlichen Alkalimetall-Ionen-Batterien, bei denen die Alkalimetall-Ionen von einem Wirtsmaterial aus üblicherweise schweren Übergangsmetalloxiden- oder phosphaten aufgenommen werden (durch Interkalation oder Phasenumwandlung), könnten deutlich höhere spezifische Energiedichten erreicht werden, die insbesondere für Elektroantriebe von Kraftfahrzeugen erforderlich sind. Da die Alkalimetallperoxide und -superoxide bei jedem Entlade- und Ladezyklus neu gebildet und wieder zersetzt werden, kommt der Transport- und Reaktionskinetik dieser Materialien eine erhebliche Bedeutung für die Leistungsfähigkeit der Batterien zu. In der vorliegenden Arbeit werden die elektrischen Transporteigenschaften, die Sauerstoffaustauschkinetik sowie die Defektchemie der Peroxide von Lithium, Natrium und Kalium sowie der Superoxide von Kalium, Rubidium und Cäsium untersucht.

Aufgrund der hohen Empfindlichkeit der Substanzen gegenüber Kohlenstoffdioxid und Wasser sowie der elektrischen Transporteigenschaften gegenüber Verunreinigungen wurde besonderes Augenmerk auf die Herstellung, Handhabung und chemische Charakterisierung (Raman-Spektroskopie, Röntgenbeugung, Infrarotspektroskopie und Atomemissionsspektroskopie) der Proben gelegt. Die Präparation erfolgt im Falle von Lithiumperoxid durch eine Fällungsreaktion einer Lithiumbase mit Wasserstoffperoxid, in den anderen Fällen durch vorsichtige Oxidation des Alkalimetalls mit Sauerstoff. Die Handhabung der Proben unter Schutzgas (Handschuhkasten) oder reinem Sauerstoff und die Verwendung von leckdichten Versuchsaufbauten sind erforderlich, um die Reaktion zu Karbonaten und Hydroxiden zu unterbinden.

Zur elektrochemischen Charakterisierung wurden Presslinge hergestellt und ionisch blockierende Elektroden (Titan, Gold, Platin) durch Kathodenzerstäubung aufgebracht. Die elektrische Leitfähigkeit der Materialien wurde mittels Impedanzspektroskopie und Stöchiometriepolarisation mit Gleichstrom in ihre ionische und elektronischen Anteile zerlegt. Aus dem transienten Verhalten der Stöchiometriepolarisation ließ sich außerdem der chemische Diffusionskoeffizient (ambipolare Diffusion von ionischen und elektronischen Ladungsträgern) gewinnen. Die

Sauerstoffpartialdruckabhängigkeit der elektronischen Leitfähigkeit gibt Aufschluss über die elektronischen Majoritätsträger. Für die Alkalimetall-Peroxide ergibt sich eine zunehmende elektronische Leitfähigkeit mit zunehmendem Sauerstoffpartialdruck gemäß einer p-Leitung. Mit Hilfe der Elektronenspinresonanzspektroskopie können Superoxidionen als Defektspezies in den Peroxiden identifiziert werden. Dieser Defekt lässt sich als ein an einem regulären Peroxid-Platz lokalisiertes Defektelektron (Loch) veranschaulichen. Der wahrscheinlichste elektronische Leitungsmechanismus ist daher der Sprung eines solchen Defektelektrons zu einem benachbarten Peroxid-Ion. Das genau umgekehrte Bild ergibt sich für die Alkalimetall-Superoxide. Hier zeigt die zunehmende elektronische Leitfähigkeit mit abnehmendem Sauerstoffpartialdruck auf einen n-Leitfähigkeit an. Die Überschusselektronen sind am wahrscheinlichsten an Superoxid-Ionen gebunden und bilden Peroxidionen als Defektspezies im Material.

Die ionischen Majoritätsladungsträger lassen sich in Lithiumperoxid durch die Verwendung von Elektroden aus Lithium-Aluminium | Lithiumiodid (reversibel für Kationen, polarisierend für Anionen) dem Lithiumionen-Teilgitter zu ordnen. Für den Transport der Kationen ergibt sich aus der Erhöhung der ionischen Leitfähigkeit mit zunehmendem Gehalt an Donoratomen ein Leerstellenmechanismus. Die relativ hohen Aktivierungsenergien für ionischen und elektronischen Transport erklären sich durch Berücksichtigung von Assoziaten aus Lithiumionenleerstellen und Donoren sowie Lithiumionenleerstellen und Löchern. Auf der Grundlage der Ergebnisse wird ein defektchemisches Modell vorgeschlagen und diskutiert. Die Abhängigkeiten der Defektkonzentrationen vom Sauerstoffpartialdruck bzw. von der Alkalimetallaktivität werden abgeleitet und als sogenannte Kröger-Vink-Diagramme graphisch dargestellt.

Die ionische Leitfähigkeit zeigt im Falle von Rubidiumsperoxid, Cäsiumsuperoxid sowie getempertem Kaliumsuperoxid eine starke negative Abhängigkeit vom Sauerstoffpartialdruck. Gemäß dem vorgeschlagenen Defektmodells für die Alkalimetall-Superoxide ist dieses Verhalten für den Transport entweder von Alkalimetall-Zwischengitterionen oder von Superoxid-Leerstellen zu erwarten ist. In diesem Zusammenhang sind weitere Arbeiten, beispielsweise unter Verwendung von Elektroden die selektiv nur Anionen oder Kationen blockieren notwendig, um die Frage der ionischen Majoritätsladungsträger abschließend zu klären.

Der Sauerstoffaustausch der Alkaliperoxide und -superoxide wurde durch Sauerstoff-Isotopenaustausch mit anschließender Analyse der Gasphasenzusammensetzung mittels Massenspektrometer untersucht. In Lithiumperoxid, Natriumperoxid sowie Kaliumsuperoxid erfolgt der Sauerstoffaustausch maßgeblich unter Brechung der kovalenten Sauerstoffbindung. Dabei wird die Austauschkinetik mit zunehmendem Kationenradius deutlich schneller. Hingegen ermöglicht die hohe Polarisierbarkeit der Kationen im Cäsiumsuperoxid sogar den Einbau und den Volumentransport von Sauerstoff unter Beibehaltung der kovalenten Bindung. Aus der Sauerstoffisotopenrelaxation

lassen sich der Diffusionskoeffizient des Superoxids sowie eine Untergrenze für die Sauerstoffaustauschreaktionsrate bestimmen. Während die Diffusion im Vergleich zu Sauerstoffelektrolyten wie Yttrium-dotiertem Zirkonoxid langsam verläuft, ist die Oberflächenreaktion in Cäsiumsuperoxid verglichen mit hochdotierten Kathodenmaterialien für Hochtemperatur-Brennstoffzellen sehr schnell.

Die erhöhte Austauschkinetik der Alkalimetall-Superoxide mit der Gasphase – die lediglich den Transfer eines Elektrons sowie die Vernichtung einer Superoxid-Leerstelle, jedoch nicht die Brechung der kovalenten Bindung des molekularen Sauerstoffs erfordert – ermöglicht auch die Messung der elektromotorischen Kraft (EMK) durch Unterschiede im Sauerstoffpartialdruck bei vergleichsweise niedrigen Temperaturen $< 200\text{ °C}$. EMK-Messungen an den Superoxiden sind ferner eine geeignete Methode, um die elektronische Leitfähigkeit und ihre Abhängigkeit vom Sauerstoffpartialdruck zu bestimmen.

Zusammenfassend lässt sich festhalten, dass in der vorliegenden Arbeit die Defektchemie für eine Reihe von Metall-Peroxiden und Superoxiden systematisch und im Detail untersucht wurde. Hierbei wurden auch Transportgrößen wie die elektronische und ionische Leitfähigkeit, Diffusionskoeffizienten und Oberflächenreaktionsraten bestimmt sowie Transportmechanismen aufgeklärt. Diese Ergebnisse sind einerseits von grundlegendem Interesse aber auch hochgradig relevant für das Verständnis und die Entwicklung von neuartigen elektrochemischen Energiespeichern.

Abstract

While the formation and transport of point defects of oxide materials have been well investigated on numerous examples, the defect chemistry of metal peroxides and superoxides is largely unknown so far. This subject is of fundamental interest (what are the relevant charge carriers, exist differences compared to oxides etc.) but also of technological relevance for novel electrochemical energy storage systems.

During the discharging of the alkali metal oxygen battery based on non-aqueous electrolytes, oxygen takes up electrons from the electric circuit and reacts with alkali metal ions to alkali metal peroxides or superoxides. Compared to conventional alkali metal ion batteries with heavy transition metal oxides or phosphates as host material for the alkali metal (either by intercalation or phase transformation), much higher specific energy densities, which are in particular necessary for electric vehicles, can potentially be achieved in these batteries. The transport and reaction kinetics is particularly relevant for the performance of these energy storage systems, since the alkali metal peroxides and superoxides are formed and decomposed again at every charge-discharge cycle. The present thesis investigates the electrical transport properties, the oxygen exchange kinetics and the defect chemistry of the peroxides of the lithium, sodium and potassium as well the superoxides of potassium, rubidium and cesium.

Due to the high sensitivity a) of the materials towards carbon dioxide and water and b) of the electrical transport properties towards impurities, special attention was paid to the preparation, the treatment and the chemical characterization (Raman spectroscopy, x-ray diffraction, infrared spectroscopy, atomic emission spectroscopy) of the samples. The preparation of lithium peroxide is carried out by precipitating a lithium base with hydrogen peroxide. The other peroxides and superoxides were prepared by careful oxidation of the corresponding alkali metal with oxygen. The samples have to be handled under inert gas (glove box) or pure oxygen and leakage free setups have to be employed to avoid the reaction to carbonates and hydroxides.

For the electrochemical characterization, pellets were pressed from the sample powders and contacted with ionically blocking electrodes (titanium, gold, platinum) by dc magnetron sputtering. The electrical conductivity of the materials was separated into its ionic and electronic contributions by electrochemical impedance spectroscopy and dc stoichiometry polarization. Furthermore, the chemical diffusivity (ambipolar diffusion of ionic and electronic charge carriers) was determined from the transient behavior of the stoichiometry polarization relaxation curve. The oxygen partial pressure dependence of the electronic conductivity sheds light on the majority electronic carrier. The increase of the electronic conductivity upon increasing pO_2 provides evidence for p-type conduction. With electron spin resonance spectroscopy, it is possible to identify superoxide ions as defects in the

peroxides. This defect can be seen as a defect electron (hole) trapped on a regular peroxide site. Accordingly, the most probable electronic transport mechanism is the hopping of such a trapped defect electron to a neighbouring peroxide ion. The exactly inversed situation can be considered for the alkali metal superoxides. The increasing electronic conductivity with decreasing pO_2 suggests n-type conductivity. The excess electrons are most likely trapped by superoxide ions and form peroxide ions as defects in the material.

The main ionic charge carrier in lithium peroxide can be assigned to the cation sub-lattice by investigating cells with electrodes of lithium-aluminium | lithium iodide (which are reversible for lithium, but polarizing for oxygen species). Since the ionic conductivity is increasing with increasing donor content, the lithium transport can be considered to proceed via a vacancy mechanism. The relatively high activation energies of ionic and electronic transport are explained if the formation of associates of lithium vacancies and donor impurities as well as of lithium vacancies and holes are taken into account at the low measurement temperatures. Based on the results, a defect chemical model is proposed and discussed. The dependence of the defect concentration on the oxygen partial pressure and alkali metal activity respectively are derived and graphically illustrated as so called Kröger-Vink diagrams.

The ionic conductivity exhibits a pronounced negative pO_2 dependence in the case of rubidium and cesium superoxide as well as annealed potassium superoxide. According to the proposed defect model for alkali metal superoxides, this corresponds either to the transport of alkali metal interstitial ions and/or superoxide vacancies. Further experiments employing selectively cation or anion blocking electrodes will be necessary to distinguish between these defects and determine the main ionic charge carrier in alkali superoxides.

The oxygen exchange in alkali peroxides and superoxides was studied by oxygen isotope exchange and analysis of the gas phase composition by mass spectrometry. In lithium and sodium peroxide as well as in potassium superoxide, the oxygen exchange proceeds mainly by breaking the covalent oxygen bond. The exchange kinetics is accelerated with increasing cation size. In contrast, the high polarizability in cesium superoxide allows the incorporation and bulk transport of molecular oxygen as a unit without breaking the oxygen-oxygen bond. The chemical diffusivity of the superoxide and a lower limit of the oxygen exchange rate constant can be extracted from the relaxation of the oxygen isotope composition in the gas phase. While the superoxide diffusion is rather slow compared to oxygen electrolytes such as yttrium doped zirconia, the surface reaction turns out to be extremely fast compared to highly doped cathode materials employed in solid oxide fuel cells.

The enhanced oxygen exchange kinetics of the alkali metal superoxides – which requires only the transfer of an electron and the annihilation of a superoxide vacancy, but no bond breaking – also enables the measurement of the electromotive force (EMF) caused by differences in the oxygen

partial pressure at comparable low temperatures of $< 200\text{ }^{\circ}\text{C}$. It was further shown that the EMF method is suitable to determine the dependence of the electronic conductivity on the oxygen partial pressure in alkali superoxides.

To summarize, the present thesis is the first systematic and detailed investigation of the defect chemistry of a number of metal peroxides and superoxides. Transport properties such as electronic and ionic conductivity, diffusivity and surface reaction rate constants were determined and transport mechanism were identified. On the one side, these results are considered as fundamentally interesting, but they are also highly relevant for the understanding and development of novel electrochemical energy storage systems.

1 Introduction and Motivation

1.1 Inorganic Peroxides and Superoxides

Inorganic peroxides and superoxides are ionic solids containing metal cations and the oxygen species O_2^{2-} and O_2^- . The energy level diagrams of the latter species can be derived from that of O_2 according to molecular orbital theory by filling the antibonding π^*_{2p} by one (superoxide) or two (peroxide) more electrons (Figure 1.1). Accordingly, the intramolecular bond strength decreases from O_2 to O_2^- to O_2^{2-} which can be seen by the decrease of the stretch vibration frequency probed by Raman spectroscopy. Only the most electropositive metals (namely, those with the electronegativity < 1 according to Pauling's scale^[1]) are known to form pure bulk peroxides: the alkaline earth metals strontium and barium and the alkali metals (discarding the radioactive francium). The reported peroxide phases of calcium, magnesium and the group II b metals zinc, cadmium and mercury are heavily contaminated by water and hydroxide. Pure superoxides have only been prepared so far as bulk materials with the alkali metals heavier than lithium.^{[2]-[4]}

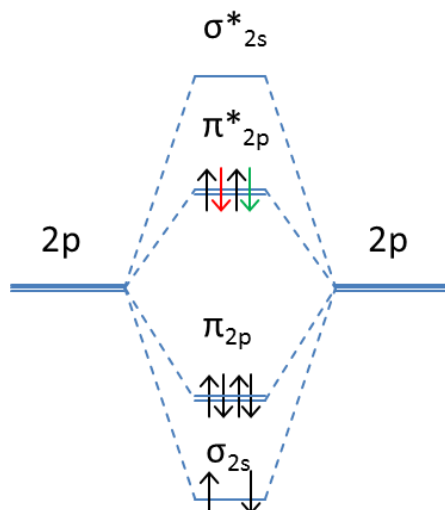


Figure 1.1: Energy levels of molecular oxygen formed by the 2p orbitals according to molecular orbitals theory and occupation of electrons in molecular oxygen (black), superoxide (oxygen occupation plus red) and peroxide (superoxide occupation plus green).

The focus of research on inorganic peroxides and superoxides was mainly triggered by technological advances and interests. After the discovery of the metal peroxides in the 19th century, barium peroxide was studied and employed for oxygen generation (Brin process)^{[5],[6]} – until it became

obsolete by the development of the more economic fractionation of liquid air. The invention and development of x-ray diffraction techniques enabled the structure determination of barium and strontium peroxide (1935)^[7], potassium superoxide (1936)^[8], rubidium and cesium superoxide (1939)^[9], sodium superoxide (1950)^[10] and finally the alkali peroxides (1957)^{[11],[12]}.

In the 1960s, the ability of alkali peroxides and superoxides to trap carbon dioxide and release oxygen raised their interest for air regeneration in spacecraft and nuclear powered submarines.^{[13]-[18]} Potassium superoxide was already employed in personal breathing apparatuses for naval vessels since World War 2.^[19] After the 1970s energy crisis, the thermodynamics and kinetics of the barium peroxide/oxide couple was reinvestigated for the purpose of chemical energy storage.^[20] Kinetic aspects of the formation of barium peroxide were also addressed in the context of the extensively studied field of oxide thermionic cathodes.^[21]

Further research on the thermodynamic properties and decomposition kinetics of barium peroxide was conducted in the 1990s due to its use as precursor in the preparation of the previously found high T_c superconductors.^{[22]-[25]} The reaction of lithium, potassium and cesium with molecular oxygen to superoxide and peroxide thin films at low temperatures was also studied in this context.^[26] Moreover, thin films of cesium superoxide and peroxide were grown and investigated by various spectroscopic techniques due to their function in the activation of group III-V semiconductors as photocathodes.^{[27] [28]}

Beginning with 1980s, the prospect to refine the abundant methane by oxidative coupling in particular to ethane initiated research of the role of peroxide and superoxide species on the surface of metal oxide catalysts in various reactions: the oxidative coupling of methane to ethane and ethene on alkali and alkaline earth peroxides^{[29]-[32]} and alkaline earth-transition metal oxides^{[33]-[37]}, the oxidation of methane to methanol on iron-aluminum-lead oxide^[38], the oxidative dehydrogenation of butane on alkali and alkaline earth promoted nickel-molybdenum oxide^[39], the decomposition of nitric oxide on barium oxide^{[40],[41]} and titanate^[42], the oxidative dehydrogenation of ethane on strontium chloride/lanthanum oxide^[43] and the combustion of soot on metal oxides^{[44]-[46]}.

Most recently, the demands for high energy density storage systems in particular for automotive applications opened a new field of research involving alkali peroxides and superoxides: the reversible non-aqueous alkali oxygen battery based on the earlier work of Abraham and Ziang.^[47] In this electrochemical storage system, the alkali metal is stored at a high electrical potential in a high energy density anode. Upon discharging the cell, the alkali ions diffuse through the non-aqueous electrolyte, react with molecular oxygen and electrons from the outer electrical circuit to form alkali peroxides or superoxides at the cathode (with $n = 1$ for superoxide and $n = 2$ for peroxide formation):



So far, electrochemical cells working according to equation (1) with $M = \text{lithium}$ and $n = 2$ ^[48], $M = \text{sodium}$ and $n = 1$ ^[49], 2 ^[50] and $M = \text{potassium}$ and $n = 1$ ^[51] have been found and explored. With lithium (the lightest metal in the periodic table), the theoretical specific energy density of the active material in the Li-O₂ battery (with lithium metal as anode) amounts to 3,457 Wh/kg in the discharged state (with $n = 2$, i.e. peroxide formation) exceeding that of conventional lithium ion intercalation batteries (with lithium intercalated graphite as anode) by an order of magnitude. Given the low tank to wheel efficiency of combustion engines, the lithium oxygen battery – if its major problems of rapid O₂ uptake from the atmosphere while keeping out H₂O and CO₂, sluggish kinetics of the cathodic reaction and electrolyte decomposition are solved – may have the potential to compete with gasoline (13,000 Wh/kg) in terms of the practical energy density.^[52]

In any case, this topic of lithium oxygen battery technology stimulated experimental research of formation and decomposition of Li₂O₂^{[53]-[58]} as well as a series of theoretical studies and calculations on the thermodynamics^{[59]-[65]} and the transport and reaction kinetics^{[66]-[72]} of Li₂O₂. However, there was no systematic experimental study of the electrical transport properties and defect chemistry in Li₂O₂ – or any other alkali metal peroxide - until it was elucidated in course of the present thesis.^[73]

The only known published conductivity data of a metal peroxide was collected unintentionally in 1958.^[74] During the investigation of the transport properties of barium and strontium oxide (as thermionic cathode coating), a positive slope was observed in the Arrhenius plot of the conductivity upon heating up barium oxide to 500 °C in 0.5 bar oxygen. The anomaly was correctly related to the phase transition to the peroxide, which readily takes place under these conditions. More recently, a pronounced oxygen nonstoichiometry - whereby oxide defects occupy regular peroxide sites - was observed in barium and strontium peroxide by means of x-ray diffraction of single crystals. The loss of oxygen leads also to a shortening of the covalent peroxide bond and a shift of the O₂²⁻ stretch vibration to higher frequencies in the Raman spectrum.^[75] But a systematic investigation of the defect chemistry of these alkaline earth peroxides was beyond the scope of these studies and no further research was conducted. As far as alkali superoxides are concerned, dc conductivity of potassium superoxide was reported in ref. ^[76]. However, the conductivity data seems seriously flawed and is about 16 orders of magnitude higher than what is found in the present work.

Owing to the scarce knowledge of the electrical transport properties and the underlying defect chemistry of inorganic peroxides and superoxides and its significance in particular for research and development of rechargeable alkali-oxygen batteries, the present work aims of providing insight into this issue. Electrochemical techniques such as electrochemical impedance spectroscopy, dc polarization measurements, conductivity relaxation and electromotive force measurements are powerful tools to probe the transport and reaction properties and were extensively employed in this study.

As the commercially available powders of sodium and lithium peroxide and of potassium superoxide are heavily chemically contaminated by 3 to 10 wt.% of carbonate and hydroxide (the heavier alkali peroxides and superoxides are not even commercially available) and since the knowledge and control of defects is important for the electrochemical characterization (see also next section 1.2 Solid State Defect Chemistry), considerable effort was put into the preparation and chemical characterization of the inorganic peroxides and superoxides. The task was complicated by the extremely high reactivity of the compounds towards moisture and CO_2 and necessity to work under inert gas conditions or highly pure oxygen.

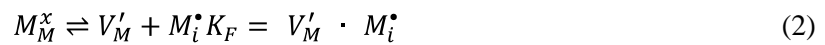
1.2 Solid State Defect Chemistry

The perfectly ordered solid state has the lowest enthalpy and is the stable state at absolute zero ($T = 0$ K). However, at temperatures $T > 0$ K, in thermodynamic equilibrium the contribution of the configurational entropy introduces disorder in materials. The energy required to form point defects (e.g. vacancies, interstitials) is outweighed by the entropy gain. Point defects— though small in concentrations – are therefore always present in thermodynamic equilibrium in solids.^[77] In addition to this, non-equilibrium defects exist in real materials. Such frozen-in imperfections were introduced into the solid under different conditions (e.g. at higher temperatures and different chemical environments, by external forces) and the kinetics is too slow to remove them under the conditions considered. For instance, in ceramics dislocations (lines of point defects, i.e. one dimensional defects) are known to form at high temperatures and by shear forces and to remain in the material even at elevated temperatures as a large number of atoms needs to be displaced (requiring very high mobilities of the constituents of the crystal) to heal them out.

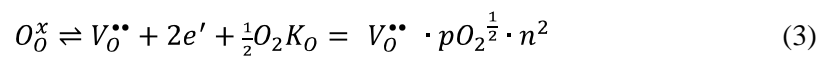
For the treatment of many physical properties such as density and heat capacity, the presence of diluted defects bears little relevance and can be usually neglected. However, other important properties, in particular those involving charge and mass transport, depend very sensitively on the kind of defects and their concentrations, because these are the centers for transport and reaction. For example, the motion of atoms in a crystalline solid is determined by the motion of defects in the lattice. Phenomena such as diffusion, electrical conduction and reaction kinetics are closely related to defect concentrations and mobilities in the material and their study provides insight into the underlying defect chemistry. Vice versa, understanding the defect chemistry of a material provides the basis for rationally improving its properties and coping with problems related to transport and reaction.

The basic native atomic imperfections are vacancies, interstitials and anti-site defects. In binary ionic compounds, the anti-site defect bears no relevance as it is subjected to a large energy penalty because of electrostatic repulsion. A further consequence of ionic bonds is that the condition of charge neutrality couples the population of the anion and cation defects. At a fixed stoichiometry, the intrinsic formation of a vacancy occurs either simultaneously with the formation of an interstitial in the same sub-lattice (Frenkel reaction for cations, Anti-Frenkel reaction for anions) or together with the formation of a vacancy in the counter-ion sub-lattice (Schottky reaction).

In solid state defect chemistry, the individual structure elements of the solid are described according to the Kröger-Vink notation: the species is denoted by its symbol in the periodic system, by V in case of an atomic vacancy and by e and h in case of electrons and holes, the site occupied by the species under consideration is indicated in the subscript (i for interstitial) and the charge of the species relative to the perfect lattice (‘ for positive, • for negative, x for neutral) is given in the superscript.^[78] The formation and reaction of defects can then be expressed as chemical reactions with the corresponding mass action laws (with concentrations instead of activities for diluted defects). The conditions of mass and site balance and electroneutrality have to be fulfilled in the equations. For example, the Frenkel reaction (simultaneous formation of a vacancy and interstitial defect) in the sublattice of a singly charged cation and the corresponding mass action law are expressed as follows:



The interaction of the solid with the surroundings establishes the external defect equilibria (i.e. oxygen exchange reaction for oxygen ion compounds) and deviations from the perfect stoichiometry (e.g. $MO_{1-\delta}$). The oxygen deficiency is increased with increasing temperature because of the positive entropy for the oxygen excoorporation reaction in oxide materials:



The concentration of electrons and holes are denoted by n and p.

Extrinsic defects are foreign atoms accommodated in the host lattice. The defect chemical and also technological most interesting and important case is when the imperfection is electrically charged relative to the perfect lattice (“aliovalent”) and thereby is responsible for changes in the concentration of ionic or electronic defects to compensate its charge. While the presence of chemical impurities is undesired when studying the intrinsic properties of a compound, chemical doping is intentionally employed in order to tune the transport and reaction properties of materials. Examples are p- and n-type doping of the semiconductor silicon with boron and phosphor or the increase of the oxygen vacancy concentration (and thus oxide ion transport) in yttria doped zirconium oxide.

2 Experimental

2.1 Powder Preparation

Generally, alkali peroxides and superoxides are very reactive with CO_2 and H_2O already at room temperature. The reactivity increases with increasing atomic mass and basicity of the cation as well as from the peroxide to the superoxide. Li_2O_2 is the most stable of these compounds and its fine powder is converted into carbonate and hydroxide within hours in air, but the heavier alkali peroxides as well as the superoxides react more readily within seconds (CsO_2) to few minutes (Na_2O_2). Therefore, most sample preparations, manipulations and measurements were carried out under CO_2 and H_2O free atmospheres^a. Figure 2.1 shows various sample powders sealed in glass capillaries. The alkali peroxides powders are white to ivory. In contrast, the alkali superoxide powders show optical absorption in the blue range of the visible spectrum and therefore appear bright (KO_2) to dark (CsO_2) yellow.

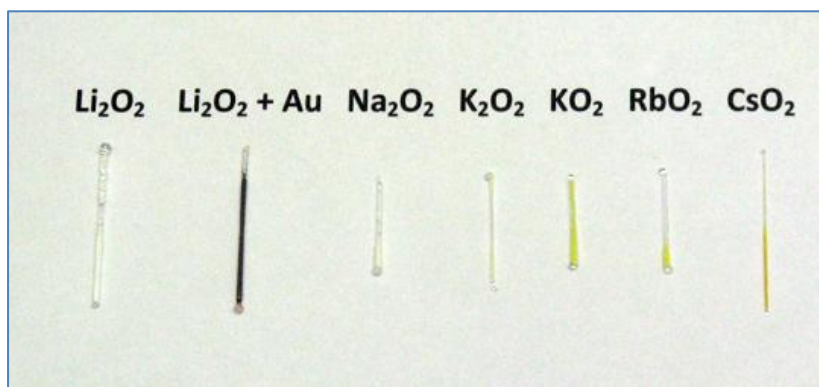


Figure 2.1: Photograph of the samples powders.

Ball milling was carried out without further additive with ZrO_2 media enclosed in a gas-tight steel vessel under argon for 1 h with 200 rpm (Fritsch Pulverisette 5 planetary mill).

2.1.1 Lithium Peroxide

0.25 g lithium metal foil (99.5% metals basis, Alfa Aesar) ripped into ca. 5 x 5 mm pieces was slowly dissolved in 30 ml dry methanol in a glove bag under argon flow. The reaction is strongly exothermic and the solution was allowed to cool down to room temperature prior proceeding further. A slightly overstoichiometric amount of aqueous 30 wt% H_2O_2 (ACS grade, Acros Organics or Fisher Scientific, unstabilized, stored in a refrigerator) was added to the lithium methanolate solution and the resultant precipitate consisting of $\text{Li}_2\text{O}_2 \cdot \text{H}_2\text{O}_2 \cdot n\text{H}_2\text{O}$ ($n = 2 - 3$)^[2] was filtered with a glass frit (porosity 5)

^a With the following exceptions: Preparation of Li_2O_2 hydrate, transfer of samples into the setup for thermogravimetric measurements, transfer of samples to the scanning electron microscope and elemental analysis with ICP-OES.

employing a rough vacuum (still in the glove bag). The dehydration to the nominally dry lithium peroxide was carried out in an Al_2O_3 crucible in a gas tight quartz setup heated to 150 °C in a tube furnace in vacuum (rotary pump with 10^{-3} mbar end pressure). The dehydrated white powder was further annealed in 1 bar pO_2 at 185 °C.

The Li_2O_2 hydrate can be obtained more simply via precipitation with H_2O_2 from a solution or slurry of LiOH in methanol instead of LiCH_3O , but the latter method enabled the dissolution of $\text{Mg}(\text{CH}_3\text{O})_2$ in the methanolic solution for donor doping experiments. The route proposed in ref. ^[79] of dissolving LiOH in boiling ethanol turned out to be unfeasible, as LiOH is barely soluble in pure, dry ethanol. The most efficient preparation method is using distilled water as solvent for LiOH , adding overstoichiometric amounts of 30% H_2O_2 and evaporating the water at rough vacuum and elevated temperatures (rotational evaporator). The route was used in this study for preparing large amounts of powder needed for isotope exchange experiments, but was considered not suitable for the preparation of doped samples for conductivity measurements, as any excess dopant not incorporated into the lithium peroxide lattice unavoidably remains in the sample powder as an undesired secondary phase. To prepare donor doped samples of Li_2O_2 , 1-5 wt.% of $\text{Mg}(\text{CH}_3\text{O})_2$ and LiCl were added to methanolic solution prior precipitating with H_2O_2 . The precipitate was washed with dry methanol.

The attempts to prepare Li_2O_2 directly via the oxidation of lithium metal or the oxidation of lithium oxide (both in pure 1 bar pO_2 and 1 bar pO_2 enriched with up to 20% ozone in the temperature range 150 to 250 °C) were not successful.

2.1.2 Sodium Peroxide

Sodium metal (99.95%, distilled, Alfa Aesar) was filled with a stainless steel scoop from its quartz ampule into an Al_2O_3 crucible in an argon filled glove box. The crucible was placed in a gas tight sample preparation setup consisting of a quartz tube connected to a stainless steel flange with thermocouple and two gas feedthroughs, and transferred to a tube furnace. The setup was flushed with 100 ml/min 20% O_2 in argon and heated to 375 °C with a heating rate of 300 °C/h. Applying higher pO_2 than 0.2 bar should be avoided as it can lead to a violent exothermic reaction, thermal runaway and cracking of the Al_2O_3 crucible and quartz tube. At the target temperature of 375 °C, the argon valve was closed and the oven turned off allowing the quartz reactor to cool down in 1 bar pO_2 . Below 100 °C, the setup was evacuated down to 10^{-3} mbar and flushed with pure argon for several times and transferred back into the glove box. This preparation method is based on ref. ^[80].

2.1.3 Potassium Peroxide

Homemade KO_2 (from potassium, Sigma Aldrich, 99.95% metal purity, stored in oil) was annealed for 20 h in an Al_2O_3 crucible at 300 °C in 10^{-4} mbar vacuum (turbomolecular pump with a rotary vane forepump). The reaction proceeds according to equation (4).



2.1.4 Potassium, Rubidium and Cesium Superoxide

The respective alkali metal (distilled Potassium, 99.95% metal purity, Sigma Aldrich; distilled Cesium, 99.98% metal purity, Alfa Aesar, distilled Rubidium, 99.75% metal purity, Alfa Aesar) was filled with a stainless steel scoop from its quartz ampule into a homemade tantalum crucible (cut and bent from a tantalum tube with 10 mm diameter and 0.5 mm wall thickness, 99.95% metal purity, WHS Sondermetalle). Note that Al_2O_3 crucibles are cracked by potassium melt already at moderate temperatures and should not be used for the heavier alkali metals. The tantalum crucible was placed into the same setup described for the Na_2O_2 preparation and transferred to a tube furnace.

In case of potassium, the setup was flushed with 100 ml/min 5% O_2 in argon and heated to 250 °C with a heating rate of 200 °C/h. At the target temperature, the valve of the argon line was closed to successively increase the pO_2 in the quartz reactor up to 1 bar. After 1 h annealing time, the setup was cooled down to room temperature and transferred into the glove box.

Rubidium and cesium react even more readily and violently with oxygen already at room temperature and special care needs to be taken to avoid a thermal runaway. The setup was evacuated and slowly flushed with oxygen using a needle valve until the surface of alkali metal is oxidized to a black-brown layer. The setup was transferred back into the glove box and the thick passivation layer was broken by scratching with a spittle or by grinding in an agate mortar. The procedure (oxygen exposure followed by grinding) was repeated until the material did not show a visible reactivity with oxygen at room temperature anymore. The powder was then annealed for 1 h at 300 °C in 1 bar oxygen to form the respective superoxide and transferred to the glove box after cooling down to room temperature.

2.2 Electrochemical Techniques

2.2.1 Pellet Preparation for Electrochemical Measurements

Cylindrical pellets were pressed from the sample powders for the electrochemical characterization. The powder was compacted for 20 s with a stainless steel pressing tool (consisting of a commercial stainless steel bore sleeve with 5 mm inner diameter and two cylindrical stainless steel stamps, which were cut from bar stocks and polished by the Crystal Preparation Group of the Max Planck Institute for Solid State Research, Stuttgart) by 200 MPa uniaxial pressure provided by a hydraulic press located in an argon glove box. Li_2O_2 samples (as well as Na_2O_2 not meant for sintering) were further subjected to 120 s of 600 MPa isostatic pressure provided by a hydraulic press located outside the

glove box using oil as pressure transmitting medium. The uniaxial pressed green pellet was sealed in two latex tubes put into each other. The inner tube served to protect the sample from air, the outer tube kept the oil from the inner tube and allowed its oil-free transfer and handling back into the glove box.

Sintering of Na_2O_2 and KO_2 is most preferably carried out on polished MgO single crystals as support, which show the least reactivity with the peroxides and superoxides at high temperatures compared to Al_2O_3 crucibles, MgO polycrystalline crucibles and also unpolished MgO single crystals. However, the adhesion of pellets on a polished surface of MgO single crystals is so poor that their transport from the glove box to the tube furnace without displacing the pellets from the single crystal to the Al_2O_3 crucible serving as support is difficult. For practical reasons, small crucibles of MgO single crystals (based on 0.5 mm thick MgO single crystals (Crystec, Berlin) with a rectangular dimple in the middle inserted by ultrasonic drilling in the metal workshop of the Max Planck Institute for Solid State Research, Stuttgart) with an unpolished surface were usually employed. Typical sintering conditions are 475 °C and 1 bar $p\text{O}_2$ for Na_2O_2 and 450 °C and 1 bar $p\text{O}_2$ for KO_2 .

Titanium, gold and platinum electrodes of 400 – 600 nm thickness were deposited on the faces of the pellets by means of dc magnetron sputtering (EMITECH K575X, modified to flange the sputter head to an argon glove box) from the respective target with a sputter current of 100 mA and a process pressure of $7 \cdot 10^{-3}$ mbar argon in the sputter head. Scanning electron microscope images of a sputtered gold film on a glass substrate are shown in Figure 2.2. The Au film appears dense, but is composed of particles with about 400 nm lateral extension. The sides of the sample pellets were polished with SiC paper after sputtering to remove electrode material reaching the sides despite the use of shadow masks (the samples could often not be perfectly aligned and covered by the mask, because of variations in samples thickness and diameter). The polishing process also removed steel abrasions from the previous uniaxial pressing.

LiAl (commercial, supplier not known), NaPb (homemade, see below) and KPb (homemade, see below) electrodes were deposited on the sample already during the uniaxial pressing. The electrode powder was filled into the pressing tool and loosely compacted by pressing the steel stamp just by hand force. The sample powder was filled on top of the electrode layer and likewise loosely compacted with a clean steel stamp. The powder of the second electrode layer was poured on top of the sample layer and the entire sandwich was subjected to 600 MPa uniaxial pressure. The side of the sample layer tends to get smeared by electrode material upon removing the pellet from the pressing tool and needs to be thoroughly polished with SiC paper.

NaPb was prepared by dissolving 55 at.% sodium (99%) in lead (Roth, 99.99% purity) at 400 °C in an Al_2O_3 crucible on a hot plate in an argon glove box. The product is actually a phase mixture of NaPb and a sodium rich intermetallic phase.^[81] KPb was prepared in the same way, except that only 45 at.%

sodium (99%) was solved in lead to end up with a phase mixture of KPb and K_2Pb_3 .^[82] The metal alloys/mixture of intermetallic compounds have a higher melting point than the pure alkali metals, and fix the chemical potential of the alkali metal at the interfaces to the sample.

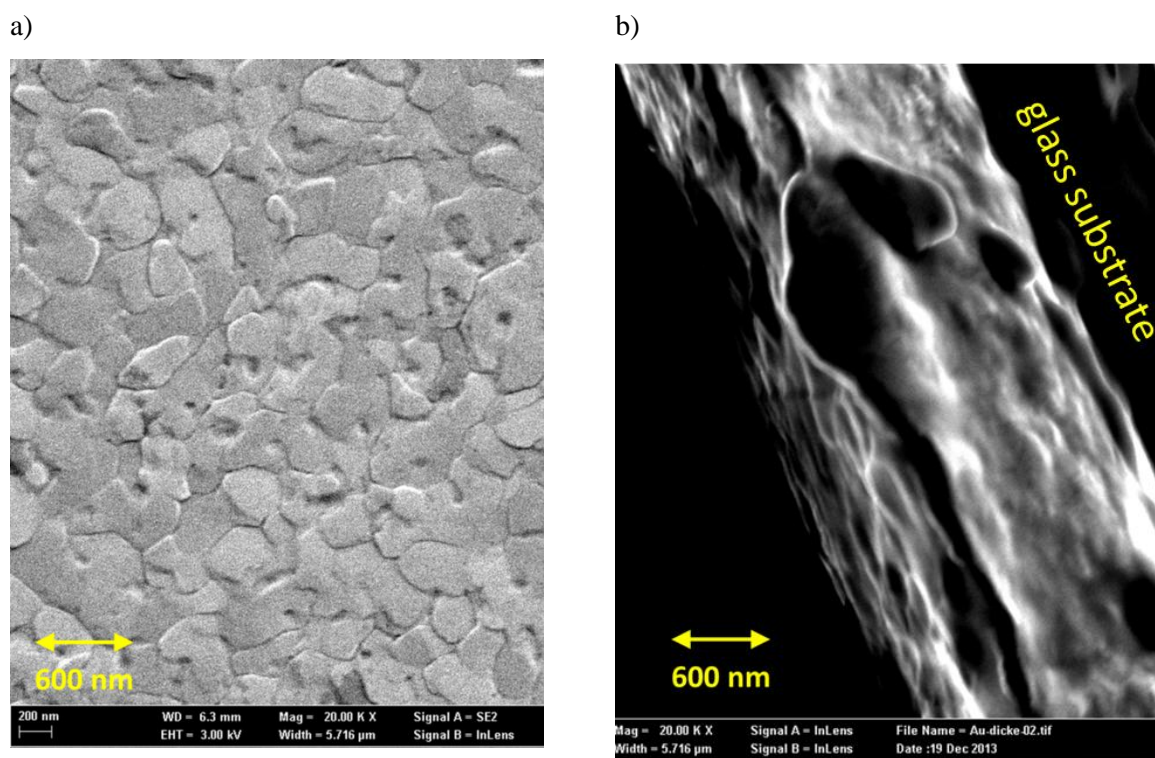


Figure 2.2: Scanning electron microscope image of a dc magnetron sputtered gold film on a glass substrate a) top view and b) side view (fractured surface).

2.2.2 Direct Current Polarization Measurement

The voltage drop across a mixed conductor with reversible electrodes when turning on a constant current corresponds to the dc resistance $\frac{1}{U} = \frac{1}{R_{dc}} = \frac{1}{R_{eon}} + \frac{1}{R_{ion}}$ with the partial electronic and ionic resistances R_{eon} and R_{ion} . For reversible electrodes, the voltage vs. time plot is a simple step function.

The partial resistances can be extracted when selectively reversible and blocking electrodes are used (e.g. Au for electronic charge carriers, YSZ | Pt at high temperatures for O^{2-}). The blocking of one charge carrier gives rise to stoichiometry polarization and a gradient of the chemical potential of the blocked component.^[83] At sufficiently long waiting times a stationary state is reached and the electrical potential gradient compensates by the built up gradient of the chemical potential and a stationary state is reached. The polarization voltage yields the resistance of the non-blocked charge carrier. The transient behavior is related to the chemical diffusion of the blocked component. For small polarization voltages (so that the partial conductivities and diffusivities can be approximated as

constant throughout the sample), the relevant current equations can be reduced to a diffusion equation and analytically approximated for short times $< \tau_\delta/2$ as

$$U(t) = RI + \frac{4 \cdot RI}{\pi^2} \cdot X \cdot \sqrt{\frac{t}{\tau_\delta}} \quad (5)$$

and for long times $> \tau_\delta/2$ as

$$U(t) = RI + RI \cdot X \left(1 - \frac{8}{\pi^2} e^{-\frac{t}{\tau_\delta}} \right) \quad (6)$$

with $X = R_{\text{con}}/R_{\text{ion}}$ for ionic blocking electrodes and $X = R_{\text{ion}}/R_{\text{con}}$ for electronic blocking electrodes.^[84] The relaxation time τ_δ can be extracted either from the short time behavior from the slope of the U vs. \sqrt{t} plot or from the long term behavior from the slope of the $\ln U$ vs. t plot. In the case of two symmetrical blocking electrodes^b, the chemical diffusion coefficient D^δ is obtained from the relaxation time τ_δ and the sample thickness L according to

$$D^\delta = \frac{L^2}{\pi^2 \tau_\delta} \quad (7)$$

Dc measurements were carried out with a Keithley 220 programmable current source connected to the electrodes of the sample and a Keithley electrometer (617 programmable electrometer, 6514 system electrometer) in parallel to the current source. The java based software DC-Pot/Gal (written by Uwe Traub, Max Planck Institute for Solid State Research, Stuttgart) was used to record the data. The program provides a function to automatically turn on and off the current according to a predefined scheme, but as this requires some anticipation of the sample behavior and relaxation times prior the measurement, it was operated manually instead. The currents were adjusted to reach the stationary state between 10 to 100 mV and were typically in the range of 10^{-6} to 10^{-10} A.

2.2.3 Electrochemical Impedance Spectroscopy

Electrochemical impedance spectroscopy enables one to separate transport processes and to characterize their dielectric properties by measuring the current response to a small alternating voltage for a range of frequencies. The resultant impedance spectra are interpreted by comparing the electrochemical behavior of the sample to a model of passive electrical circuit elements.^{[85],[86]}

^bFor one blocking and one reversible electrode, the relaxation process is four times slower, i.e. $D^\delta = \frac{4L^2}{\pi^2 \tau_\delta}$ ^[84]

Charge transport in a dielectric material across the bulk, grain boundaries or electrodes can be modeled as a resistance (corresponding to ohmic transport) in parallel to a capacitor (corresponding to dielectric polarization). Such an RC element describes a semicircle in the plot of the real vs. the imaginary part of the impedance (Nyquist plots) with the relaxation time $\tau = \omega_{\max}^{-1} = RC$. The various serial transport processes can be separated in the impedance spectra if their relaxation times are sufficiently different, and their R and C values can be obtained as fitting parameters. For macroscopic polycrystalline samples, the electrical capacitances of bulk, grain boundary and electrodes differ greatly as entirely different length scales are involved in either case for typical cells. A bulk/grain boundary/electrode capacitance is typically at the order of $10^{-12}/10^{-9}/10^{-6}$ F.

In practice, deviations from ideal semicircles are often observed in the Nyquist plot of real materials, which can be explained by the presence of a distribution of relaxation times e.g. due to inhomogeneities in the sample.^[87] This effect can be taken into account in the model of the electrical circuit elements by using a constant phase element (CPE) with the impedance $Z = \frac{1}{Q \cdot (i\omega)^n}$ instead of a capacitance with the impedance $Z = \frac{1}{i\omega C}$.^[86] From the fitting parameters Q, R and n of the CPE, the capacitance of the relaxation process can be estimated according to^[88]

$$C = (R^{1-n} \cdot Q)^{\frac{1}{n}} \quad (8)$$

The parameter n is typically in the range of 0.8 to 1 and provides a measure for the distortion of the semicircle. For n = 1, the CPE is equivalent to the ideal capacitor.

In this study, an ionic blocking electrochemical cell was used to determine the electronic conductivity by dc polarization measurements and the predominant ionic conductivity was calculated from the bulk conductivity obtained from impedance spectroscopy according to $\sigma_{ion} = \sigma_{bulk,ac} - \sigma_{eon}$ since electronic and ionic resistances can be considered to be in parallel.

The impedance spectra of the sample pellets were recorded with a Novocontrol (Hundsangen, Germany) Alpha-A High Frequency analyzer in the frequency range 10^{-7} to 10^{-2} Hz with 100 mV AC amplitude. The data was analyzed and fitted with the software ZView from Scribner Associates, Inc. (Southern Pines, USA)

2.2.4 Conductivity Relaxation Measurement

In this technique, the time dependent conductivity of a sample is measured after suddenly changing the activity of a component previously equilibrated with the sample, such as the partial pressure of

oxygen. The equilibration can be divided into three processes: a) reactor flushing, b) surface oxygen exchange and c) solid state diffusion into the sample. The flushing of the measurement reactor with the new oxygen partial pressure proceeds comparable fast and can be neglected for the setups (≈ 500 ml volume) and gas flow rates (50 – 100 ml/min) in this study. The relaxation process is therefore diffusion and/or surface reaction rate controlled.

When the surface exchange of oxygen is fast compared to the diffusion in the bulk, the conductivity relaxation is described by a \sqrt{t} law for short times ($t < \tau$) and an exponential decay for long times ($t > \tau$) similar to the dc polarization measurement.^[77] The relaxation time yields again the chemical diffusion coefficient according to equation (7).

In the other extreme case that the equilibration with the new oxygen partial pressure is limited by the surface oxygen exchange reaction, an exponential decay is observed for the all times.^[89] The chemical surface exchange rate constant k^δ is then related to the relaxation time τ and the relevant equilibration length L (i.e., diameter/thickness of a fully dense pellet or grain size in a porous sample) according to equation (9).

$$k^\delta = \frac{L}{2\tau^\delta} \quad (9)$$

2.2.5 Electromotive Force Measurement

A galvanic cell consists of an electrolyte separating two electrodes. Its reversible cell voltage (electromotive force) E gives the free enthalpy $\Delta_r G$ (per mol) of the cell reaction:

$$\Delta_r G = -z \cdot F \cdot E \quad (10)$$

Considering a solid oxygen ion conductor as electrolyte and two electrodes reversible for oxygen exchange exposed to the oxygen partial pressures $p_{O_2}(1)$ and $p_{O_2}(2)$, the overall chemical cell reaction can be simply expressed as



Combining equation (10) and (11) with the exponential relation of the free reaction enthalpy to the mass action constant yields the Nernst equation:

$$E = \frac{RT}{zF} \ln \frac{p_{O_2}(2)}{p_{O_2}(1)} \quad (12)$$

It allows one to calculate the reversible cell voltage as a function of the oxygen partial pressures and number of electrons involved per formula unit for oxides ($z = 4$), peroxides ($z = 2$) and superoxides ($z = 1$). For a mixed conductor with non-negligible electronic conductivity instead of an electrolyte, the measured cell voltage is reduced by the mean ionic transference number $\langle t_{\text{ion}} \rangle$ as approximation for small $p\text{O}_2$ differences.^[77] Hence, the electromotive force (EMF) measurement can be used to separate electronic and ionic conductivity.

The gas tight separation of the gas chambers above the electrodes is usually achieved by a ceramic glue or glass solder^[90]. However, their use was considered not feasible for this study since both sealants require high temperature treatments not tolerable for most of the peroxides and superoxides investigated (either because of decomposition or severe plastic deformation of the samples). Chemical reactions of the sealants with the samples could have posed a further problem.

The amount of leakage still admissible for a nominally gas tight setup depends on the specific context, in particular on the required concentration difference on each side and the flow/pumping rates. The above mentioned experimental difficulty raised the question whether the extremely low leakage, which can be reached by glass sealants, is really necessary for the EMF measurement.

In order to measure the cell voltage and relate it to the transference number, the two electrodes on the sample need to be exposed to sufficiently different and known oxygen partial pressures. For example, one order of magnitude difference in the oxygen partial pressure results in a cell voltage of about 100 and 50 mV for superoxides and peroxides respectively according to equation (12) at 225 °C. It was found that a sufficient sealing to maintain such a $p\text{O}_2$ difference on both sides is already achieved in practice when two flat, rigid solids are pressed onto each other without an additional sealant. The pairing yields a leakage rate typically at the order of $1 \text{ mbar}\cdot\text{l}\cdot\text{s}^{-1}$ (estimated with the pressure loss method), which is readily compensated by flow rates of 50 to 100 ml/min to sustain $p\text{O}_2$ differences of up to two orders of magnitude.

In view of this, an EMF setup without using a sealant agent to separate the gas spaces was designed for this work (Figure 2.3). The measurement was performed on pellets with 12.8 mm diameter. Two 400 nm thick platinum electrodes with different diameter (12.8 and 4 mm for the electrode exposed to $p\text{O}_2(1)$ and $p\text{O}_2(2)$ respectively) were sputtered on the circular faces of the pellet. The pellet is mounted between the platinum foil and the platinum net as shown in the figure. An inner and an outer quartz tube are pressed against the sample by the forces of steel bellows welded to steel tubes. The quartz tubes are connected to the steel tubes by Swagelok ultratorr fittings. The inner quartz tube presses the platinum net on the electrode exposed to $p\text{O}_2(2)$. The outer quartz tube seals the gas room with $p\text{O}_2(2)$ against $p\text{O}_2(1)$ and presses the pellet against the quartz holder to contact the platinum foil with the electrode exposed to $p\text{O}_2(1)$. The sample is most conveniently mounted by pulling a rough vacuum in the gas room (2); the sample pellet is pressed on the quartz tubes by the pressure

differential. The end pressure in (2) should be in the range 1 – 10 mbar with a rotary vane pump and can be taken as a guide to properly align the quartz tubes, sample and quartz holder. The actual $pO_2(1)$ and $pO_2(2)$ of the exhaust gases were measured with homemade potentiometric oxygen sensors based on yttrium stabilized zirconia as electrolyte operating at 700 °C using platinum as electrodes (lambda probes).

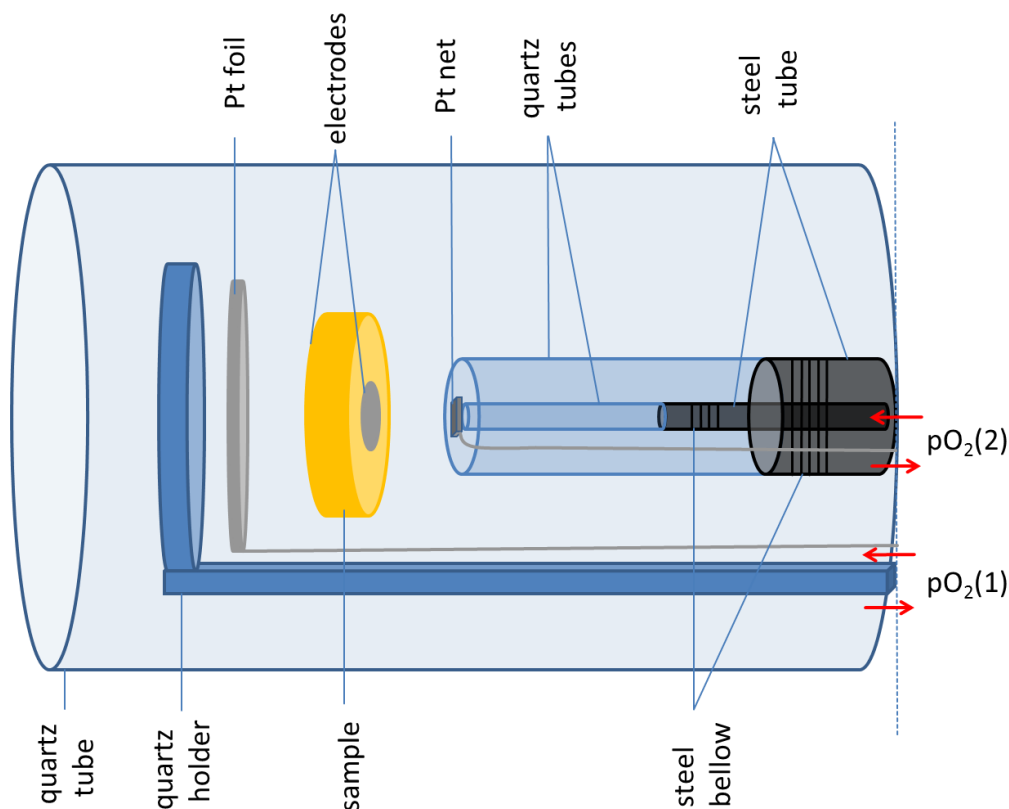


Figure 2.3: Schematic representation of the EMF measurement setup.

2.3 Chemical, Thermal, Thermochemical, Microstructural and Magnetic Characterization Techniques

2.3.1 Scanning Electron Microscopy

Samples for scanning electron microscopy (SEM) were fixed with sticky carbon tape on an aluminum sample holder and coated with about 10 nm of gold by dc magnetron sputtering inside an argon glove box. The samples were transferred to the Zeiss Merlin scanning electron microscope (operated by Annette Fuchs, Max Planck Institute for Solid State Research, Stuttgart) in a desiccator.

2.3.2 Differential Scanning Calometry

Differential Scanning Calometry (DSC) measurements were performed with a Perkin Elmer Pyris 1 (operated by Ewald Schmidt, Max Planck Institute for Solid State Research, Stuttgart). The sample powder was wrapped into gold foil and sealed under argon in an aluminium pan.

2.3.3 Thermogravimetric Measurement

Thermogravimetric measurements were carried out in alumina crucibles with a STA449C Jupiter from Netzsch, Germany with nitrogen as protective gas.

2.3.4 X-ray diffraction

X-ray diffraction (XRD) patterns were measured with a STOE STADI P diffractometer with Cu K_{α1} radiation in transmission geometry (operated by Friedrich Kögel, Max Planck Institute for Solid State Research, Stuttgart). The sample powder was filled in the glove box into mark capillaries (Hilgenberg GmbH, Malsfeld) with the inner diameter 0.3, 0.5, 0.7 or 1 mm (depending on the atomic mass of the cation) and temporarily sealed with high vacuum grease. The capillaries made of quartz or of a low melting glass were permanently sealed outside the glove box with a H₂/O₂ gas burner. Profile matching and Rietveld refinement to determine the lattice constants were performed with the software package Fullprof 2.05.

2.3.5 Inductive Coupled Plasma – Optical Emission Spectroscopy

The cation impurity content in the samples was determined photometrically by inductive coupled plasma - optical emission spectroscopy (ICP-OES) with a Spectro Ciros CCD (SPECTRO Analytical Instruments GmbH, Kleve) at the Max Planck Institute for Intelligent Systems, Stuttgart. The samples were dissolved in diluted hydrogen chloride (outside the glove box) for the analysis.

2.3.6 Raman Spectroscopy

Raman spectra were obtained with a Labram V 010 single grating spectrometer (HORIBA Jobin Yvon GmbH, Bensheim) in quasi-backscattering geometry using the linearly polarized 632.817 nm line of a He/Ne gas laser focused to a 10 μm spot through a 50x microscope objective on to the top surface of the sample. The resolution of the spectrometer (grating 1800 L/mm) is about 1 cm⁻¹. The sample powder was prepared in mark capillaries in the same manner as for XRD.

2.3.7 Infrared Spectroscopy

Fourier transform infrared (FTIR) spectra were recorded with a Bruker IFS 113v spectrometer under nitrogen atmosphere. About 0.5 to 3 mg sample powder was mixed with 300 mg potassium bromide (99+%, for spectroscopy, Fisher Scientific) in an agate mortar in the glove box and pressed with a stainless steel tool with 12.8 inner diameter and 700 MPa of uniaxial pressure to a pellet. The pellets were mounted on the sample holder of the spectrometer already in the glove box and transferred to the

outside in a desiccator. The pellets were exposed to air for about 30 s between the transfer from the desiccator to the spectrometer and until inert gas conditions were achieved.

2.3.8 Electron Paramagnetic Resonance Spectroscopy

EPR spectra were recorded using a Bruker EMX spectrometer operating in the microwave X band region. The powder sample was sealed in suprasil quartz tubes under argon and measured at $T \approx 120$ K (cooling by evaporated liquid nitrogen). Typical parameters of the measurements are listed in Table 2.1.

Table 2.1: Typical parameters of the EPR measurements.

Microwave power / mW	Time constant / ms^{-1}	Modulation frequency / Hz	Modulation amplitude / G	Receiver gain	Number of spectra averaged
63.65	2.56	100	3	$1 \cdot 10^4$	100

The paramagnetic spin concentration was determined from the double integration of the EPR signal and compared to an ultramarine blue standard with $3.72 \cdot 10^{16}$ spins per g.

2.4 Oxygen Isotope Exchange and Gas Phase Analysis

The measurement setup is schematically represented in Figure 2.4. The three way valve behind the flow controllers (3 ml/min) enabled switching between $^{16}\text{O}_2/\text{N}_2$ (commercial, 99.999% chemical purity) and $^{18}\text{O}_2/\text{N}_2$ (home mixed, from $^{18}\text{O}_2$ with 97.1% isotopic purity from Euriso-Top and N_2 of 99.999% chemical purity) gas mixtures. The sample capillary was heated by a temperature controlled tube furnace. A Balzers Prisma quadrupole mass spectrometer detected the oxygen isotopes' evolution (atomic masses 34 and 36 corresponding to $^{16}\text{O}-^{18}\text{O}$ and $^{18}\text{O}-^{18}\text{O}$) via the leak valve after passing the sample capillary. The gas consumption of the MS was about 2 ml/min and it operated at a pressure of 10^{-5} mbar. The excess exhaust gas leaves the measurement line through a paraffin filled gas bubbler. The weighted sample powder was filled in an argon glove box into an 1/8 inch thick quartz capillary with a 10 mm thick bulge and glass frit with 16 to 40 μm pores in the middle to accommodate the powder. The capillary was sealed with 1/8 inch Swagelok ultratorr fittings and could be mounted into the setup without exposure to air (apart from the ≈ 0.1 cm^3 dead volume of the miniature Swagelok quick connection fittings).

The intensities at pre-selected mass/charge ratios m/e (for the species of interest, but also additional m/e serving as baseline) were recorded as a function of the time with a time resolution of 5 s. The obtained spectra of the atomic masses 34 and 36 were manipulated in two steps. Firstly, the intensity

of the atomic mass 25 (where no real signal is expected) was subtracted from them to remove baseline fluctuations. Secondly, the baseline at long times was corrected for a drift term if necessary (usually the baseline was already sufficiently flat after the first step) and set to zero.

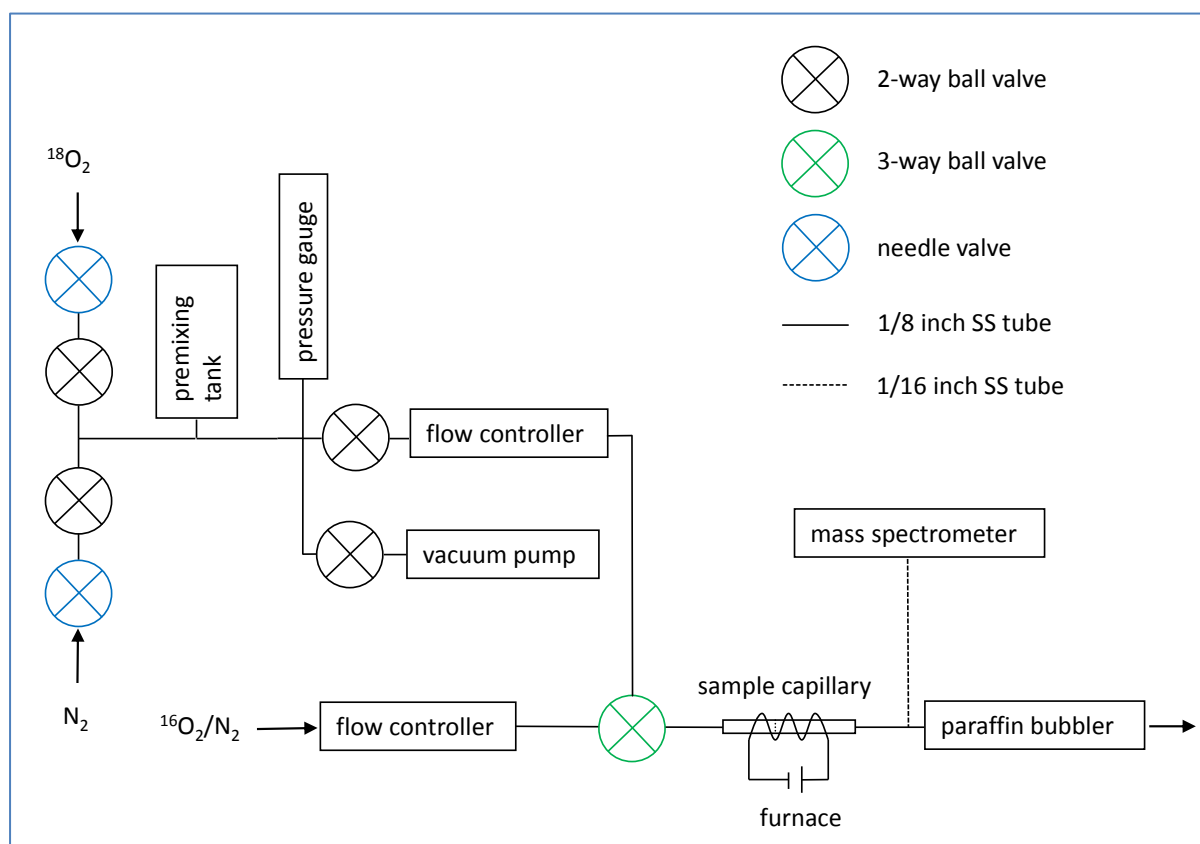


Figure 2.4: Schematic representation of oxygen isotope exchange setup.

3 Results and Discussion

3.1 Lithium Peroxide

3.1.1 Chemical Characterization and Thermal Stability of Li_2O_2

As transport properties are strongly related to the defective species in the sample - point defects, but also interfaces as well as secondary phases - their knowledge is essential for interpreting the electrochemical data. The phase purity of Li_2O_2 samples was routinely determined with x-ray diffraction and Raman spectroscopy. While Li_2O_2 is the most stable alkali peroxide in air, the overall decomposition reaction $\text{Li}_2\text{O}_2 + \text{CO}_2 \rightarrow \text{Li}_2\text{CO}_3 + 1/2\text{O}_2$ proceeds sufficiently fast to yield significant amounts of lithium carbonate impurity phase within 1 h exposure. The use of capillary tubes eliminated this post-preparation contamination of the sample. The preparation of Li_2O_2 in an argon flushed glove bag yields carbonate and hydroxide impurities in the infrared spectrum, but is below the detection limit of x-ray diffraction technique (or amorphous and thus XRD inactive) and is usually also not observed with Raman spectroscopy (Figure 3.1). Factor group analysis predicts two Raman active internal vibrations for Li_2O_2 because of two distinct peroxide sites in the unit cell^[91] (see also Figure 3.2 b), however, only one peak is observed and resolved at 788 cm^{-1} besides the external modes between 100 to 500 cm^{-1} . The amount of secondary phases is thus relatively small and certainly less than the percolation threshold. The concentrations of alkaline earth impurities are typically close or below the detection limit of the method ICP-OES ($c_{\text{Mg}} + c_{\text{Ca}} + c_{\text{Sr}} + c_{\text{Ba}} \leq 20\text{ ppm}$). Other cation impurities were not detected. The concentration of chloride was below the detection limit of the method anion chromatography with conductivity detection ($< 130\text{ ppm}$; the analysis was carried out by Mikroanalytisches Labor Pascher, Remagen-Bandorf, Germany).

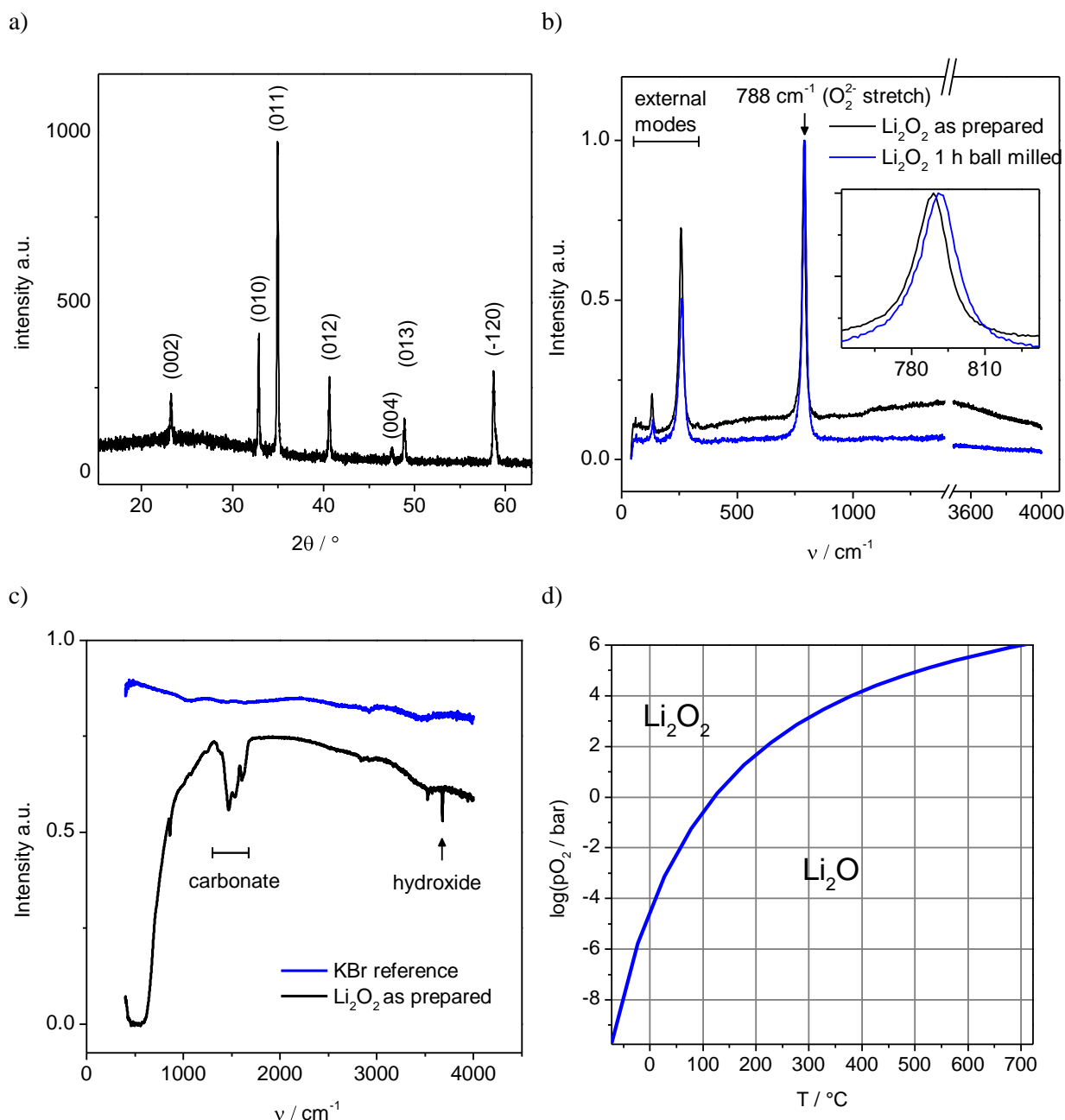


Figure 3.1: a) X-ray diffraction pattern of as prepared Li_2O_2 , b) Raman spectrum of as prepared Li_2O_2 (black) and ball milled Li_2O_2 (blue), c) FTIR spectrum of as prepared Li_2O_2 (black) and KBr reference pellet (blue) and d) thermodynamic stability of Li_2O_2 vs. Li_2O calculated from thermochemical data from ref. ^[92].

In this work, the thermal stability window of Li_2O_2 is decisive for determining the temperature range for the electrochemical investigations. According to thermochemical data published in ref. ^[92], Li_2O_2 is thermodynamically stable versus Li_2O only up to 120°C at $1 \text{ bar } p\text{O}_2$ (Figure 3.1 d). However, the accuracy and reliability of the data has not been established. For example, the free formation enthalpies provided in the reference considerably underestimate the thermodynamic stability of potassium superoxide versus potassium peroxide as well as that of barium peroxide versus barium oxide. The thermal stability of Li_2O_2 has been previously investigated by various methods, namely oxygen evolution analysis, (differential) thermoanalysis, thermogravimetry, XRD and x-ray

photoelectron spectroscopy. A summary of the methods, crucial parameters and results is shown in Table 3.1.

Table 3.1: Summary of the studies on the decomposition temperature of Li_2O_2

Study	Methods	Atmosphere	Heating rate / $^{\circ}\text{C}\cdot\text{h}^{-1}$	Holding time / h	Decomposition onset / $^{\circ}\text{C}$
Rode et al. ^[93]	thermoanalysis, O_2 evolution	air passed over P_2O_5 , Na_2O_2 and KO_2	360	-	280 – 315
Vol'nov ^[94]	thermoanalysis	unclear	ca. 250	-	325
Markowitz et al. ^[15]	chemical titration	286 – 345 bar O_2	-	17 - 62	250 – 350
Tsentsiper et al. ^[95]	O_2 evolution	O_2 , N_2 , 10^{-2} mbar vacuum	-	2	290
Ferapontov et al. ^[96]	DTA, TGA	air	300	-	340 - 348
Yao et al. ^[97]	in situ XRD, XPS, TGA	inert gas (99.999% purity), 10^{-3} mbar vacuum	30	-	250 (surface) 300 (bulk)
This work	ex situ XRD, Raman spectroscopy and TGA	1 bar O_2 (99.999% purity)	-	up to 72	< 225

The studies report an onset of the Li_2O_2 bulk decomposition between 280 to 340 $^{\circ}\text{C}$ and an onset of the surface formation of Li_2O on Li_2O_2 at 250 $^{\circ}\text{C}$. The decomposition reaction is irreversible and not in thermodynamic equilibrium. Li_2O_2 is only kinetically stabilized below these temperatures and the decomposition temperature actually depends on the measurement time and the detection limit of the technique to identify the decomposition product Li_2O . The measurement times used in the above cited studies were mostly small compared to the time that is typically required for the electrochemical measurement of a sample pellet at various temperatures and oxygen partial pressures. Prolonged heat treatments of Li_2O_2 were only performed in the study by Markowitz et al. However, the oxygen partial pressure was more than two orders of magnitude higher than the highest value of 1 bar $p\text{O}_2$ used in this work. The stability range of Li_2O_2 is extended towards higher temperatures at higher $p\text{O}_2$.

It was therefore necessary to check the stability of Li_2O_2 at prolonged heat treatments and 1 bar $p\text{O}_2$. At 250 $^{\circ}\text{C}$ in 1 bar $p\text{O}_2$, Li_2O_2 is entirely decomposed to the oxide within 36 hours according to its Raman spectrum. Already at 250 $^{\circ}\text{C}$ - the reported onset of the Li_2O surface formation - bulk Li_2O_2 is

largely reduced to Li_2O within 36 hours in 1 bar pO_2 according to ex situ XRD (Figure 3.2 a) and Raman spectroscopy (Figure 3.3). It is noteworthy that the lattice constants of Li_2O_2 annealed at 250°C are not altered compared to Li_2O_2 exposed only to lower temperatures. Hence, unlike in barium peroxide^[75] ex situ XRD and Raman spectroscopy provided no evidence for a stable and pronounced unstoichiometry in Li_2O_2 prior to its decomposition to the oxide (this is in contrast to what it is reported for Li_2O_2 by in situ x-ray diffraction in ref. ^[97]). After a heat treatment at 225°C for 72 hours, Li_2O as a possible decomposition product is below the detection limit of XRD and Raman spectroscopy. At 200°C , thermogravimetric measurements of Li_2O_2 uniaxially pressed into pellets in $\text{pO}_2 = 1$ bar evidence a slow, but steady loss of mass that may be related to oxygen release (either by decomposition to the oxide or by reaction with CO_2 to carbonate). At 185°C any possible loss of mass was below the detection limit of the TGA. Thus, the temperature range $185 - 200^\circ\text{C}$ was taken as upper limit for the thermodynamic or kinetic stability of Li_2O_2 as far as the electrochemical characterization was concerned.

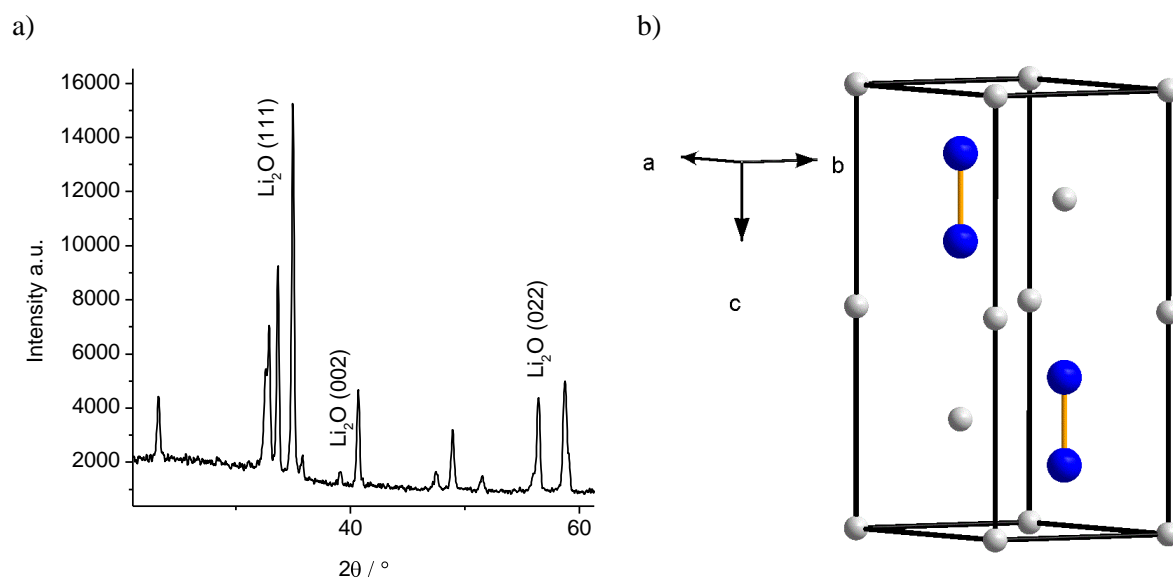


Figure 3.2: a) XRD pattern of Li_2O_2 after 36 hours of heat treatment at 1 bar pO_2 and 250°C (the additional peaks from the decomposition product Li_2O are indicated) and b) hexagonal crystal structure of Li_2O_2 (lithium in gray, oxygen in blue) based on powder XRD data from ref. ^[111].

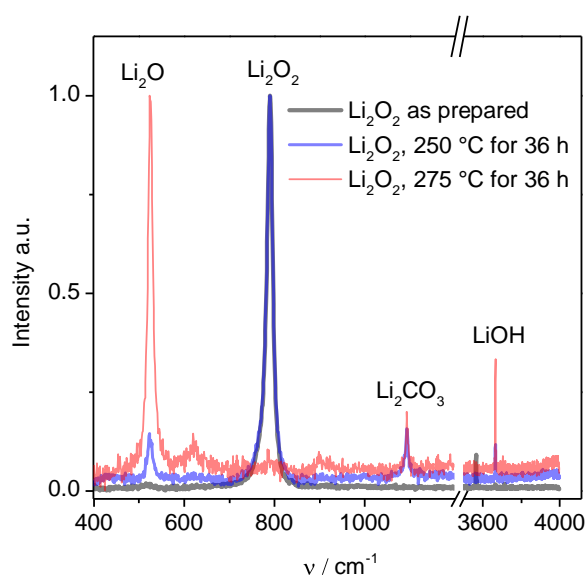


Figure 3.3: Raman spectra of as-prepared as well as of 250 °C and 275 °C annealed Li_2O_2 . The vibrational mode at 523 cm^{-1} is assigned to Li_2O according to ref. [98].

3.1.2 Electrochemical characterization

For electrochemical measurements on pellets, it is desirable to have the possibility of sintering the sample, i.e. removing porosity and increasing the grain size due to Oswald ripening, to improve the electrical contact between the grains and vary the density and porosity of the pellet. Since sintering requires fast diffusion processes of cations and anions, it is typically only relevant for ceramics at temperatures not far from the melting point ($> (2/3) \cdot T_m$).

As pointed out in the previous section, Li_2O_2 is thermodynamically and kinetically unstable above 200 °C (at 1 bar p_{O_2}) and decomposes to the oxide releasing oxygen. The melting point of Li_2O_2 is not known, but the pellets show no sinter activity at 200 °C. According to thermochemical data^[92], an oxygen partial pressure of 1 Mbar is necessary to stabilize Li_2O_2 at 700 °C, which is the estimated temperature at least required for sintering based on the melting point differences between Na_2O_2 (675 °C), Na_2O (920 °C)^[99] and Li_2O (1400 °C)^[100]. Sintered Li_2O pellets would be likely to disintegrate when trying to accommodate excess oxygen to form Li_2O_2 , let aside that the reaction $\text{Li}_2\text{O} + \frac{1}{2} \text{O}_2 \rightleftharpoons \text{Li}_2\text{O}_2$ is kinetically hindered already for a powder at 1 bar oxygen partial pressure. As a consequence, the electrochemical characterization of Li_2O_2 had to be carried out with cold-pressed pellets with 65 - 70% of the theoretical density and corresponding high surface area.

The impedance spectra (Nyquist plots) of Li_2O_2 with symmetrical electrodes of titan, gold, platinum and lithium-aluminum alloy | lithium iodide are shown in Figure 3.4.

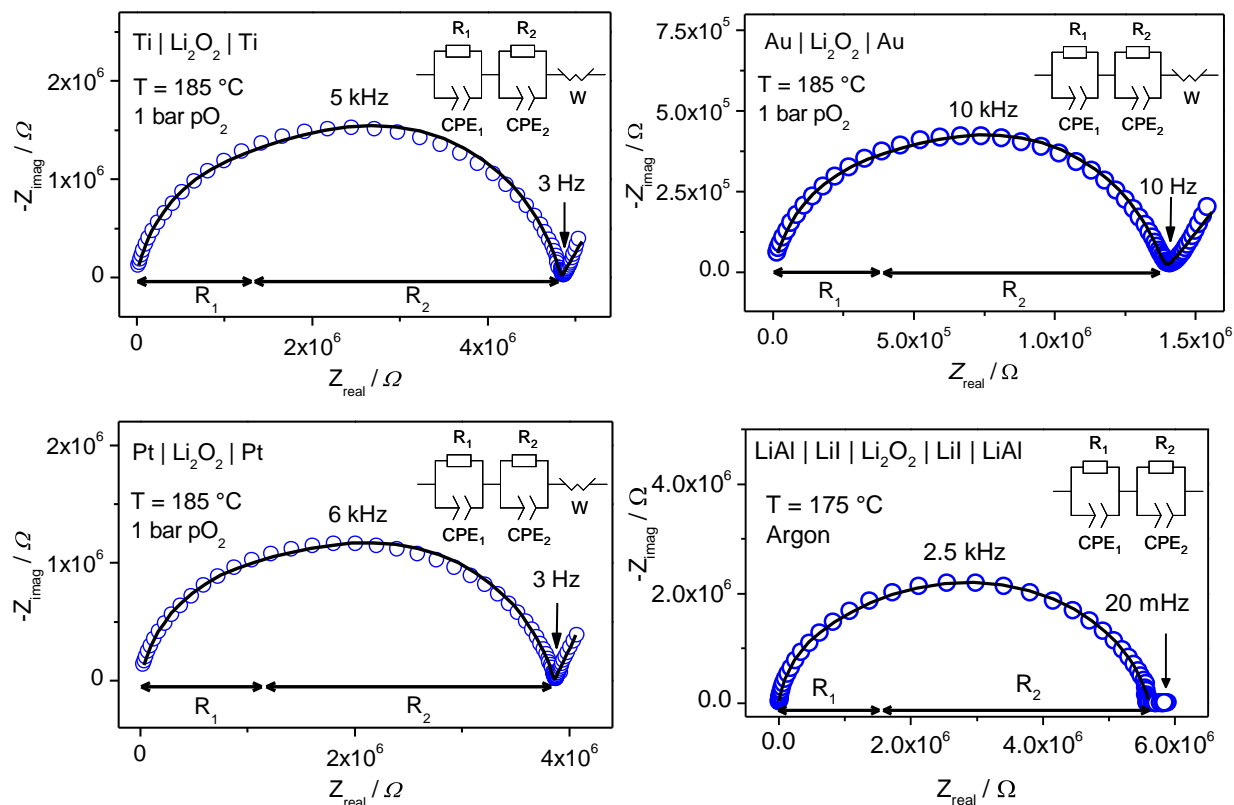


Figure 3.4: Impedance spectra of $\text{Ti} | \text{Li}_2\text{O}_2 | \text{Ti}$, $\text{Au} | \text{Li}_2\text{O}_2 | \text{Au}$, $\text{Pt} | \text{Li}_2\text{O}_2 | \text{Pt}$ at $T = 185\text{ }^\circ\text{C}$ and $p\text{O}_2 = 1\text{ bar}$ and $\text{LiAl} | \text{LiI} | \text{Li}_2\text{O}_2 | \text{LiI} | \text{LiAl}$ at $T = 175\text{ }^\circ\text{C}$ and argon atmosphere ($< 1\text{ ppm } p\text{O}_2$). Each spectrum was measured with a separate sample with slightly varying geometry.

The high frequency region up to 1 - 10 Hz resembles a semi-circle with a capacitance of the order of 10^{-12} F ($\epsilon_r \approx 35$) as is typical for the bulk response of a dielectric ceramic. However, the fit of the spectra in this region with the corresponding model of a resistor and a capacitor in parallel is poor, even if the capacitor is replaced by a constant phase element (CPE) to take into account a depression of the semicircle, e.g. due to sample inhomogeneities (weighted sum of squares ≈ 3). The high frequency spectrum can only be fitted satisfactorily by extending the model by another R-CPE element in series (weighted sum of squares ≈ 0.1). A set of exemplary fitting parameters for the R-CPE elements is given in Table 3.2.

Table 3.2: Fitting parameters R , Q and n of the R-CPE elements in the impedance spectrum of the cell $\text{LiAl} | \text{LiI} | \text{Li}_2\text{O}_2 | \text{LiI} | \text{LiAl}$ at $T = 185\text{ }^\circ\text{C}$ and argon atmosphere in Figure 3.4. Also given is the capacitance calculated from the parameters Q and n of the CPE as defined in chapter 2.2.3.

	R / Ω	$Q / (\text{F}/\Omega)^{1/n}$	n	C / F
$R_1\text{-CPE}_1$	$1.6 \cdot 10^6$	$3 \cdot 10^{-11}$	0.94	$1.6 \cdot 10^{-11}$
$R_2\text{-CPE}_2$	$4 \cdot 10^6$	$6 \cdot 10^{-11}$	0.88	$2 \cdot 10^{-11}$

The relaxation process described by R_2 and CPE_2 can be explained by the sample morphology. During the pressing of the pellets, some plastic deformation may occur as the green density is relatively high compared to a random close packing of spheres $\approx 64\%$ ^[101]. SEM images (Figure 3.5) suggest a relatively good packing of the particles due to their plastic deformation. Still, there is only a limited contact between the individual grains. The current constriction at the particle to particle interfaces gives rise to a frequency dependent distribution of current lines and to the additional relaxation process in the impedance spectrum.^[102] The activation energy is comparable to the bulk process and its capacitance is lower by half an order of magnitude.

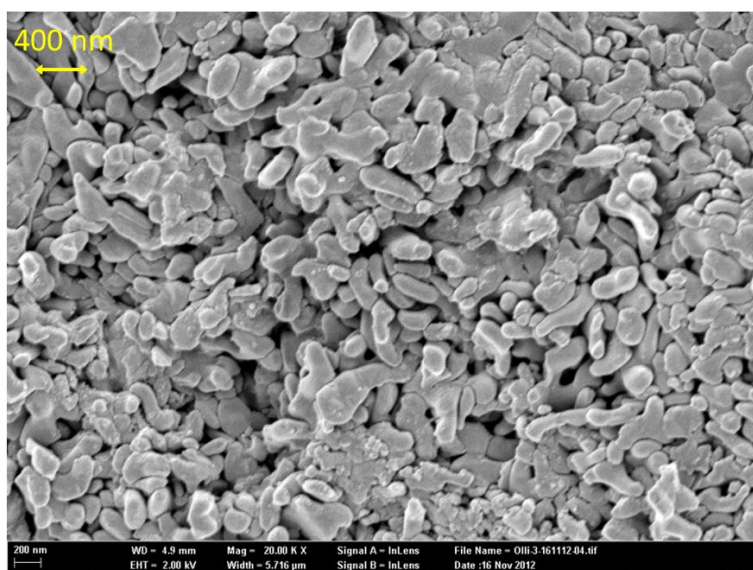


Figure 3.5: Scanning electron microscope image of the fractured surface of an isostatically pressed Li_2O_2 pellet. About 10 nm of Au coating was sputtered on the surface to reduce the electrostatic charging of the sample's surface under the electron beam.

At low frequencies, a Warburg diffusion resistance (W) with a capacitance of the order of 10^{-6} F is observed for the cells with Ti, Au and Pt electrodes due to the blocking of ions at the electrodes. The reversibility of the LiAl electrode demonstrates that Li_2O_2 is mainly a lithium conductor.

As expected for the cell $\text{LiAl} \mid \text{LiI} \mid \text{Li}_2\text{O}_2 \mid \text{LiI} \mid \text{LiAl}$, a stepwise application of a small dc current results in a stepwise voltage increase with a magnitude corresponding to $R_{ac} \cdot I$ (Figure 3.6 a).

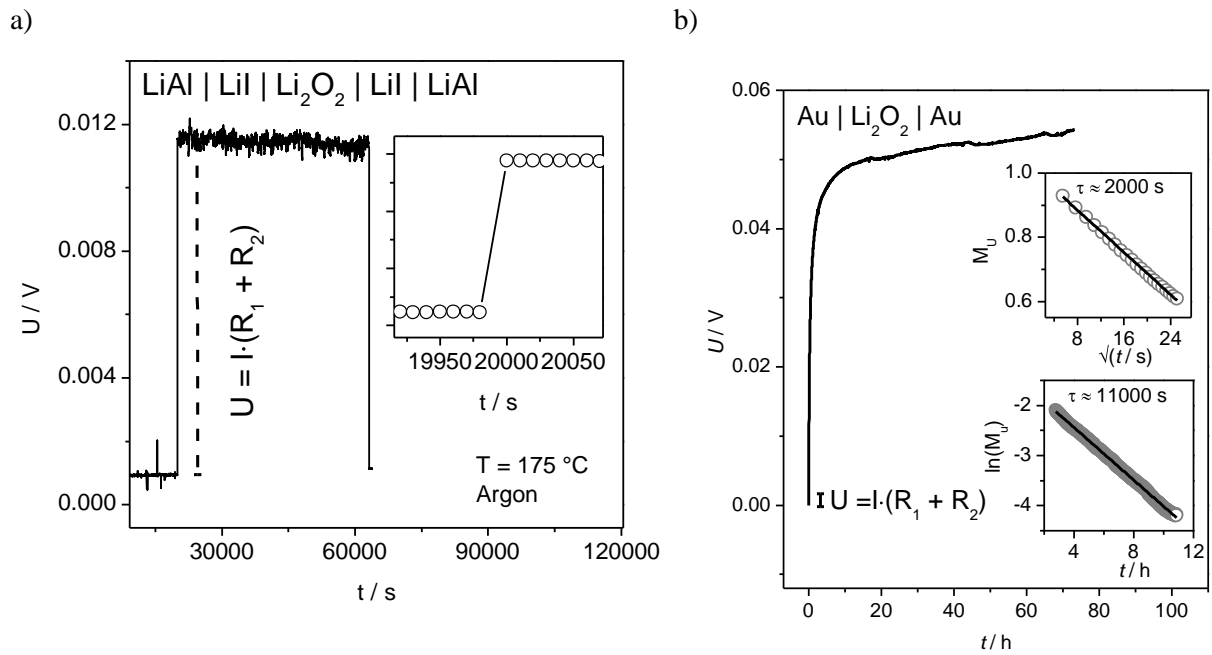


Figure 3.6: Dc polarization measurement of a) $\text{LiAl} | \text{LiI} | \text{Li}_2\text{O}_2 | \text{LiI} | \text{LiAl}$ with $I = 1 \cdot 10^{-9}$ A at 175 °C in argon atmosphere and b) $\text{Au} | \text{Li}_2\text{O}_2 | \text{Au}$ with $I = 1 \cdot 10^{-9}$ A at 185 °C and 1 bar $p\text{O}_2$. The inset in a) shows a close up of the step response (the open circles are the actual data points), the insets in b) fit the short (top) and long (bottom) time transient with the corresponding relations to extract the relaxation time τ . The normalized voltage in the insets is defined in equation (16).

For the symmetric cell $\text{Au} | \text{Li}_2\text{O}_2 | \text{Au}$ extensive stoichiometry polarization owing to the blocking of lithium ions at the electrodes is observed after the initial voltage jump of the magnitude $R_{ac}I$ (Figure 3.6 b). A true stationary polarization voltage not depending upon time is usually not observed; the voltage is continuously drifting to higher values. The time dependence of the voltage drift is linear at least within the measurement times of few days. The exact reason of the drift remains unclear, but it can be presumed to be related to the sluggish equilibration of minority ionic defects in Li_2O_2 from the initial conditions during the synthesis (room temperature, 30% hydrogen peroxide solution) to measurements conditions (185 °C, 1 bar $p\text{O}_2$). The values of R_{con} thus depend upon sample history and measurement time and have to be taken as a lower limit. Despite this, a reliable temperature dependence of the electronic conductivity can still be measured, since the voltage drift proceeds slowly compared to the exponential stoichiometry polarization at long times. R_{con} is obtained from the polarization voltage $U(\infty)$ at long times according to

$$R_{eon} = \frac{U(\infty)}{I} \cdot \left(1 + \frac{R_2}{R_1} \right)^{-1} \quad (13)$$

The second term in equation (13) corrects the apparent electronic resistance for the effect of current constriction using the fitted resistances R_1 (current constriction) and R_2 (bulk contribution) from the impedance measurements. The ionic resistance is given by

$$\frac{1}{R_{\text{ion}}} = \frac{1}{R_2} - \frac{1}{R_{\text{eon}}} \quad (14)$$

The conductivity relates the resistance to the sample geometry:

$$\sigma = \frac{1}{R} \cdot \frac{l}{A^2} \cdot \frac{1}{\frac{3\rho_{\text{theo}}}{2\rho} - \frac{1}{2}} \quad (15)$$

The second term in equation (15) corrects the apparent geometry of the sample (thickness l and area A of the pellet) for the presence of non-conducting porosity assuming spherical pores.^[103] The temperature dependence of σ_{eon} and σ_{ion} is shown in Figure 3.7 a.

The transient behavior of the dc polarization of the cell $\text{Au} | \text{Li}_2\text{O}_2 | \text{Au}$ is shedding light on the kinetics of the chemical lithium transport. The polarization transient obeys a \sqrt{t} law for short times and an exponential decay for long times (after subtracting the linear drift as baseline) as expected for a diffusional process (see 2.2.2). The chemical diffusion of lithium can be calculated from the relaxation time τ obtained from the corresponding fits (insets in Figure 3.6 b) and equation (7). The voltage in the insets is normalized by initial and final voltages U_1 and U_2 according to

$$M_U(t) = \frac{U_1 t - U_2}{U_1 - U_2} \quad (16)$$

The activation energy of this ambipolar diffusion (transport both of electronic and Li ion defects) is about 1 eV (Figure 3.7 a). Although the short and long term approximations are meant to describe the same physical process, the relaxation times obtained from either method differ by a factor of 5. The deviation may be due to influences of interfacial processes for the short term behavior and the long term drift and potential leakage current via the gas phase for the long term behavior.

So far the electrochemical characterizations were carried out at fixed oxygen partial pressure of 1 bar. A change of the $p\text{O}_2$ forces Li_2O_2 to equilibrate with the new chemical potential of oxygen in the gas phase. The oxygen exchange affects not only the concentration of ionic defects, but for reasons of maintaining the charge balance also the concentration of electronic defects must be adjusted. Since electrons are created and holes annihilated by the excorporation of oxygen from the ionic lattice, the electronic conductivity should be enhanced upon decreasing the $p\text{O}_2$ in case of n-type conductivity and reduced in case of p-type conductivity. Thus, the oxygen partial pressure acts as a tool to probe the type of electronic charge carrier and the corresponding defect reactions.

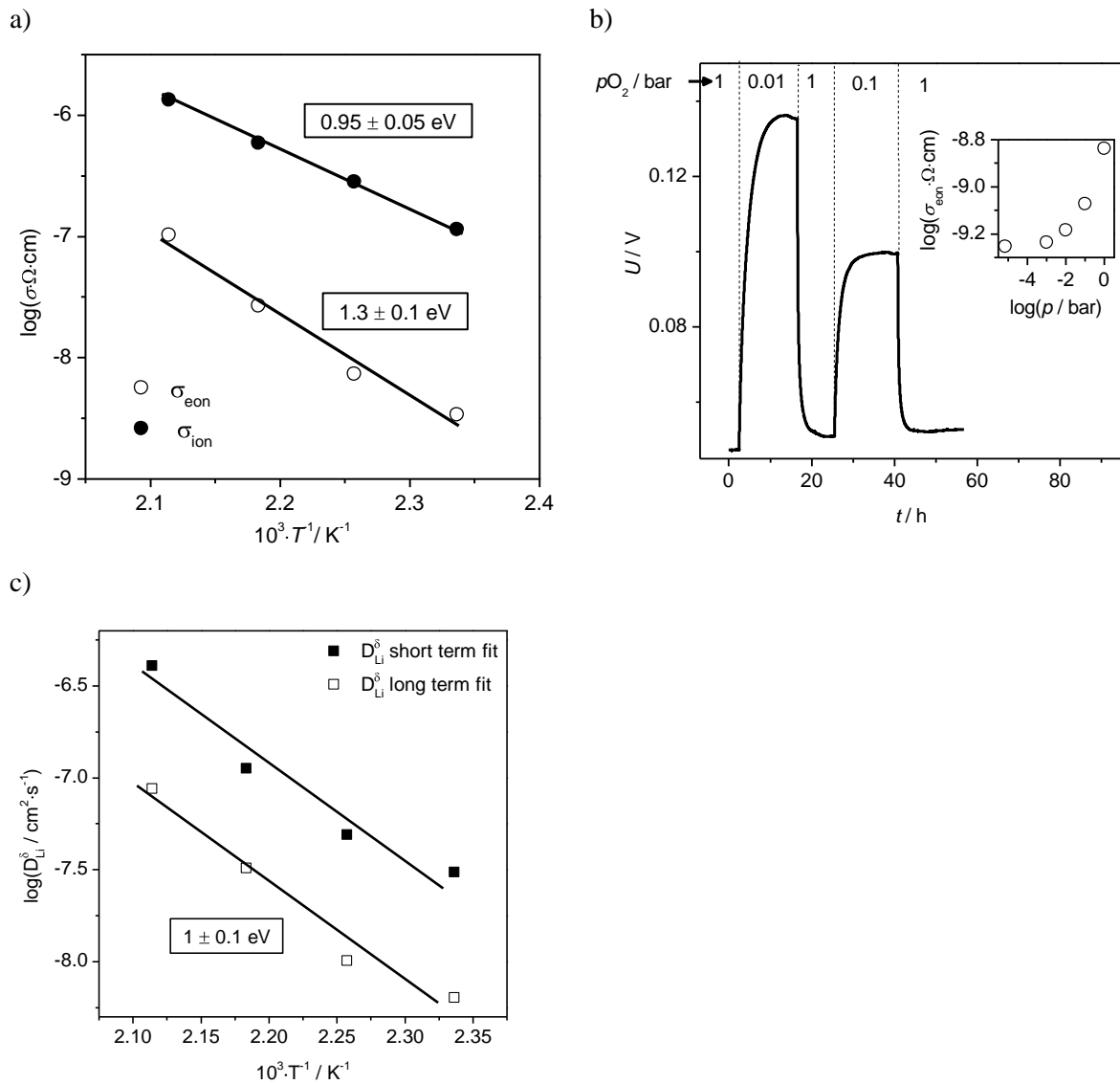


Figure 3.7: a) Temperature dependence of the electronic and ionic conductivity of Li_2O_2 at $1 \text{ bar } p\text{O}_2$, b) voltage relaxation of the cell $\text{Au} | \text{Li}_2\text{O}_2 | \text{Au}$ upon changing the $p\text{O}_2$ of Li_2O_2 at $185 \text{ }^\circ\text{C}$ at a dc bias of $I = 10^{-9} \text{ A}$ (the inset of b) shows the dependence of the electronic conductivity on $p\text{O}_2$) and c) temperature dependence of the chemical diffusivity of Li_2O_2 at $1 \text{ bar } p\text{O}_2$ (the results of both long and short term fit are shown).

One way to determine the $p\text{O}_2$ dependence of σ_{eon} is to set a defined $p\text{O}_2$ in the gas phase, wait for equilibration of the sample with the new $p\text{O}_2$ and then measure the electronic resistance with a dc polarization measurement. The disadvantage of this approach is the time consuming process of stoichiometry polarizing and depolarizing the sample after every $p\text{O}_2$ step as well as the uncertainty of the required equilibration time. As a workaround, an alternative approach was taken. A small dc current was applied to the cell $\text{Au} | \text{Li}_2\text{O}_2 | \text{Au}$ until only the electronic defects contributed to the charge transport. Instead of turning off the current and allowing for depolarization, the $p\text{O}_2$ in the gas phase was changed and the voltage relaxation recorded. At the new steady state, the electronic resistance at the new set oxygen partial pressure can be extracted. It is immediately clear from Figure 3.7 b that σ_{eon} increases with increasing $p\text{O}_2$ and hence the sample is p-type conducting. The quantitative

dependence is, however, less straightforward to interpret as the double logarithmic representation yields a bent curve with increasing slope with increasing pO_2 instead of a straight line as expected from a simple defect model based on the oxygen exchange reaction with lithium vacancies and holes as dominating defects (see next section).

The relaxation curves after changing the pO_2 correspond to an exponential decay for the whole time range. In contrast, a \sqrt{t} law would be expected for short times if the oxygen equilibration were limited by the solid state chemical diffusion (as in the stoichiometry polarization at constant pO_2 above). In this case the relaxation should also proceed within few minutes as the diffusion length (half the grain size) is more than 3 orders of magnitude smaller than in the stoichiometry polarization experiment (pellet length). Therefore, the equilibration process has to be governed either by the surface reaction kinetics or by the reactor flush time and gas phase diffusion into the porous pellet. Assuming an ideal continuously stirred tank reactor, the time for exchanging the gas in the measurement setup with a new mixture can be estimated according to

$$\tau_{\text{flush}} = \frac{V_{\text{reactor}}}{Q_{\text{flow}}} \cdot \frac{293 \text{ K}}{T_{\text{reactor}}} \quad (17)$$

with the gas flow rate Q and the reactor volume and temperature V_{reactor} and T_{reactor} .^[104] For the setup used in the experiment with approximately 500 ml reactor volume and 100 ml/min flow rate, the reactor flush time is about 4 min at 155 °C, which is about two orders of magnitude less than what the limiting process actually takes to relax. SEM images of the pellets show that some grains are fairly well packed with an open space that may be well below 100 nm (below the resolution limit of the technique, see Figure 3.5), while other pores are at the order of 100 nm. To be on the safe side, a conservative estimate of 10 nm channels in the sample is made. At such dimensions, the mean free path of the gas molecules is on the order of the pore size and the diffusion is strongly affected by collisions of the gas molecules with the grains (Knudsen diffusion). With the Knudsen diffusion coefficient $D_{\text{Knudsen}} = \frac{2}{3} \cdot \frac{8RT}{\pi M}^{\frac{1}{3}}$ according to ref. ^[105], the relaxation time into a 1 mm thick sample is less than 2 minutes at 155°C. Hence, neither the chemical diffusion nor the reactor flush time nor the gas phase diffusion can account for the comparable sluggish but highly thermally activated process (> 1 eV activation energy) limiting the oxygen equilibration. Accordingly, the oxygen exchange reaction at the Li_2O_2 -gas interface can be considered to be the rate limiting process.

For the same reasons, possible leakage currents (equivalent to an electronic short circuiting) by oxygen exchange with the gas phase are not relevant for the dc stoichiometry polarization experiment, which may though in principle occurring since the Li_2O_2 sample is porous and the surfaces of the grains are not sealed against the gas phase (if the exchange with the gas phase were exactly zero, the conductivity should not respond to a pO_2 change at all). Such a leakage current would result in a higher apparent electronic conductivity, but more gravely would also lead to a decrease of this

apparent electronic conductivity with decreasing pO_2 (due to the typically strong pO_2 dependence of the surface reaction) and pretend a p-type conductivity, if it is higher than the true electronic current through the bulk. In this case, the relaxation time of the equilibration process would be limited only by the reactor flush time and gas phase diffusion. As mentioned in the previous paragraph, the observed relaxation time of several hours at 155 °C and the high activation energy of > 1 eV are not consistent with these kind of transport processes. Moreover, leakage currents and the corresponding apparent electronic conductivity should strongly depend upon the grain size and sample morphology. When a solution of 30% hydrogen peroxide is added to the lithium methanolate solution dropwise instead of at once, plates of several μm diameter and about 0.5 to 1 μm thickness are obtained (Figure 3.8). Despite the different morphology of the resultant pellets, the measured electronic conductivity is not significantly affected.

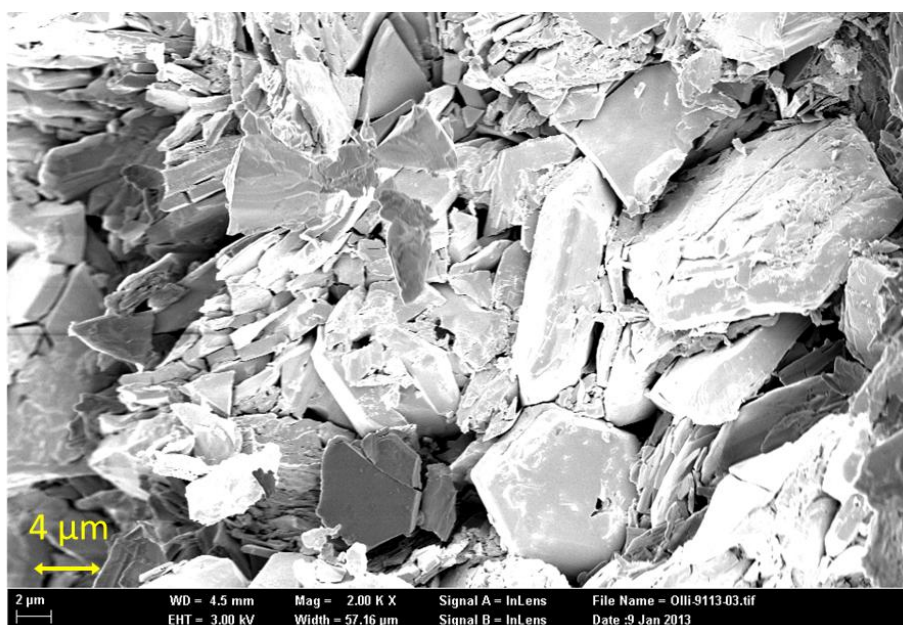


Figure 3.8: Scanning electron microscope image of the fractured surface of an isostatically pressed pellet from Li_2O_2 plates obtained by dropwise addition of 30% H_2O_2 to the lithium methanolate solution. About 10 nm of Au was deposited on the surface as conductive layer.

3.1.3 Defect Chemistry

In order to describe and evaluate the defect chemistry of a binary ionic material, it is necessary to take into account a set of relations completely describing the internal defect reactions, one external defect reaction and the electroneutrality condition. In case of Li_2O_2 , the internal defect equilibria are for example described by the band reaction (formation of electron and holes), Schottky reaction (formation of a Li ion and peroxide ion vacancy; Li_2O_2 is a large band gap material with $E_g = 4$ -5 eV according to theoretical calculations^{[70], [71], [66]}), the Frenkel reaction (formation of a lithium ion

vacancy and lithium ion interstitial), the Anti-Frenkel reaction (formation of a peroxide ion vacancy and peroxide ion interstitial) and the oxide reaction (formation of an oxide defect on a peroxide site). The oxygen excorporation and annihilation of a lithium ion vacancy can be taken as description of the external defect equilibrium. The electroneutrality condition balances the charges of the defects to obtain an electrically neutral crystal. The relevant reactions, mass action laws and the electroneutrality condition are summarized in Table 3.3.

Table 3.3: Basic defect chemical reactions, mass action laws and electroneutrality condition for alkali peroxides.

Band reaction	$0 \rightleftharpoons e' + h^{\bullet}$	$K_B = n \cdot p$
Schottky reaction	$2M_M^x + O_{2O_2}^x \rightleftharpoons K_2O_2 + 2V_M' + V_{O_2}^{\bullet\bullet}$	$K_S = V_M'^2 \cdot V_{O_2}^{\bullet\bullet}$
Frenkel reaction	$M_i^x + V_i^x \rightleftharpoons V_M' + M_i^{\bullet}$	$K_F = V_M' \cdot [M_i^{\bullet}]$
Anti-Frenkel reaction	$O_{2O_2}^x \rightleftharpoons V_{O_2}^{\bullet\bullet} + O_{2i}''$	$K_F = V_{O_2}^{\bullet\bullet} \cdot [O_{2i}'']$
Oxide defect reaction	$O_{2O_2}^x + V_{O_2}^{\bullet\bullet} \rightleftharpoons 2O_{O_2}^x + 2h^{\bullet}$	$K_O = \frac{O_{O_2}^x{}^2 \cdot p^2}{V_{O_2}^{\bullet\bullet}}$
Gas phase reaction	$M_2O_2 + 2V_M' + 2h^{\bullet} \rightleftharpoons 2M_M^x + O_2 \text{ g}$	$K_G = \frac{p_{O_2}}{[V_{Li}]^2 \cdot p^2}$
Electroneutrality condition	$n + V_M' + A' + 2 O_{2i}'' = p + 2 V_{O_2}^{\bullet\bullet} + [M_i^{\bullet}] + D^{\bullet}$	

The p_{O_2} dependences of the various defects can be expressed by combing the external defect reaction with the relevant internal defect equilibria. Since the combination of the gas phase reaction with the oxide defect reaction and the Schottky reaction results in an equilibrium without any charged species relative to the perfect lattice (as the oxide is carrying the same charge as the peroxide), the dependence of the oxide defect on the p_{O_2} can be immediately given as $[O_{O_2}^x] \sim p_{O_2}^{\frac{1}{2}}$.

The mass action law of the gas phase reaction in Table 3.3 relates the concentrations of lithium vacancies and holes to the oxygen partial pressure. It can also be combined with the Schottky reaction to calculate the p_{O_2} dependence of the concentrations of peroxide vacancies as well as with the Frenkel and Anti-Frenkel reaction to obtain the dependence of lithium and peroxide ion interstitials

upon pO_2 (first column in Table 3.4). It is not possible anymore to solve these expressions analytically without approximation. The sum on each side of the electroneutrality condition in Table 3.3 needs to be reduced to a single term by assuming the other contributions being negligible. The approach is known as Brouwer approximation^[106] and is effectively dividing the pO_2 (or metal activity) range into regimes, in which a simplified electroneutrality condition and the derived dependence of defect concentrations hold (Table 3.4). The graphical representation (logarithm of the defect concentrations versus the logarithm of the oxygen partial pressure/metal activity) is known as Kröger-Vink or Brouwer diagram (Figure 3.9).

Table 3.4: Oxygen partial pressure dependence of basic defects in alkali peroxides.

Approx. Neutrality Condition	$V'_M = [M_i^\bullet]$ or $V'_M = 2[V_{O_2}^{\bullet\bullet}]$ or $V'_M = [D^\bullet]$ or $A' = [M_i^\bullet]$ or $A' = 2[V_{O_2}^{\bullet\bullet}]$	$V'_M = p$ or $n = [M_i^\bullet]$	$n = p$	$n = 2[V_{O_2}^{\bullet\bullet}]$
$V_{O_2}^{\bullet\bullet}$	0	-1/2	-1	-1/3
V'_M	0	1/4	1/2	1/6
M_i^\bullet	0	-1/4	-1/2	-1/6
p	1/2	1/4	0	1/3
n	-1/2	-1/4	0	-1/3
$[O_{O_2}^x]$	-1/2 for all cases			

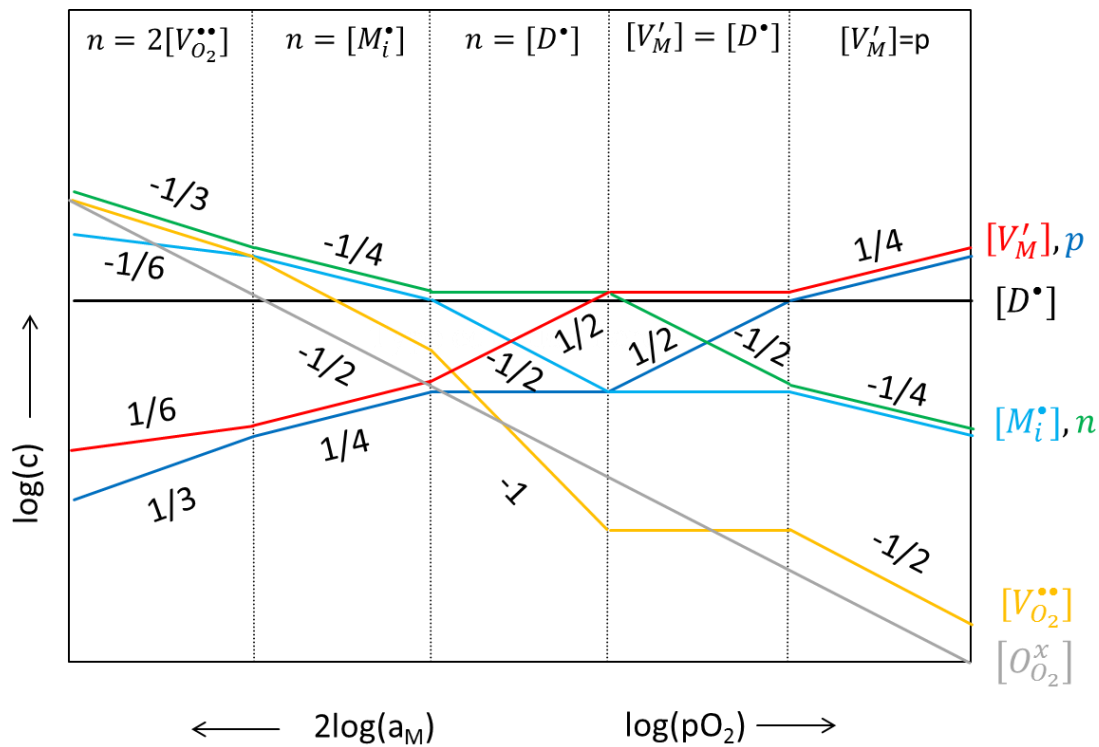


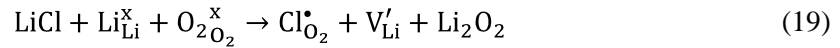
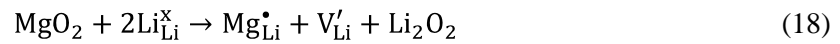
Figure 3.9: Dependence of the defect concentrations on pO_2 and metal activity (Kröger-Vink diagram) for donor doped alkali metal peroxides.

In practice, not all of these defects are relevant and not all dependencies can be accessed experimentally. In particular the stability range of the peroxide must be considered, which probably does not comprise the strongly reducing conditions (i.e. $n = [D^*]$, $n = [Li_i^*]$, $n = 2[V_{O_2}^{..}]$). It is also expected that excess electrons are energetically unfavourable because they will neither be much stabilized at the alkali cations nor at the peroxide ions.

From the comparison of the low frequency ac impedance spectra and dc polarization measurements between the cells $Au | Li_2O_2 | Au$ and $LiAl | LiI | Li_2O_2 | LiI | LiAl$ it is clear that lithium ionic defects are the dominating species for the electrical transport in lithium peroxide. The possible lithium ionic defects are vacancies (compensated by peroxide vacancies, lithium interstitials or donor impurities) and interstitials (compensated by lithium vacancies or acceptor impurities). The prevailing defects depend upon the impurity content of the sample and conversely, intentionally changing the concentration of impurities (doping) results in a variation of the respective lithium defect concentrations. For example, donor dopants introduce excess positive charges (relative to the perfect lattice) that can be compensated by the creation of lithium vacancies or excess electrons.

According to the charges and the ionic radii, suitable donor dopants for Li_2O_2 are Mg^{2+} on a lithium site (the crystal radii in sixfold coordination are 90 pm for Li^+ and 86 pm for Mg^{2+})^[107] and halides such as Cl^- on a peroxide site (167 pm for Cl^- ^[107], 62 pm in the ab plane and 194 pm in

crystallographic c-direction for O_2^{2-} ^[11]). The incorporation reactions of Mg^{2+} and Cl^- dopants can be described as follows:



Suppose that the nominally undoped Li_2O_2 were predominantly a lithium interstitial conductor, the above insertion of donor species coupled with the Frenkel reaction $Li_{Li}^x \rightleftharpoons V_{Li}' + Li_i^\bullet$ would result in depletion of lithium interstitials and a decrease in the conductivity. Conversely, if a vacancy transport mechanism were prevailing, a conductivity enhancement would be expected upon donor doping. These relations are specific cases of the more general rule of homogenous doping according to which $\frac{z_k \delta c_k}{z \delta C} < 0$ with the charge z_k and concentration c_k of the defect k and the charge z and concentration C of the dopant.^[77] A change in the transport mechanism from lithium interstitials to lithium vacancies due to excessive donor doping should lead to a change in the activation energy, as interstitials and vacancies can be supposed to have differing formation and migration barriers.

As described in the experimental part, the dopants were added as magnesium methanolate and lithium chloride respectively to the lithium methanolate solution prior the precipitation reaction with 30% hydrogen peroxide. The amount of chloride and magnesium detected in the Li_2O_2 sample powders by element analysis (ICP-OES for magnesium, anion chromatography with conductivity detection for chloride) is typically an order of magnitude lower than the amount actually added to the solution, i.e. not all dopant is incorporated in Li_2O_2 . X-ray diffraction and Raman spectroscopy of the doped samples do not show any change in the lattice constant and change of the O-O bond strength respectively. In order to compare the conductivity of the doped samples vs. nominally undoped Li_2O_2 it was first necessary to establish the value the latter, as its conductivity substantially scatters from batch to batch. The ac bulk conductivity (\approx ionic bulk conductivity) of 8 samples of nominally undoped Li_2O_2 from different preparation batches was evaluated. The mean conductivity and its standard deviation as a function of the temperature are presented in Figure 3.10.

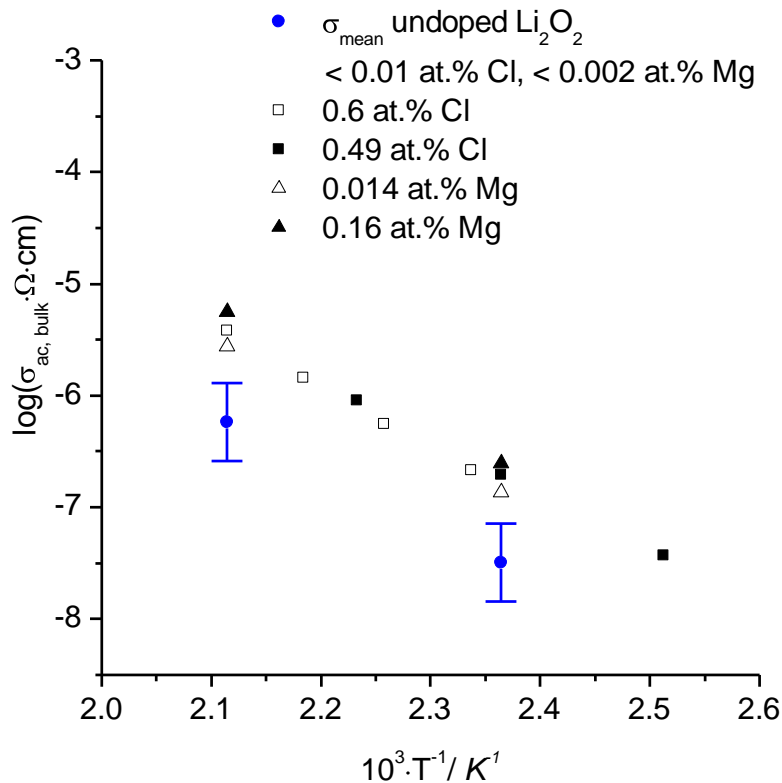


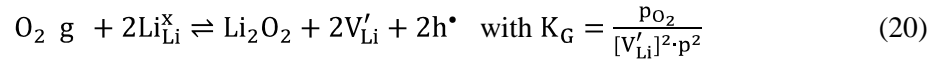
Figure 3.10: Temperature dependence of the mean ac bulk conductivity (i.e. without the contribution of current constriction) of 8 different samples of nominally undoped Li_2O_2 (blue filled circles) with the standard deviation as error bars and doped samples with different actual Cl and Mg content (open and solid black squares and circles).

The plot also includes the ac bulk conductivity of four donor doped samples. Their conductivity is significantly higher than the undoped samples according to the above statistical analysis. That the increase in case of the chloride doped samples is caused by the presence of a possible LiCl impurity phase at a volume fraction below the x-ray diffraction limit can be ruled out, as LiCl itself has a lower conductivity and also lower activation energy than both the nominally undoped and chloride doped Li_2O_2 samples.^[108] The increase of the conductivity is in accordance with a transport via V'_{Li} . A transition from interstitial to vacancy transport mechanism is discarded as the activation energy remains the same upon donor doping. The correlation between ac bulk conductivity and donor content is semi-quantitative, i.e. the higher the donor content, the higher the conductivity, but the conductivity does not scale linearly with the donor concentration. Such behavior could be the result of the formation of a secondary phase containing some of donor dopants leading to lower effective dopant concentration in Li_2O_2 than suggested by the elemental analysis, or of more complex defect chemistry in the system.

The constant activation energy for nominally undoped and donor doped samples could hypothetically also be explained by a negligible formation energy for lithium vacancies compared to its migration energy. However, density functional theory calculations predicted bulk formation energies in the

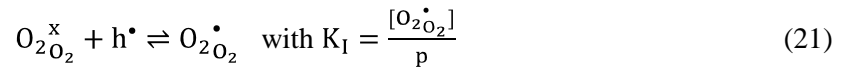
range of 2.85 to 4.1 eV for V'_{Li} [70],[66]. The more likely explanation is thus that already the nominally undoped Li_2O_2 is not in the intrinsic regime at the measurement conditions (with the lithium vacancy concentration determined by the Schottky reaction $0 \rightleftharpoons 2V'_{\text{Li}} + V_{\text{O}_2}^{\bullet\bullet}$), but in the extrinsic regime with V'_{Li} fixed by donor impurities, such as alkaline earth metal ions but also protons bound to peroxides yielding HO_2^{\bullet} . The observed $p\text{O}_2$ independence of σ_{ion} supports this finding. The activation energy of ≈ 1 eV of σ_{ion} would accordingly correspond to the migration barrier of V'_{Li} transport.

Since lithium ion vacancies and holes are the main ionic and electronic charge carriers in Li_2O_2 , the oxygen exchange reaction is most conveniently written as in Table 3.3 as



With the electroneutrality condition for the extrinsic regime $V'_{\text{Li}} = D^{\bullet}$, the oxygen exchange reaction predicts the electronic conductivity being proportional to the square root of the oxygen partial pressure $\sigma_{\text{eon}} \sim p\text{O}_2^{\frac{1}{2}}$. The experimentally measured slope in the $\log\sigma_{\text{eon}}$ vs. $\log p$ plot is significantly less than +1/2 (Figure 3.7b). It is about +0.25 for the two highest $p\text{O}_2$ values of 0.1 to 1 bar and even less for lower $p\text{O}_2$. The measured slope of +0.25 fits to the intrinsic defect regime with the electroneutrality condition $V'_{\text{Li}} = p$, but the agreement can be considered incidentally since the $p\text{O}_2$ independent ionic conductivity and invariant activation energy upon donor doping provide strong arguments that the defect chemistry of the Li_2O_2 as prepared in this study is in the extrinsic regime.

The electronic structure of Li_2O_2 is mainly determined by the peroxide molecule ion^[109] and the electron holes can be considered to be accommodated in the valence band consisting mainly of peroxide orbitals. In defect chemical terms, it ionizes the peroxide to superoxide according to



With its unpaired electron, the superoxide defect should give rise to a signal in electron paramagnetic spectroscopy. The EPR spectrum of as prepared Li_2O_2 measured at 120 K is shown in Figure 3.11b (blue curve). Besides the broad peak at $g = 2.1$ originating from the quartz capillary, a sharp peak of low intensity is found at approximately $g = 2.006$. Based on the comparison with EPR studies of superoxide adsorbed on metal oxides^[110] and alkali superoxides isolated in a noble gas matrix^[111] the signal can be assigned to superoxide defects. The paramagnetic spin concentration in the as prepared Li_2O_2 determined from the double integration of the EPR signal and comparison to an ultramarine blue standard amounts to < 0.1 ppm.

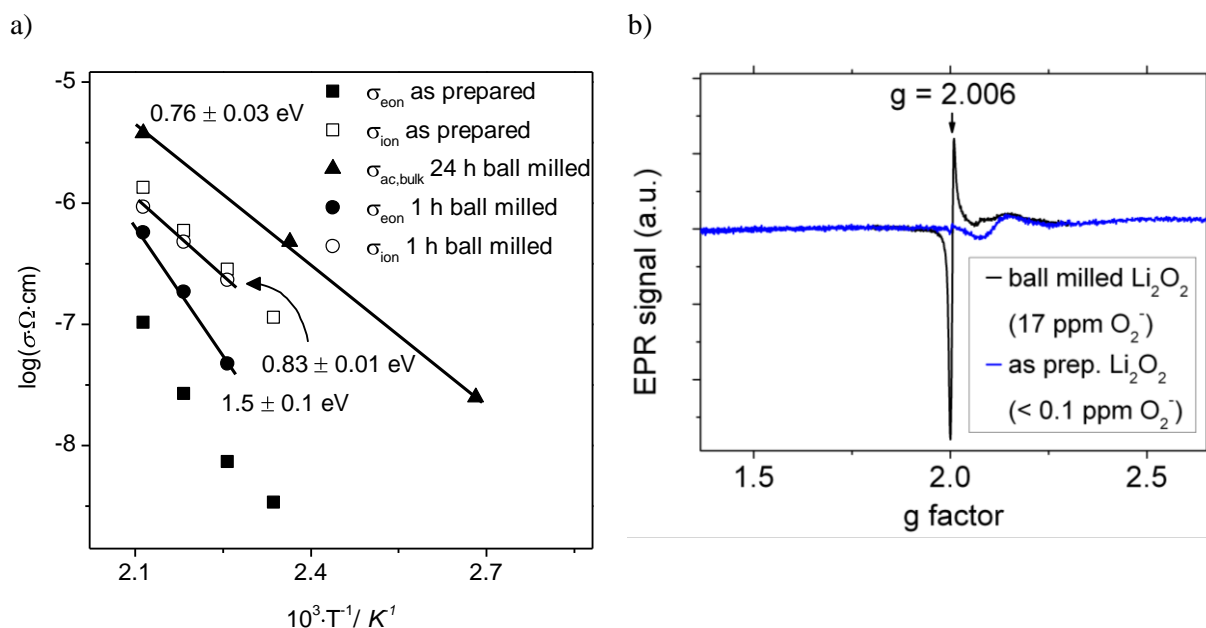


Figure 3.11: a) Electronic and conductivity of Li_2O_2 ball milled for 1 hour at 200 rpm (open and solid circles) and ac bulk conductivity of Li_2O_2 ball milled for 24 h at 400 rpm (solid triangle) in 1 bar pO_2 and b) electron paramagnetic resonance spectra of as prepared and Li_2O_2 ball milled for 1 hour at 200 rpm measured at 120 K.

In planetary ball milling, high kinetic energy is transferred from the milling media to the sample powder resulting in the disintegration of the particles. The decrease in the grain size and increase in the surface area typically achieved by ball milling affect the transport properties when interfacial and surface processes play a role. Besides downsizing the particle size, ball milling has also been shown to influence the transport properties of materials by inducing defects.^[112]

The grain size of as prepared Li_2O_2 is already relatively small with 100 – 200 nm and it not significantly decreased by ball milling. The ionic conductivity of Li_2O_2 ball milled for 1 hour in argon atmosphere at 200 rpm is comparable to the value of as prepared Li_2O_2 (Figure 3.11a), but the activation energy is decreased from 0.95 to about 0.83 eV. The effect is further enhanced by prolonged ball milling for 24. If the contribution of the defect formation to the activation energy is equal to zero as indicated by donor doping experiments, then the change of the activation energy after ball milling can be attributed to a lowering of the lithium ion migration barrier due to distortion of the lattice. In contrast, the electronic conductivity is significantly increased by about a factor of 5 in the 1 hour ball milled sample and the ionic transference number drops from about 0.92 to 0.6 at 200 °C. The activation energy of the electronic conductivity is surprisingly higher pointing towards some decrease of the hole mobility in the ball-milled sample. Most interestingly, the concentration of superoxides in Li_2O_2 is greatly enhanced from less than 0.1 ppm to about 17 ppm by ball milling (black curve in Figure 3.11b).

If the superoxide (= holes trapped on peroxide ions) defects are the electronic charge carriers in Li_2O_2 as suggested above, the increase of the superoxide defect concentration by ball milling should give rise to the same order of magnitude increase in the electronic conductivity, whereas only a fraction of

this is observed in practice. To explain the difference, it should be noted that a 24 h heat treatment at 200 °C - corresponding to the time necessary for a dc measurement to obtain σ_{con} - already decreased the spin concentration by a factor of 10. The superoxide defects created during ball milling are at least partly healed out at elevated temperatures. Moreover, the higher activation energy of the electronic conductivity in the ball milled sample (1.5 eV vs. 1.3 eV in as prepared Li_2O_2) could indicate a lower mobility of holes compensating the increased charge carrier concentration.

The condition of electroneutrality in ionic solids requires that the oxidation of peroxide to superoxide species according to equation (22) is accompanied by defect reactions compensating for the loss of negative charge at the peroxide.



A possible reaction could be the trapping of one or two electron at peroxide vacancies in analogy to color centers (trapping of electrons at oxide vacancies) in alkaline earth oxides^[113]:



Another possible mechanism could be that electrons generated by the superoxide formation reduce peroxide ions to oxide defects:



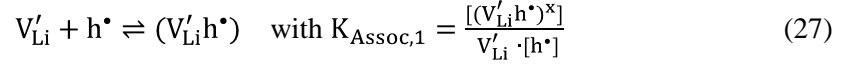
Finally, in ref. ^[71] the trapping of electrons in broken O-O bonds is suggested as possible electronic defect in Li_2O_2 :



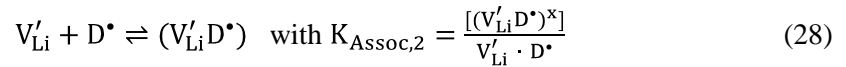
The formation of triple charged oxygen species O_2^{3-} is rather questionable though. The electron in the antibinding π^* orbital of O_2^{3-} formed in reaction (26) as well as the single charged vacancy in reaction (23) should give rise to a signal in the EPR spectrum, but none is observed other than from the superoxide and the quartz capillary. This leaves reactions (24) and (25) as possible mechanism to accommodate the electron stripped from the peroxide during the ball milling treatment. However, in the absence of evidence favoring one or the other, the question which of the reactions is prevailing in ball milled Li_2O_2 cannot be answered here.

The defect chemical description of Li_2O_2 is incomplete when interactions between defects are not taken into account. According to DFT calculations, the V_{Li}' migration barrier for transport in the (100) plane is estimated as 0.35 eV.^[66] In a polycrystalline sample as investigated in this study the lithium

transport may proceed on other crystallographic planes as well (for which migration barriers have not been calculated), but the large difference still indicates that the interaction of lithium vacancies with positively charged defects (holes, donors) contributes to the experimental migration barrier. The interaction energy between holes and lithium vacancies was calculated as 0.47 eV.^[70] The corresponding trapping reaction reads:



A comparable value can be assumed for the activation energy of the trapping reaction for donor dopants and lithium vacancies:



This energy term adds up to the migration barrier of the free carrier when a trapped lithium vacancy is changing its site. In the covered temperature range it can also be assumed that most of the electron holes are trapped by the larger number of lithium vacancies and the theoretically calculated trapping energy of 0.47 eV between holes and lithium vacancies also adds to the migration barrier of the free electronic charge carrier. Experimentally, the activation energy of about 1.3 eV for σ_{con} is found.

The chemical diffusion coefficient is composed of the individual defect diffusivities according to

$$D^{\delta} = t_{\text{ion}}D_{\text{eon}}\chi_{\text{eon}} + t_{\text{eon}}D_{\text{ion}}\chi_{\text{ion}} \quad (29)$$

with the respective transference number t and the trapping factors χ .^[114] Assuming that the trapping factors are of the same order of magnitude (since the trapping energies are probably comparable), with $t_{\text{ion}} \gg t_{\text{eon}}$ and a typically higher mobility of holes compared to lithium vacancies, the chemical diffusivity would be determined by the term $t_{\text{ion}}D_{\text{eon}}\chi_{\text{eon}}$, i.e. by the electronic transport. The contribution of the migration of undissociated pairs of $(V'_{Li}h^{\bullet})$ to the chemical diffusion might result in the activation energy of the chemical diffusion coefficient being somewhat lower than the activation energy of the electronic conductivity.

The trapping reactions of holes by lithium vacancies (equation (27)) and of lithium vacancies by donors (equation (28)) can be combined with the oxygen exchange reaction (equation (21)) to calculate from the respective mass action laws how the concentrations of the associates and the unassociated donors depend upon the oxygen partial pressure under the assumption of strong trapping, i.e. large mass action constants for the trapping reactions, for both the intrinsic and extrinsic regime with the electroneutrality conditions $V'_{Li} = [h^{\bullet}]$ and $V'_{Li} = D^{\bullet}$ (Table 3.5).

Table 3.5: Dependency of concentrations of associates and free donors upon p_{O_2} assuming strong trapping in Li_2O_2 . The first row gives the condition of electroneutrality.

	Intrinsic regime with $V'_{Li} = p$	Extrinsic regime with $V'_{Li} = [D^*]_{total}$
$[(V'_{Li}h^*)^x]$	$= \frac{K_{Assoc,1}}{K_G} \cdot p_{O_2}^{\frac{1}{2}}$	$= \frac{K_{Assoc,1}}{K_G} \cdot p_{O_2}^{\frac{1}{2}}$
$[(V'_{Li}D^*)^x]$	$\approx [D^*]_{total}$	$\approx [D^*]_{total}$
$[D^*]$	$= \frac{{}^4 K_G}{K_{assoc,2}} \cdot [(V'_{Li}D^*)^x] \cdot p_{O_2}^{-\frac{1}{4}}$	$= \frac{[(V'_{Li}D^*)^x]}{K_{assoc,2}}$

Moreover, the dependence of the defect concentrations on the total donor concentration can be derived from the set of mass action laws in equations (20), (27) and (28) with the approximations of strong trapping ($[(V'_{Li}D^*)^x] \approx [D^*]_{tot}$) or weak trapping ($D^* \approx [D^*]_{tot}$) as shown in Table 3.6. For the studied Li_2O_2 samples, the high lithium vacancy migration barrier suggests strong trapping of lithium vacancies to donors, but at very low donor concentrations the configurational entropy will dominate resulting in a weak association of the defects despite a high binding enthalpy.

Table 3.6: Dependency of defect concentrations upon total donor concentration in the extrinsic regime for the cases of weak and strong interactions.

Defect	Weak trapping	Strong trapping
$[D^*]$	$\approx [D^*]_{tot}$	$\approx \frac{[D^*]_{tot}^{\frac{1}{2}}}{K_{assoc,2}}$
$[V'_{Li}]$	$\approx [D^*]_{tot}$	$\approx \frac{[D^*]_{tot}^{\frac{1}{2}}}{K_{assoc,2}}$
$[(V'_{Li}D^*)^x]$	$\approx K_{assoc,2} \cdot [D^*]_{tot}^2$	$\approx [D^*]_{tot}$
$[h^*]$	$\approx \frac{1}{K_G} \cdot p_{O_2}^{\frac{1}{2}} \cdot [D^*]_{tot}^{-1}$	$\approx \frac{K_{assoc,2}}{K_G} \cdot p_{O_2}^{\frac{1}{2}} \cdot D^*_{tot}^{-\frac{1}{2}}$
$[(V'_{Li}h^*)^x]$	$= \frac{K_{assoc,1}}{K_G} \cdot p_{O_2}^{\frac{1}{2}}$	$= \frac{K_{assoc,1}}{K_G} \cdot p_{O_2}^{\frac{1}{2}}$

A graphical illustration of these relations is shown in Figure 3.12. The logarithm of the defect concentrations is plotted as function of the logarithm of the control parameters p_{O_2} (and with $p_{O_2} \sim a_{Li}^{-2}$ also the lithium activity a_{Li}) and the total donor content. The exponent in the dependencies

can be immediately taken from the slope of the curves, but since the values of the mass action constants are not known for now, neither are the absolute values of the concentrations.

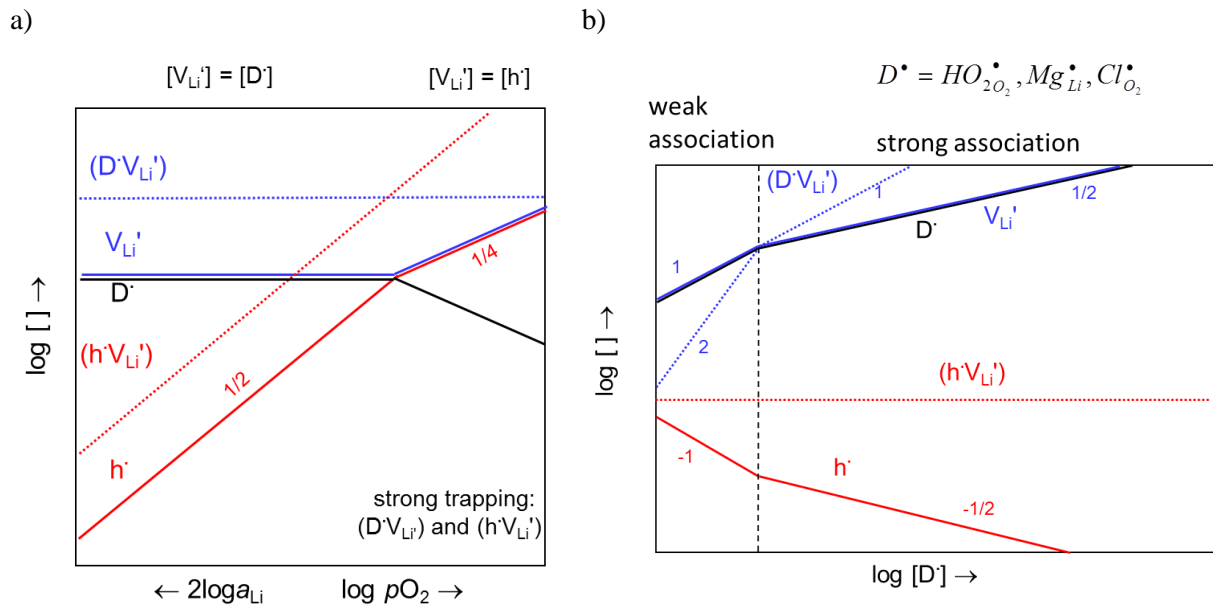


Figure 3.12: Dependence of the defect concentrations a) on pO_2 and a_{Li} and b) on donor content. The slopes of the dependences in the log-log-plot are shown by the numbers.

3.1.4 Chemical oxygen exchange kinetics in Li_2O_2

As the equilibration of the porous Li_2O_2 pellet with a new pO_2 (Figure 3.7b) is limited by the surface exchange, the effective surface exchange rate constant $k^\delta = \frac{l_{\text{grain}}}{\tau}$ can be calculated according to equation (9) with the relaxation time τ and half the grain size l_{grain} (Figure 3.13). Here it is assumed that the grain size is the relevant equilibration length. The assumption could actually underestimate k^δ , because the fact that some plastic deformation occurs upon pressing the Li_2O_2 pellet might result in a larger effective equilibration length. The figure also shows k^δ of the electrochemically and kinetically well studied Fe-doped strontium titanate for comparison. The data indicates a much higher surface reaction rate in Li_2O_2 compared to Fe-doped $SrTiO_3$. The superior kinetics can be understood if it is considered that in $SrTiO_3$, or any other oxide based material, the covalent bond of oxygen molecules needs to be broken in addition to the transfer of two electrons in order to form oxide species. In contrast, in Li_2O_2 , or any other peroxide based material, the oxygen incorporation can possibly proceed without the need to overcome the activation barrier of breaking of the oxygen bond.

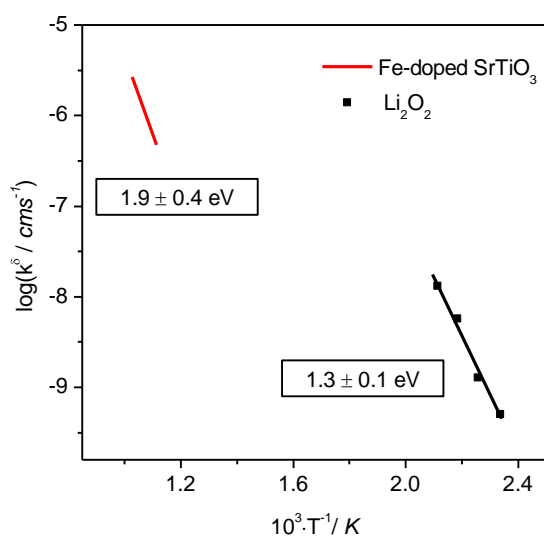
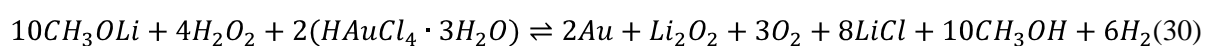


Figure 3.13: Temperature dependence of the chemical reaction rate constant k^δ of Li_2O_2 (from this study, determined by dc conductivity measurements) and Fe-doped SrTiO_3 (from ref. ^[115] determined by optical absorption spectroscopy on single crystals).

3.1.5 Li_2O_2 -Au composite

The poor electronic conductivity (cf. Figure 3.7) is one of the major practical issues with regards to the Li-oxygen battery.^[52] It may be addressed by acceptor doping, which is expected to generate additional electron holes as charge compensation. However, acceptor doping turns out to be more challenging compared to donor doping. A suitable anion dopant requires a negative charge of > 2 , but a potential dopant like nitride is too basic to exist in the water/methanolate solution without becoming protonated. For the cation site, only a rather unrealistic dopant of zero charge would do the job of homogenous acceptor doping. Local p-type doping of lithium peroxide was predicted by the interaction with carbon sheets.^[116] This led to the idea of heterogeneously doping Li_2O_2 powder with noble metal nanoparticles to locally withdraw electrons from the peroxide ions. The preparation is experimentally feasible, since gold nanoparticles can be precipitated by reduction with hydrogen peroxide from a precursor at a wide pH range.^[117] As hydrogen peroxide is already employed in the Li_2O_2 precipitation, the composite can be conveniently prepared in one go by adding the gold precursor $\text{HAuCl}_4 \cdot 3\text{H}_2\text{O}$ (Alfar Aesar) to the Li methanolate solution prior the addition of 30% H_2O_2 . Hydrogen peroxide acts both as reduction and precipitation agent in this case:



The resultant powder is grey (see also Figure 2.1) and shows the XRD patterns of Li_2O_2 and Au nanoparticles (Figure 3.14). The diameter d of the primary gold particles can be estimated from the

full width half maximum (FWHM, in radians) of the reflection at the angle θ (in radians) with the x-ray wavelength λ according to the Scherrer formula^[118]:

$$d = \frac{0.9\lambda}{FWHM \cdot \cos\theta} \quad (31)$$

According to this, the size of the Au nanoparticles is about 10 – 15 nm. The amount of Au added to Li_2O_2 is about 0.5 at.% and is confirmed by chemical analysis with ICP-OES. The effect of the gold particles on the Li_2O_2 is most strikingly seen with EPR spectroscopy (black curve in Figure 3.15). The composite contains a much higher concentration of superoxide species (≈ 1000 ppm) compared to the nominally undoped Li_2O_2 (< 0.1 ppm), even exceeding that of mechanically ball milled powder (≈ 17 ppm). It should be emphasized that the sharp EPR signal is characteristic of isolated, superoxide defects in a diamagnetic matrix rather than bulk material. In principle, the enhanced number of superoxide defects should give rise to a higher electronic conductivity. However, the defects are healed out at elevated temperatures (blue curve in Figure 3.15), which are necessary for the electrochemical characterization limited by the input resistance of the measurement equipment.

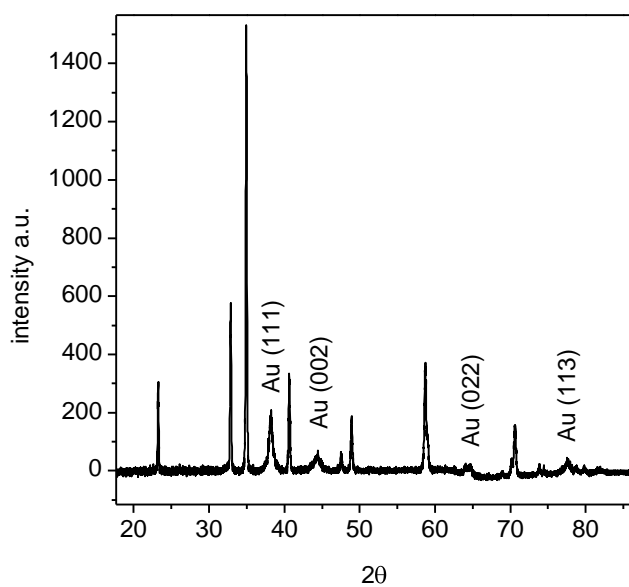


Figure 3.14: X-ray diffraction pattern of $\text{Li}_2\text{O}_2/\text{Au}$ composite powder (Au reflections are indicated, all others are from Li_2O_2).

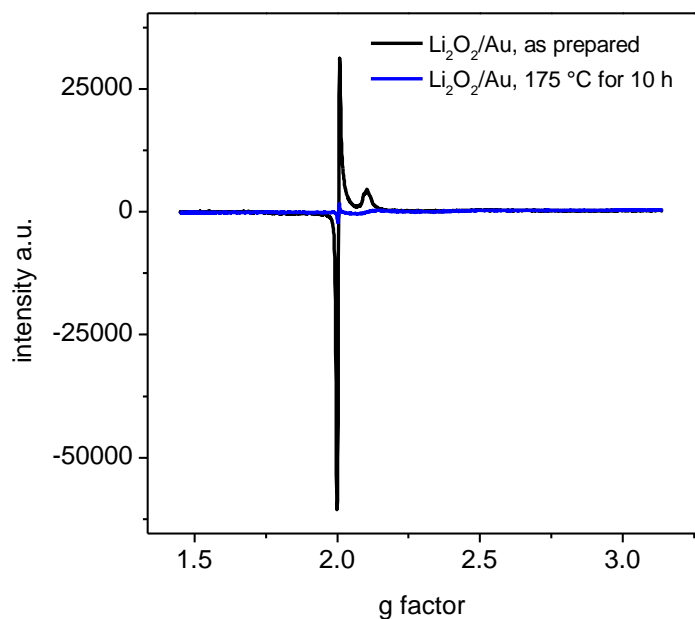


Figure 3.15: EPR spectra of $\text{Li}_2\text{O}_2/\text{Au}$ composite powder as prepared (black) and after 10 h heat treatment at $175\text{ }^\circ\text{C}$ (blue) at 120 K.

3.2 Sodium Peroxide

3.2.1 Chemical characterization and Crystallographic Structure

Na_2O_2 prepared from sodium metal of 99.95% metal purity contains some cation impurities according to ICP-OES analysis. The most prevailing impurity is potassium with a content of 40 to 90 ppm, followed by calcium with a concentration of 10 to 20 ppm.

The XRD pattern of Na_2O_2 shows a minor impurity (reflection at $2\theta = 38^\circ$ in Figure 3.16a, possibly carbonate or hydroxide), while the Raman spectrum is phase pure with the external modes in the frequency range 100 to 300 cm^{-1} and the two stretch vibrations of O_2^{2-} occupying two different sites in the lattice at 738 and 793 cm^{-1} (grey curve in Figure 3.16b).

The Na_2O_2 crystal lattice is hexagonal at low to intermediate temperatures (Figure 3.17). A phase transition takes place at $507\text{ }^\circ\text{C}$ according to in situ Raman measurements^[119], but its crystal structure is unknown.

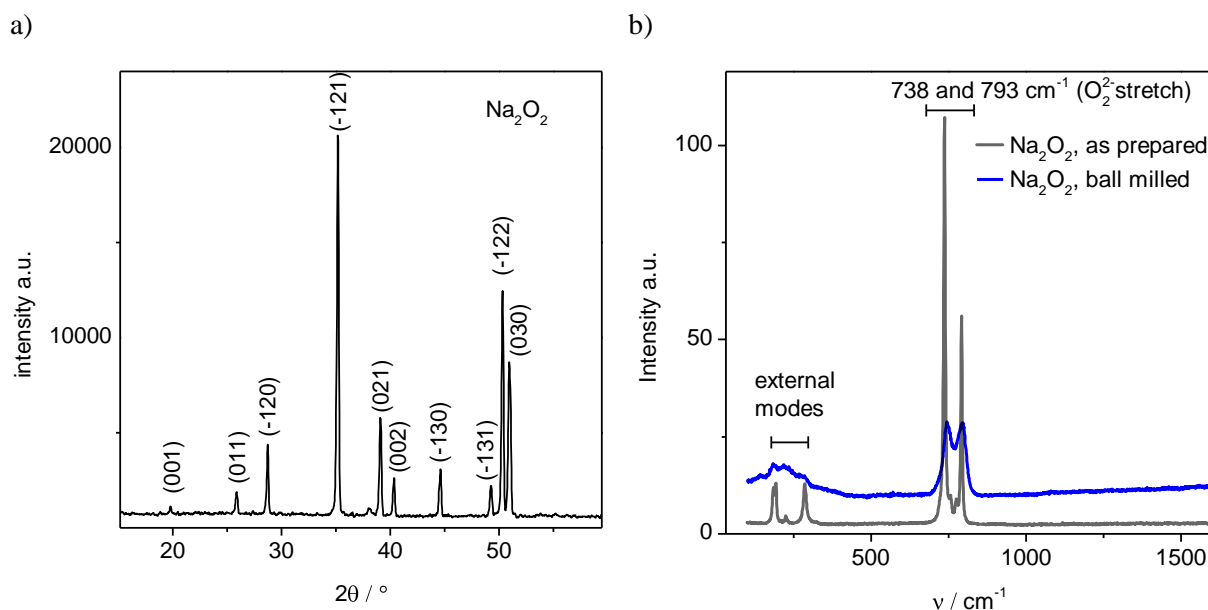


Figure 3.16: a) XRD pattern of as prepared Na_2O_2 and b) Raman spectra of as prepared Na_2O_2 and ball milled Na_2O_2 .

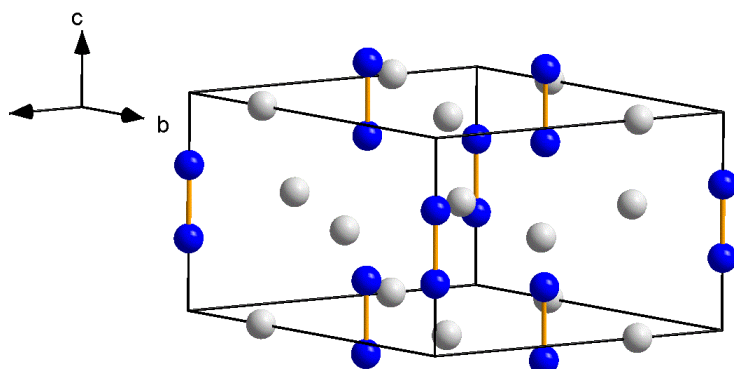


Figure 3.17: Unit cell of hexagonal Na_2O_2 (sodium in gray, oxygen in blue) based on single crystal XRD data from ref.^[11]

3.2.2 Electrochemical characterization

The impedance spectrum of the cell $\text{Au} | \text{Na}_2\text{O}_2$ (sintered) $| \text{Au}$ (ionic blocking electrodes) can be fitted with the equivalent circuit consisting of R-CPE and a Warburg element W (top left in Figure 3.18). The contribution at high frequencies is related to the bulk response of Na_2O_2 (dielectric constant $\epsilon = 24$). The sintered Na_2O_2 pellets have an improved grain to grain contact compared to cold pressed Li_2O_2 pellets, the high frequency range of the impedance spectra can be significantly better fitted with only one R-CPE element (weighted sum of squares $\approx 0.1 - 0.3$; the fit parameters of the R-

CPE element for the cell $\text{Au} | \text{Na}_2\text{O}_2 (\text{sintered}) | \text{Au}$ are $R = 1.7 \cdot 10^{-6} \Omega$, $Q = 4 \cdot 10^{-12} (\text{F}/\Omega)^{1/0.95}$ and $n = 0.95$). The low frequency contribution described by the Warburg diffusion element is related to the blocking of ionic charge carriers at the Au electrode (alternatively, a R-CPE element with a capacitance $C \approx 10^{-6} \text{ F}$ typically for electrode polarization can be used to fit the low frequency contribution). The same electrode response is obtained for Pt electrodes instead of Au. Ti electrodes exhibit the same electrode response for fresh samples, but are subjected to aging phenomena at 200°C leading to an increasing electrode resistance over the time (likely titanium oxide formation).

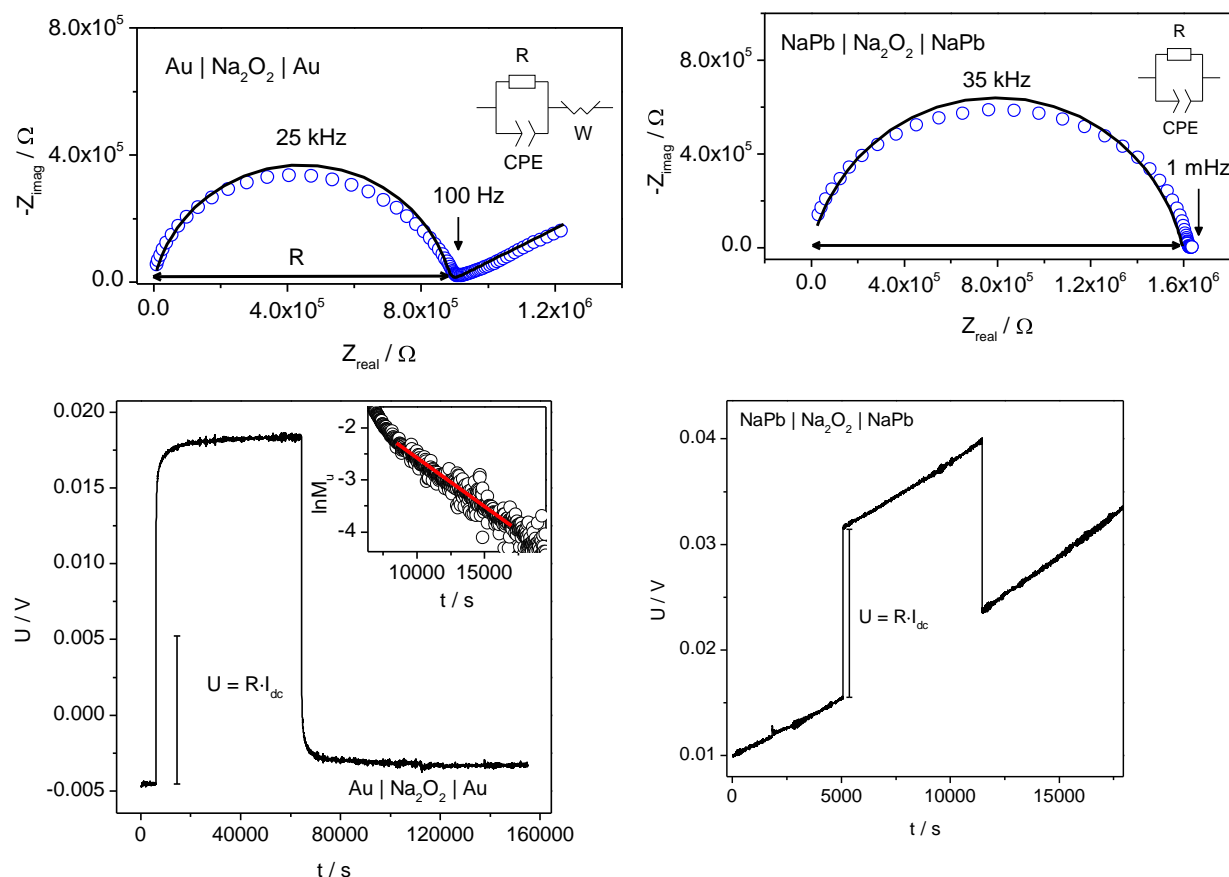


Figure 3.18: Impedance spectra (top) and dc polarization measurements (bottom) of the electrochemical cells $\text{Au} | \text{Na}_2\text{O}_2 | \text{Au}$ (left) and $\text{NaPb} | \text{Na}_2\text{O}_2 | \text{NaPb}$ (right) with $I = 10 \cdot 10^{-9} \text{ A}$ at 1 bar pO_2 and 200°C . M_u in the inset is the normalized voltage.

In contrast, for the cell $\text{NaPb} | \text{Na}_2\text{O}_2 | \text{NaPb}$ (reversible for sodium ions and electronic charge carriers; pure sodium metal melts already just below 100°C) the electrodes are not polarized at low frequencies (top right in Figure 3.18). The distinct electrode resistance with Au, Pt and Ti electrodes and reversible nature of the sodium electrodes suggests that Na_2O_2 is a mixed conductor with sodium defects as main ionic charge carrier.

As in the case of lithium peroxide, the contributions of electronic and ionic conductivity can be most accurately (i.e. without fitting the electrode polarization in the impedance spectrum) separated by dc stoichiometry polarization of $\text{Au} | \text{Na}_2\text{O}_2 | \text{Au}$ with small polarization currents/voltages (bottom left in

Figure 3.18). In the stationary state of the dc measurement, the electrical current is carried only by the electronic charge carriers yielding the electronic conductivity σ_{eon} . With the overall bulk conductivity obtained from the intercept of the high frequency semi-circle with the abscissa in the impedance spectrum, the ionic conductivity is given by $\sigma_{\text{ion}} = \sigma_{\text{ac}} - \sigma_{\text{eon}}$. The sum of formation and migration energy for sodium and electronic defects respectively is about 1.3 and 1.15 eV (Figure 3.19a)

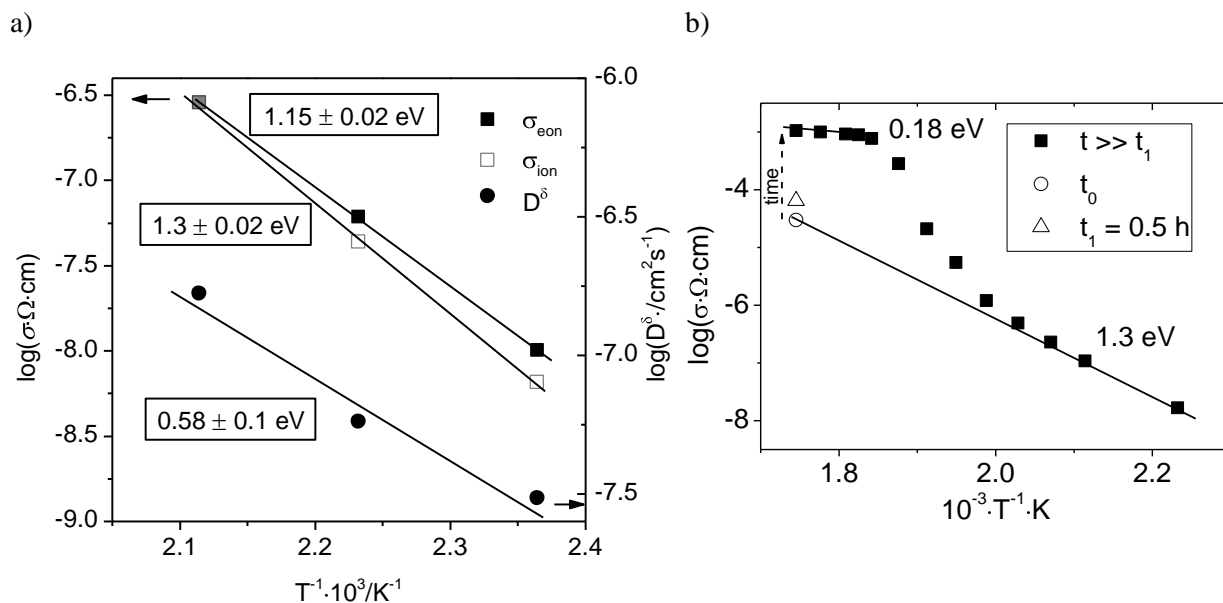


Figure 3.19: Temperature dependence of a) electronic and ionic conductivity as well as of the chemical diffusivity of previously 475 °C sintered Na_2O_2 at 1 bar pO_2 and b) ac conductivity of a freshly prepared (empty circle) and aged (empty triangle and solid squares) uniaxial pressed Na_2O_2 pellet in argon (right).

The transient of the stoichiometry polarization in the case of the cell $\text{Au} | \text{Na}_2\text{O}_2 | \text{Au}$ is determined by the chemical diffusion of sodium in the sample. For long times ($t > \tau$) the polarization and depolarization can be described with an exponential decay with the relaxation time τ (inset in Figure 3.18 bottom left). From the temperature dependence of the chemical diffusivity of sodium calculated from equation (3) the activation energy of about 0.58 ± 0.1 eV is obtained (the value has to be taken with caution as it is based on only three, scattering data points).

As expected from the impedance spectrum, the cell $\text{NaPb} | \text{Na}_2\text{O}_2 | \text{NaPb}$ shows no stoichiometry polarization but a step function when a small dc bias is applied (Figure 3.18 bottom right) owing to the reversible nature of the sodium alloy for the main charge carriers in Na_2O_2 (there is, however, a steady drift of the baseline, which may be due to reaction of the electrode with the gas phase or Na_2O_2).

Above 250 °C, a drastic increase of the total conductivity of Na_2O_2 as well as a change in the transport mechanism ($E_a = 0.18$ eV) is observed (solid squares in Figure 3.19b). A small endothermic peak can be seen in the DSC curve between 260 and 280 °C (Figure 3.20a). However, according to ref.^[119] the Raman spectrum of Na_2O_2 undergoes no changes up to 507 °C other than peak broadening and shift to

lower frequencies as it is expected for increasing temperatures. At 507 °C, the two internal peroxide stretching modes collapse to a single peak indicating that a crystallographic phase transition is taken place at this temperature. In situ Raman spectroscopy performed for the present thesis in a stainless steel sample holder under nitrogen confirms that the two distinct crystallographic peroxide sites are maintained in Na₂O₂ at least up to 350 °C (Figure 3.20b). In situ XRD above 250 °C failed because the thin quartz capillary reacted with the sample.

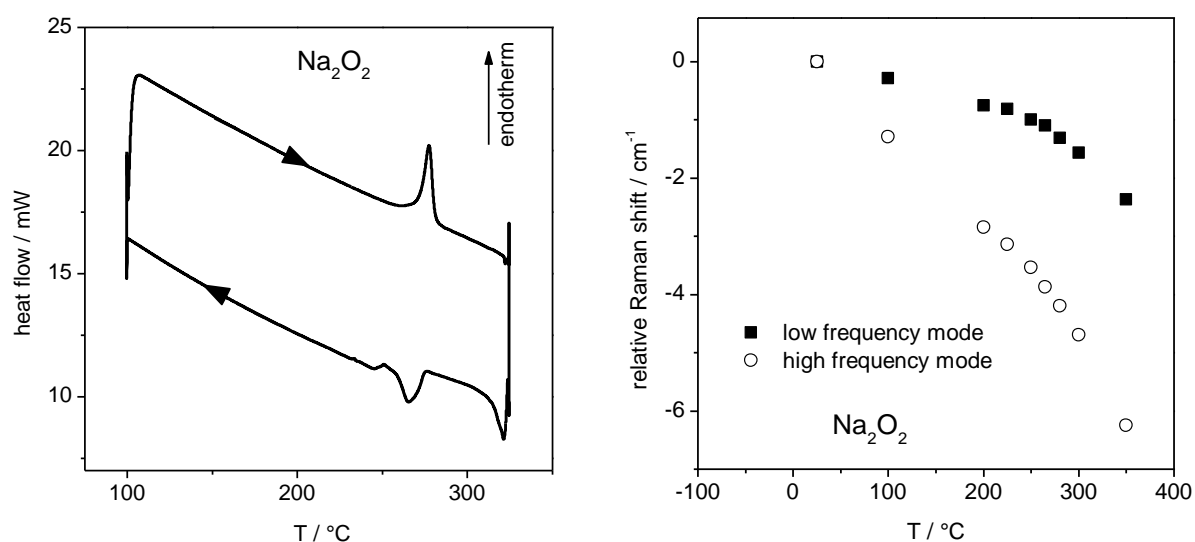


Figure 3.20: Temperature dependence a) of the heat flow (DSC) of Na₂O₂ encapsulated in gold foil under argon and b) of the Raman frequency change relative to room temperature of Na₂O₂ in nitrogen.

The change in the conductivity mechanism is therefore likely not an intrinsic property of Na₂O₂, but rather related to eutectic melting of Na₂O₂ with impurities as previously observed for NaOH.^[120] By rapid synthesis and measurement (with the oxidation of Na metal in O₂, the pressing of the pellet, the electrode coating and the conductivity measurement all performed inside a glove box), it is temporarily possible to obtain the conductivity of very phase pure Na₂O₂ at higher temperatures that is in agreement with the temperature dependence and high activation energy of > 1 eV at low temperatures (open circle in Figure 3.19b). But even in highly pure argon (< 0.1 ppm H₂O) Na₂O₂ reacts with any trace impurities in the gas phase and the conductivity drifts within an hour to the value corresponding to the eutectic melt. Thus, although Na₂O₂ is thermodynamically stable up to its melting point $T_m \approx 675$ °C^[99], the temperature range of electrochemical investigation is limited to about 250 °C as the transport properties are influenced by impurities at higher temperatures.

3.2.3 Defect Chemistry

Unless kinetically frozen or fixed by dopants, the concentration of the point defects varies with the control parameter pO_2 and its dependence reflects the underlying defect chemistry. In Na_2O_2 the ionic conductivity depends on the pO_2 with a slope of $\approx -0.04 \pm 0.01$ in the $\log\sigma_{ion}$ vs. $\log pO_2$ plot (Figure 3.21b). The slight increase of the ionic conductivity with decreasing pO_2 points to positively charged defects as main ionic charge carriers, namely to sodium interstitials as the defect is reversible at the sodium lead alloy electrode but blocked at the platinum electrode. However, the pO_2 dependence is only weak and the formation of spatially demanding sodium interstitials seems at least questionable in the Na_2O_2 structure with sodium ions being located close to the positions of a hexagonal closest packing (Figure 3.17). On the other hand, the elongated shape of the peroxide ion might also favor a double occupation of a sodium ion site.

The nature of the dominating sodium defect was further addressed by determining the change in the conductivity upon doping. As with lithium peroxide, the homogenous introduction of excess negative charges seems unlikely in sodium peroxide. In contrast, any cation with a charge > 1 on the sodium ion site and halides on the peroxide site introduce excess positive charges and acts as donor dopant. The best size match is obtained with Ca^{2+} as replacement for Na^+ (crystal radii in sixfold coordination: 116 ppm for Na^+ and 114 ppm for Ca^{2+}).^[107] At first, the following preparation methods were tried to introduce the dopant. 1) sodium metal and 2 at.% calcium metal were annealed for 5 hours at 850 °C in an arc welded, closed tantalum container under argon. The calcium alloyed sodium was oxidized to sodium peroxide in 1 bar pO_2 at 350 °C. The calcium concentration was up to 4000 ppm according to the chemical analysis with ICP-OES. 2) Sintering of uniaxially pressed pellets of Na_2O_2 and 10 at.% CaO (99.99 %) mixed powders on MgO single crystals as support at 650°C in 1 bar pO_2 for 12 hours. However, both preparations did not lead to samples with conductivities significantly different than those made of nominally undoped Na_2O_2 . Apparently, calcium was not or not homogeneously incorporated into the sodium peroxide lattice. Samples of Na_2O_2 sintered with 10 at.% CaO showed both phases in the XRD pattern.

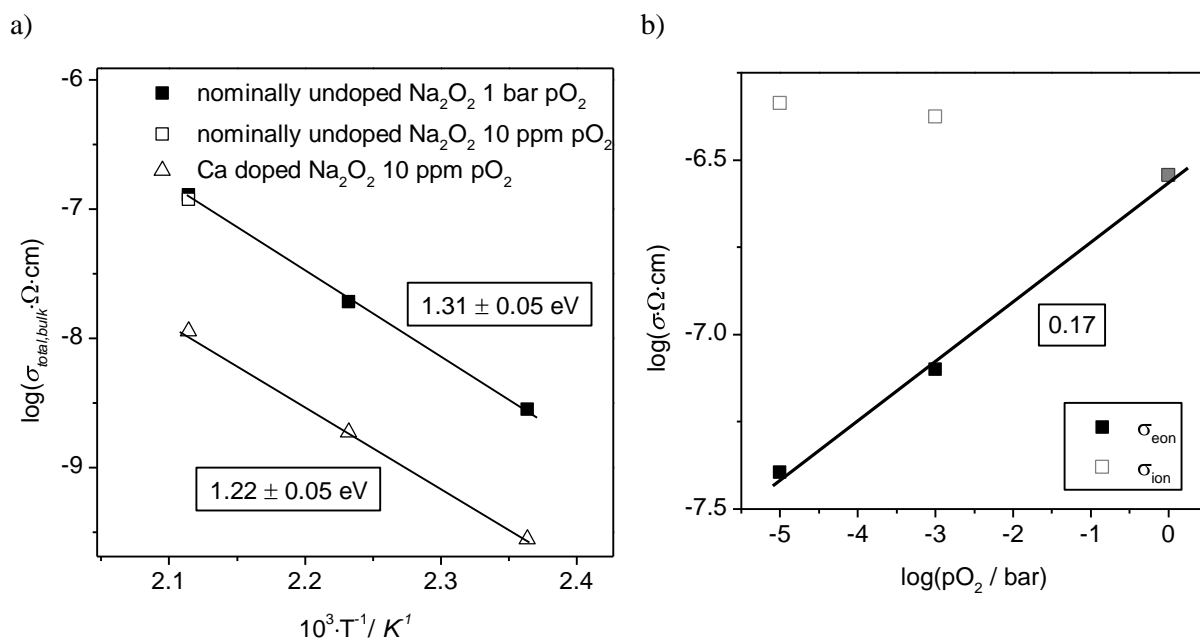
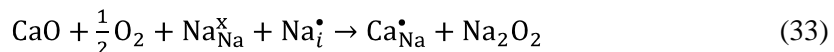
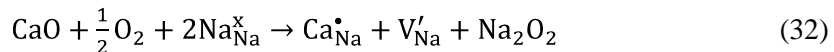


Figure 3.21:a) Temperature dependence of the bulk conductivity of nominally undoped Na_2O_2 (squares) and Ca doped Na_2O_2 obtained from a mixture of 10 wt. % CaO and Na_2O_2 (open triangles, Ca doped Na_2O_2 obtained from CaO | Na_2O_2 | CaO results in a comparable bulk conductivity) both sintered at 450 °C for 36 hours and quenched to room temperature and b) $p\text{O}_2$ dependence of the electronic and ionic conductivity of Na_2O_2 (previously sintered at 475 °C for 10 h) at 200 °C.

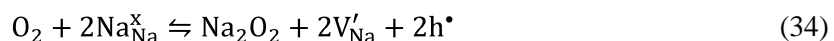
In a second attempt, the preparation 2) was modified as follows: uniaxially pressed pellets of a) Na_2O_2 and 10 at. % CaO and b) CaO | Na_2O_2 | CaO were annealed for 36 h at 450 °C in 1 bar $p\text{O}_2$ on a magnesium single crystal as support and quenched to room temperature with water as cooling medium. Since nominally pure Na_2O_2 undergoes a crystallographic phase transition around 507 °C^[119], which may have led to the disintegration of the sintered pellets upon quenching, the annealing temperature was lowered from 650 °C to 450 °C. The quenching of the pellets was supposed to freeze in the calcium concentration equilibrated in contact with CaO at 450 °C. The initial idea was to remove the CaO layers of the CaO | Na_2O_2 | CaO sandwich after sintering by grinding it down with sand paper, but it turned out that they can be removed already by applying small shear forces with a pair of tweezers (the physical contact between CaO and Na_2O_2 is very poor after quenching, possibly because of different thermal expansion coefficients).

The ionic conductivity of doped samples prepared according to the modified method a) and b) is more than half order of magnitude lower than of nominally pure Na_2O_2 with the same thermal history (Figure 3.21a). No significant change in the lattice constants is observed by XRD as well as in the FWHM and frequency of the peroxide stretch vibration by Raman spectroscopy. The insertion reaction of Ca^{2+} into the Na_2O_2 lattice can be expressed as follows for charge compensation by sodium vacancies (equation (32)) and sodium interstitials (equation (33)):



Although the reactions are expected to be in thermodynamic equilibrium at annealing temperatures, they are frozen in at low temperatures and thus shown with one direction reaction arrows. According to equation (33), sodium interstitials are annihilated by the incorporation of calcium ions on a sodium ion site. Hence, the decrease of the conductivity in the donor doped samples supports the indication from the $p\text{O}_2$ dependence of the ionic conductivity that sodium interstitials are the main ionic charge carrier in sodium peroxide. The activation energy of the ionic conductivity (sum of formation and migration enthalpy) is not altered by doping. The contribution of the formation enthalpy is therefore already negligible in the as prepared Na_2O_2 , i.e. the concentration of sodium defects are fixed by impurities. The defect concentrations are more likely controlled by donor impurities (namely alkaline earth metal cations on sodium sites) than by acceptor impurities leading to a higher concentration of sodium vacancies than sodium interstitials. This finding suggests that the sodium vacancy mobility is very low compared to the mobility of sodium interstitials.

The electronic conductivity σ_{con} exhibits a distinct $p\text{O}_2$ dependence and decreases with decreasing $p\text{O}_2$ (in the range $p\text{O}_2 = 1 - 10^{-5}$ bar) as expected for p-type conductivity (Figure 3.21b). The actual slope of $\log\sigma_{\text{con}}$ vs. $\log p\text{O}_2$ of 0.17 is, however, closer to the one predicted for the oxygen exchange reaction



in the undoped case (slope 1/4, with the electroneutrality condition $\text{h}^{\bullet} = \text{V}'_{\text{Na}}$ than for the one in the donor doped case (slope 1/2, with the electroneutrality condition $\text{D}^{\bullet} = \text{V}'_{\text{Na}}$).

As already observed in Li_2O_2 , also Na_2O_2 shows a weak signal at $g = 2.008$ in the EPR spectrum at 120 K, which can be assigned to isolated superoxide (< 0.1 ppm) (blue curve in Figure 3.22a). Mechanical activation by ball milling treatment introduces considerable disorder into the Na_2O_2 lattice as indicated by the increase of the FWHM of the Raman peaks from 6 to about 30 cm^{-1} (Figure 3.16b). The concentration of superoxide defects is greatly enhanced to about 4 ppm according to EPR spectroscopy (black curve in Figure 3.22a).

Both ionic and electronic conductivities are increased by more than an order of magnitude (Figure 3.22b) by ball milling. In the figure, the isostatically pressed ball milled Na_2O_2 is compared against isostatically pressed as prepared Na_2O_2 in order to discriminate the ball milling effect against the pronounced current constriction phenomena occurring in unsintered samples. However, it cannot be entirely ruled out that the measured apparent electronic conductivity in this pellet with about 20%

porosity actually reflects circuiting of the electronic pathway by sodium ion diffusion coupled with enhanced gas phase reaction rate.

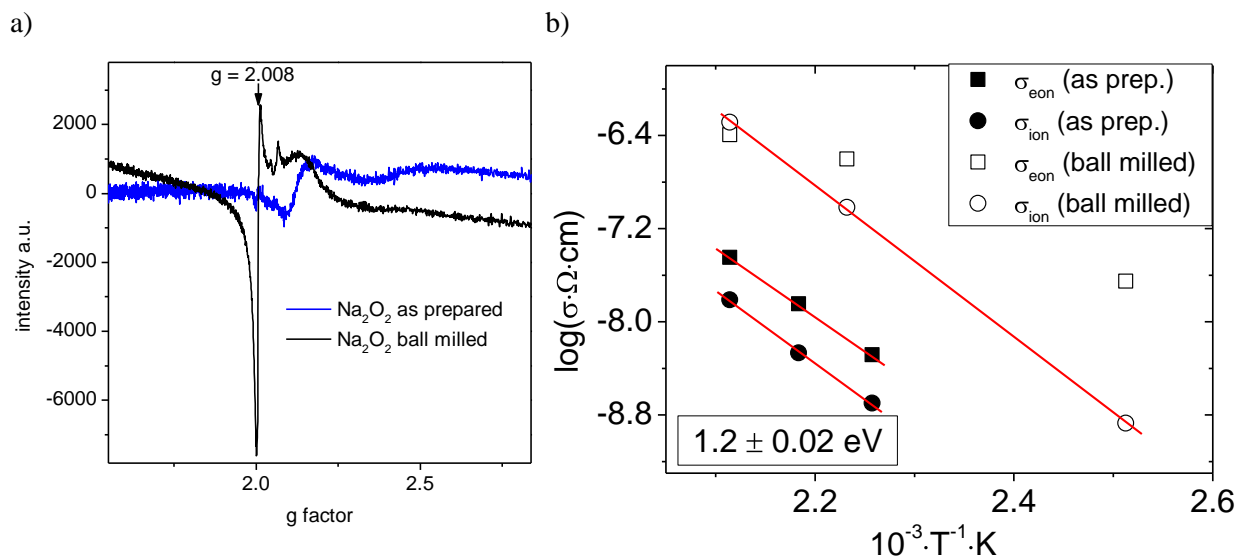


Figure 3.22: a) EPR spectra of as prepared and ball milled Na_2O_2 at 120 K (the broad signal at $g = 2.1$ can be assigned to the quartz capillary and b) temperature dependence of the electronic and ionic conductivity of isostatically pressed as prepared and ball milled Na_2O_2 .

3.3 Potassium Peroxide

3.3.1 Chemical characterization

The Raman spectrum of as prepared K_2O_2 exhibits external modes between 100 and 250 cm^{-1} , two Raman active internal modes at 746 (weak) and 761.5 cm^{-1} (strong), the symmetric carbonate stretching at 1063 cm^{-1} and the peroxide stretching overtone at 1508 cm^{-1} (Figure 3.23a). Ball milling of K_2O_2 creates substantial disorder in the lattice as the full width half maximum of the peroxide stretching increases from about 3 to 7 cm^{-1} . The peroxide stretching at 761.5 cm^{-1} seems to shift to a lower frequency at 759 cm^{-1} . This red shift implies a decrease in the force constant of the covalent oxygen bond, in contrary to what is observed for ball milled Li_2O_2 and Na_2O_2 . The decrease of the peroxide bond strength seems to be a result of a ball milling induced phase transition. According to the XRD pattern, ball milling led to a new crystallographic phase of K_2O_2 not reported in the literature so far (Figure 3.23b).

The following cation impurities were found in K_2O_2 by chemical analysis (ICP-OES): 2000 ppm sodium, 20 ppm lithium and 20 ppm barium.

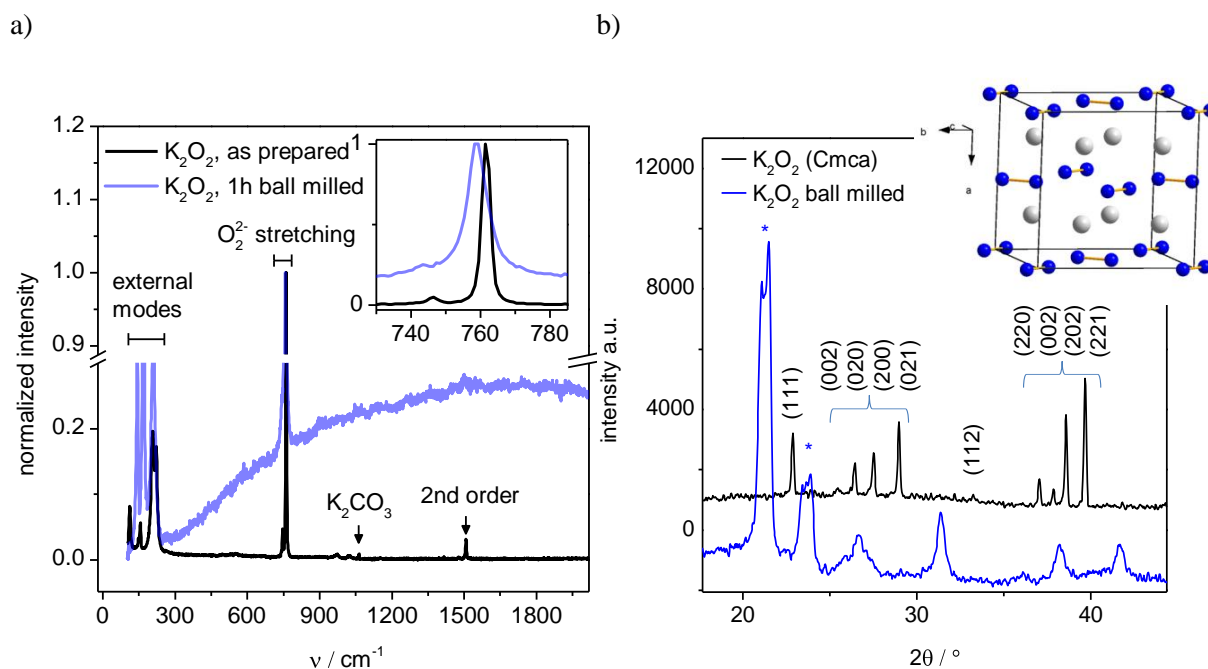


Figure 3.23: a) Raman spectra of as prepared (black, the assignment of the external and internal modes of K_2O_2 is based on ref. ^[91]) and 1 h ball milled (blue) K_2O_2 and b) XRD pattern of as prepared (black) and 1 h ball milled (blue) K_2O_2 . The reflections of as prepared K_2O_2 are indexed in black, the blue asteriks mark peaks in b) which belong to the sample holder. The inset shows the orthorhombic crystal structure of K_2O_2 (oxygen in blue, potassium in grey) based on XRD data of K_2O_2 single crystals from ref. ^[121].

3.3.2 Thermodynamic Stability of K_2O_2

The thermodynamic stability window of K_2O_2 sets the upper and lower limits of temperature and oxygen partial pressure at which its electrical transport properties can still be studied. At high oxygen partial pressures and low temperatures, the superoxide KO_2 is the thermodynamically stable phase, while at low oxygen partial pressures and high temperatures, the fully reduced oxide K_2O is the stable phase. High temperatures $> 400\text{ }^\circ\text{C}$, at which the phase boundary to the oxide might limit the characterization of K_2O_2 (Figure 3.24a), were not accessible for electrochemical investigations anyway as the pellets are severely plastically deformed already by the force of the spring pressing the platinum contacts on the sample at such temperatures. The thermodynamic stability of K_2O_2 versus KO_2 at lower temperatures calculated from thermochemical data is shown in Figure 3.24b. It is noteworthy that the boundary between the peroxide and the superoxide runs exactly through the $p\text{O}_2$ - T window that is practical and applicable for electrochemical investigations. On the one side, this means that the range for determining the $p\text{O}_2$ of the conductivities of K_2O_2 is rather narrow compared to Li_2O_2 and Na_2O_2 and limited to reducing conditions with $p\text{O}_2 < 100\text{ ppm}$. On the other side, it provides the opportunity not only to look into the electrical transport in potassium peroxide but also in the corresponding superoxide (see section 3.4).

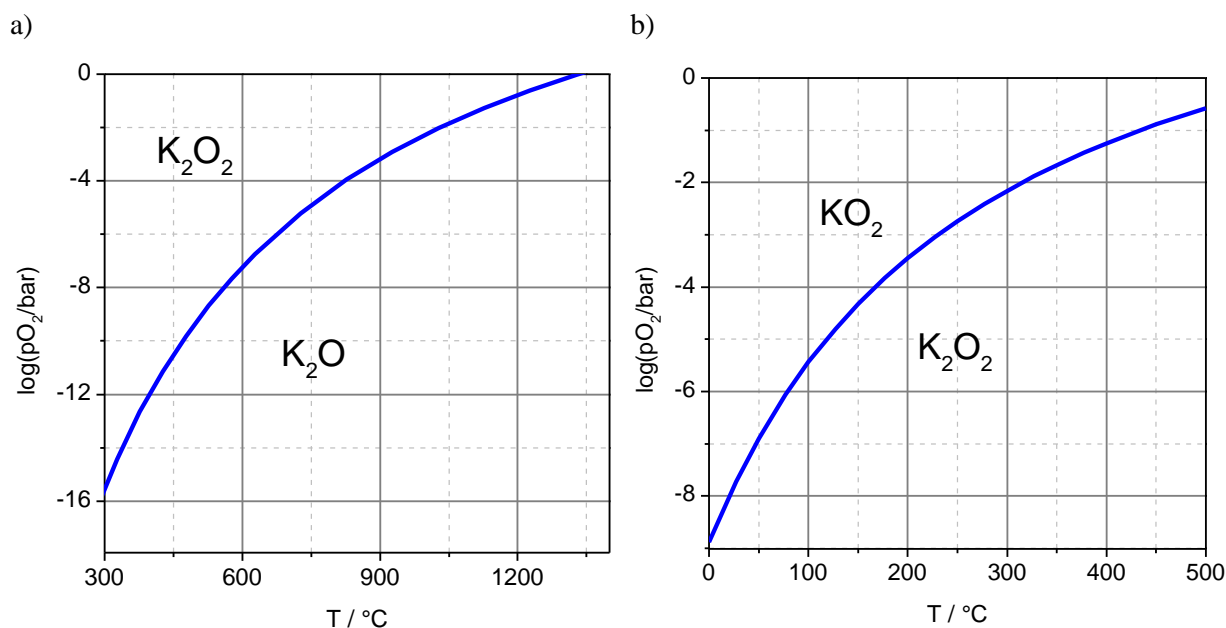


Figure 3.24: Thermodynamic stability of K_2O_2 a) vs. K_2O and b) vs. KO_2 calculated according to thermochemical data published in ref.^[92].

3.3.3 Electrochemical characterization

The impedance spectrum of potassium peroxide with ionic blocking gold electrodes in Figure 3.25a consists of a bulk ($\epsilon \approx 22$) and an electrode contribution. The ionic transference number is > 0.9 at 300 $^\circ\text{C}$ and 10 ppm pO_2 . At these conditions, K_2O_2 can be considered as thermodynamically stable against KO_2 . The electrode contribution in the impedance spectrum of cell $KPb | K_2O_2 | KPb$ is decreased compared to $Au | K_2O_2 | Au$ but does not drop to zero (Figure 3.25b). The KPb electrode (actually a mixture of the intermetallic compounds KPb and K_2Pb_3) is assumed to be reversible for both potassium ions and electronic charge carriers, whereas potassium has to dissolve at the negative pole and deposit on the positive pole to maintain continuous oxygen transport (according to the reaction $K_2O_2 + V_{O_2}^{\bullet\bullet} + 2e^- \rightleftharpoons O_{2O_2}^x + 2K$), which may result in a higher electrode resistance. Thus, the remaining electrode polarization suggests that the conductivity of oxygen species is not negligible in potassium peroxide.

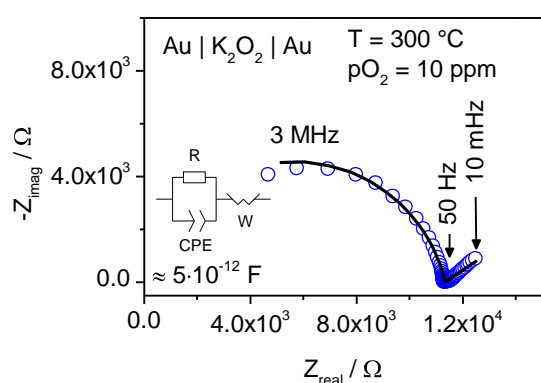
In order to sustain this conclusion, it has to be established a) that the electrode and potassium peroxide have not reacted to a layer blocking electrons or potassium ions and b) that the KPb electrode is truly reversible for both potassium ions and electronic charge carriers. There is no evidence in the impedance spectrum for the formation of a blocking layer between K_2O_2 and KPb . Furthermore, as shown in Figure 3.25c, the electrode polarization is also observed for a fresh pellet $KPb | K_2O_2 | KPb$ already in the temperature range 100 – 150 $^\circ\text{C}$ in 10 ppm pO_2 . The reaction between the electrode and the sample should be significantly more sluggish at these low temperatures. Although these

measurements conditions could be already outside the thermodynamic stability window of K_2O_2 , there is no formation of KO_2 as revealed by the absence of its characteristic yellow color on the pellets after the measurement. KPb electrodes have a negligible electronic resistance compared to K_2O_2 at the measurement temperatures. Its reversibility towards potassium ions can be verified by replacing K_2O_2 by a known potassium conductor, such as potassium iodide. The cell $KPb | KI | KPb$ exhibits no electrode polarization (at the measured temperatures 200 – 300 °C) as expected for a reversible electrode (Figure 3.25d).

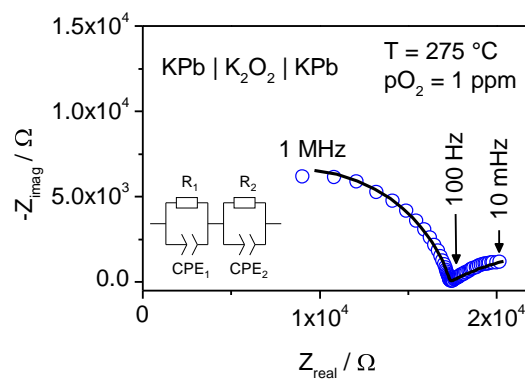
Hence, these findings support that there is appreciable transport of anions in potassium peroxide. The temperature dependence of the total conductivity as obtained from the abscissa intercept of the bulk response in the impedance spectrum (measured in pure nitrogen with $pO_2 < 1$ ppm to avoid oxidation to KO_2) is depicted in Figure 3.26a. The activation energy is 0.97 ± 0.03 eV. The chemical diffusion coefficient of potassium peroxide is about $D^\delta = 8 \cdot 10^{-8}$ cm/s² at 300 °C and 10 ppm pO_2 according to the exponential long time relaxation of the dc polarization of the cell $Au | K_2O_2 | Au$ (Figure 3.26b).

The electronic conductivity obtained from the stationary state is decreasing upon switching from 10 to 1 ppm pO_2 in accordance with p-type (hole) conductivity, but the equilibration kinetics is too sluggish to obtain a stationary state of the exponential decay within reasonable waiting times. The gold electrodes have possibly become porous and permeable for oxygen at the temperature of 300 °C. Nevertheless, short circuiting leakage currents via the gas phase are considered unlikely, exactly because of the slow equilibration process upon changing pO_2 , which should only depend on the reactor flush time in such a case, and since the density of the pressed pellets is close to the theoretical density.

a)



b)



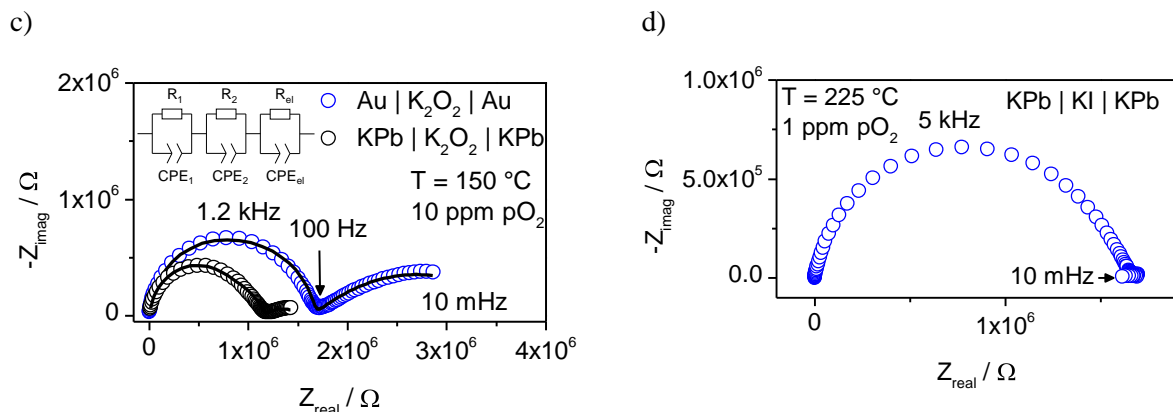


Figure 3.25: Impedance spectrum of a) Au | K₂O₂ | Au at 300 °C in 10 ppm pO₂, b) KPb | K₂O₂ | KPb at 275 °C and 1 ppm pO₂, c) Au | K₂O₂ | Au (blue) and KPb | K₂O₂ | KPb (black) at 150 °C and 10 ppm pO₂ and d) KPb | KI | KPb at 225 °C and 1 ppm pO₂.

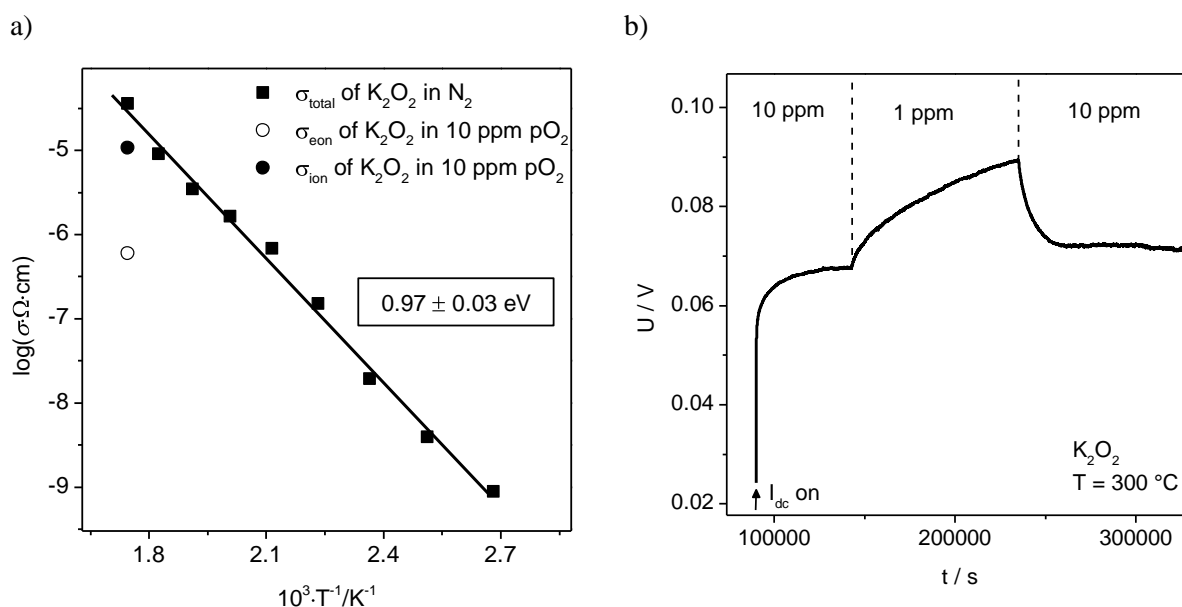
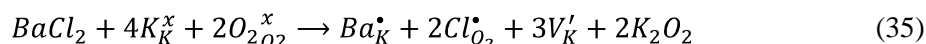


Figure 3.26: a) Temperature dependence of the total bulk conductivity of K₂O₂ in nitrogen (< 1 ppm pO₂) and b) dc polarization of the cell Au | K₂O₂ | Au at 300 °C and 10 ppm pO₂ with $I = 2 \cdot 10^{-6}$ A and conductivity relaxation after switching from 10 ppm to 1 ppm pO₂. The ionic and electronic conductivity of this cell at 300 °C and 10 ppm pO₂ is also indicated in a).

Suitable donor dopants for K₂O₂ are barium ions replacing potassium ions (crystal radii in sixfold coordination: 152 ppm for K⁺ and 149 ppm for Ba²⁺^[107]) and chloride replacing peroxide (cf. section 3.1.3). To see if any doping effect can be achieved in K₂O₂, BaCl₂ was chosen as starting material for doping as both anion and cation sites can be supplied with donors in one preparation. Sandwich pellets of BaCl₂ | K₂O₂ | BaCl₂ were uniaxially pressed with 250 MPa as well as pure pellets of K₂O₂ as reference and annealed at 400 °C in ≤ 1 ppm pO₂ on MgO single crystals as support. At a higher annealing temperature the incorporation of dopants into K₂O₂ should be more effective (both thermodynamically and kinetically), but these were avoided since perceptible viscosity of K₂O₂ and plastic deformation of its pellets was observed at 450 °C. After 36 hours of heat treatment, the setup

was quenched to room temperature in ice water. The white BaCl_2 layers were chipped off with a pair of tweezers. The remaining pellet was polished from all sides with sand paper to remove any white traces on the beige sintered K_2O_2 pellet. The thorough removal of BaCl_2 in particular on the sides of the pellet is important as its conductivity is reportedly two orders of magnitude higher (and even more when it is potassium doped as has to be expected here) than the conductivity of K_2O_2 as measured in the present work.^[122]

The doping by BaCl_2 results in donor doping no matter, whether only Ba^{2+} or Cl^- or both Ba^{2+} and Cl^- are incorporated substitutionally (for K^+ and O_2^{2-} respectively):



The ionic conductivity is expected to increase upon donor doping only in the case that the charge transport proceeds primarily via potassium vacancies. In contrast, potassium interstitials and peroxide vacancies are depleted by introducing excess positive charges and their conductivities are expected to decrease.

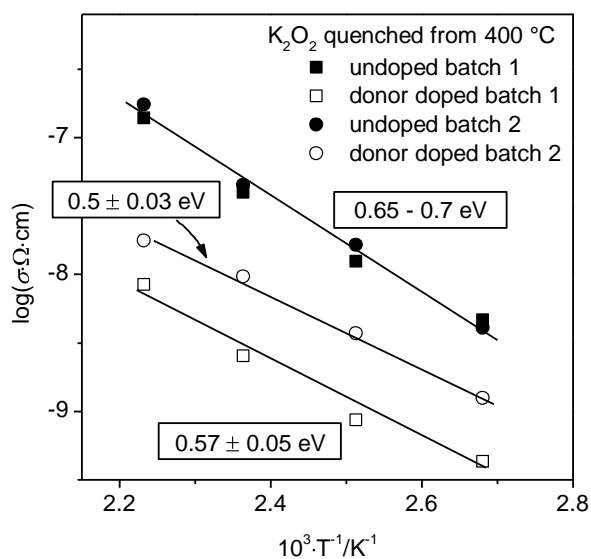


Figure 3.27: Temperature dependence of the total bulk conductivity of nominally undoped K_2O_2 (solid symbols) and BaCl_2 doped K_2O_2 (open symbols) in 10 ppm pO_2 . The pellets were previously sintered at 400 °C for 36 h and quenched to room temperature. Samples from the same batch were annealed at the same time in the same setup and have thus the same thermal history.

The temperature dependence of the total bulk conductivity of doped and nominally undoped K_2O_2 samples with the same thermal history (400 °C for 36 h and quenched to room temperature) in Figure 3.27 shows that two effects are prevailing. First of all, the heat treatment itself results in an increase of the conductivity by about 1 order of magnitude and decrease of the activation energy from about 0.97 ± 0.03 eV to $0.65 - 0.7$ eV (cf. Figure 3.26). A possible effect of the annealing could be the removal of impurities, which are kinetically frozen at lower temperatures. However, moving from the extrinsic (impurity controlled) to the intrinsic regime would result in an increased activation energy as

thermally activated defect formation would become more relevant. Secondly, donor doping decreases the conductivity by about 1 order of magnitude, which is in agreement both with transport via potassium interstitials and peroxide vacancies.

3.4 Potassium Superoxide

3.4.1 Chemical characterization and Crystallographic Structure

According to the Raman spectrum of potassium superoxide (Figure 3.28a), the frequency of the oxygen stretch (and with it the strength of the oxygen bond) is shifted to a higher value (1144 cm^{-1}) compared to potassium peroxide (716.5 cm^{-1}), as it is expected from the decrease of the number of electrons in the anti-binding π^* orbitals according to the molecular orbital theory (cf. Figure 1.1). Ball milling of KO_2 leads to a slight increase in the oxygen bond length and a small new peak emerges at about 759 cm^{-1} . The frequency corresponds to the peroxide stretch vibration of the emerging new K_2O_2 phase already observed in the previous section on ball milled potassium peroxide.

The tetragonal CaC_2 type structure stable at room temperature (Figure 3.29) transforms into a cubic rock salt type modification at higher temperatures. The temperature of the phase transition has been estimated as 60 to $150\text{ }^\circ\text{C}$.^{[123],[124]} Temperature dependent Raman measurements of KO_2 under 1 bar oxygen performed in this study indicate a blue shift of the superoxide stretch vibration beginning at about $100\text{ }^\circ\text{C}$ and a further increasing frequency with increasing temperature (1147.5 cm^{-1} at $125\text{ }^\circ\text{C}$ and 1151 cm^{-1} at $250\text{ }^\circ\text{C}$).

The main cation impurities in as prepared potassium superoxide are sodium (700 ppm) and lithium (10 ppm) according to the chemical analysis by ICP-OES.

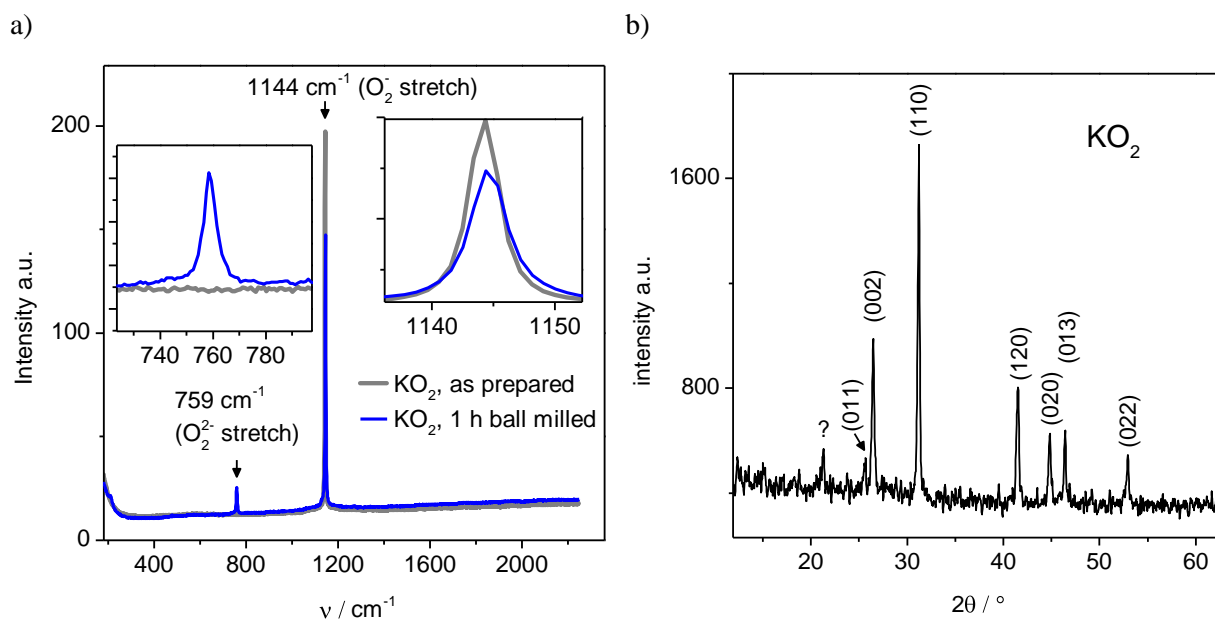


Figure 3.28: a) Raman spectra of as prepared KO_2 (grey) and 1 h ball milled KO_2 (blue) and XRD pattern of as prepared KO_2 .

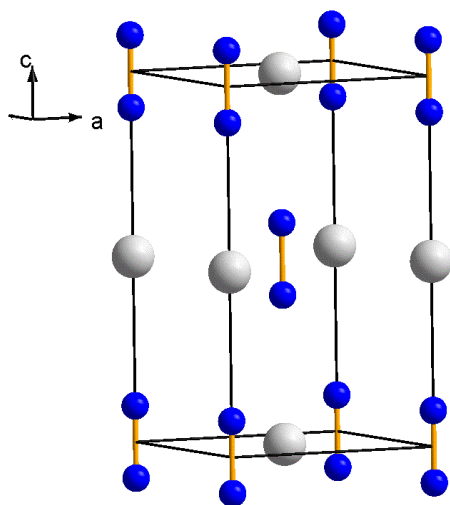


Figure 3.29: Unit cell of room temperature stable tetragonal KO_2 (potassium grey, oxygen blue) based on the x-ray diffraction data of single crystals from ref. ^[124]. No atom parameters are available for the high temperature cubic phase.

3.4.2 Electrochemical characterization

The impedance spectra of KO_2 pellets coated with gold electrodes show typically two relaxation processes (Figure 3.30a). The high frequency contribution can be assigned to the bulk with a dielectric constant $\epsilon \approx 29$. The blocking of ionic charge carriers at the gold interface gives rise to the low frequency response. The lack of current constriction for the bulk transport is consistent with a high

density already achieved upon uniaxial pressing at room temperature due to the high plasticity of the KO_2 grains.

The relative density of KO_2 pellets obtained for various uniaxial pressures is depicted in Figure 3.31. According to this, pressures of 400 - 650 MPa (applied on a commercial stainless steel tool with 12.8 mm diameter) are necessary to obtain pellets with a density close to the theoretical one. The 5 mm diameter pressing tool used in the preparation of pellets for the electrochemical characterization was loaded with maximum 250 MPa to avoid damaging the tool. In practice, the geometrically measured density of the pellets pressed with this target pressure scattered between 90 and close to 100% of the theoretical density. The variation of the density can be partly explained by uncertainties in determining size and weight of the relatively small pellets, but also by the poor control of the pressure with the employed automated hydraulic press in the glove box, which is actually designed for larger pressing tools and forces. The relatively high costs of distilled alkali metals and safety issue when dealing with these highly reactive source materials justifies taking as little sample powder as feasible for the electrochemical characterization.

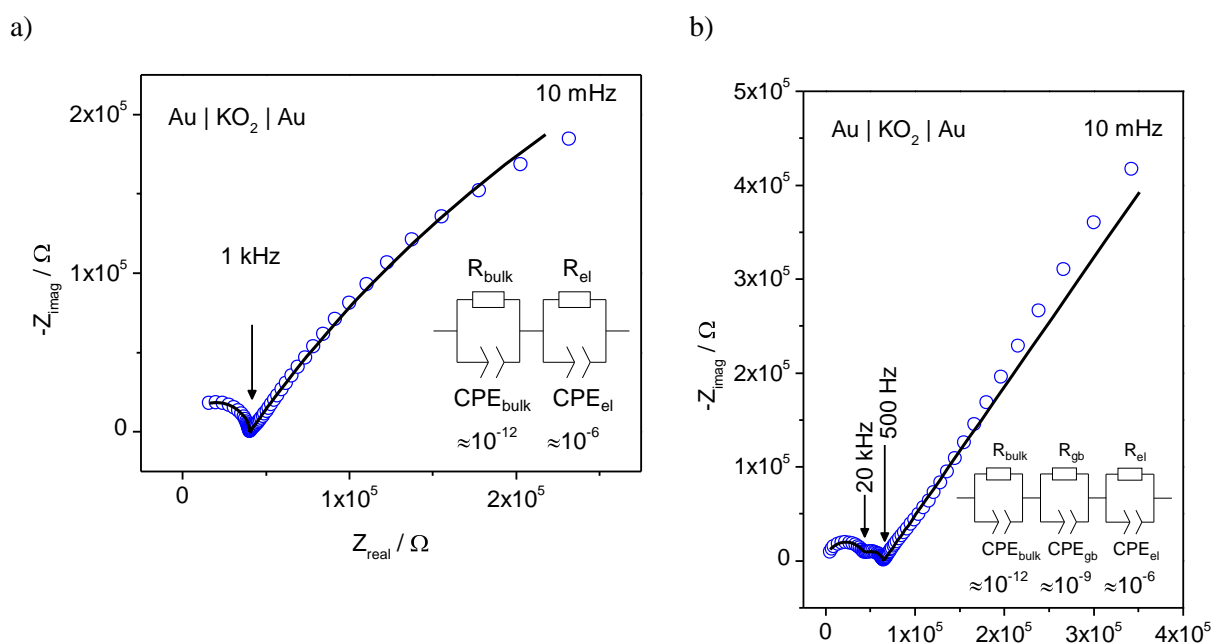


Figure 3.30: Impedance spectrum of uniaxially pressed $\text{Au} | \text{KO}_2$ (as prepared) | Au a) as typically and b) as once observed (in both cases at 225 °C, 1 bar $p\text{O}_2$ and with Au electrodes).

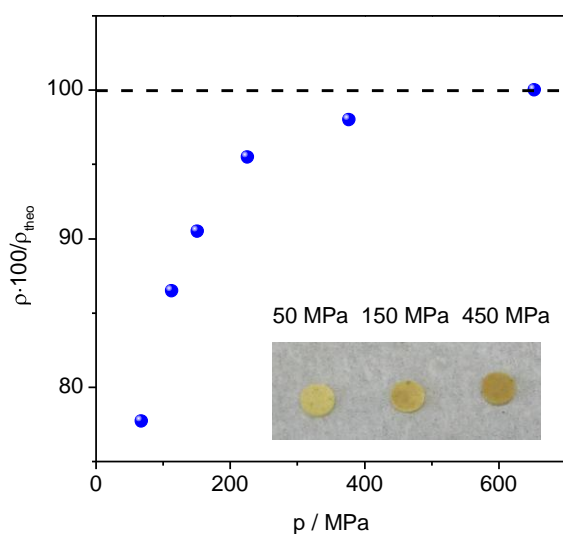


Figure 3.31: Relative density of KO_2 pellets versus applied uniaxial pressure. The experiment was performed with commercial KO_2 using a commercial stainless steel pressing tool with 12.8 mm diameter. The color changes from yellow to orange upon increasing the pressure as shown on the photograph.

Interestingly, 1 out of 10 uniaxially pressed KO_2 pellets showed an additional contribution at mid frequencies, which can be fitted with a further R-CPE element (Figure 3.30b). Its capacitance $C \approx 10^{-9}$ F is in between transport across bulk and electrode and typically for blocking grain boundaries. However, despite varying the pressure systematically (from 50 to 250 MPa with 30 s and 2 s holding time), it was not possible to identify the conditions to reproduce the morphology yielding this additional relaxation process in the impedance spectrum.

By means of dc stoichiometry polarization measurement of the cell $\text{Au} | \text{KO}_2 | \text{Au}$ (Figure 3.32), the conductivity of the ionic charge carriers (blocked at the gold electrode) was separated from the apparent electronic conductivity (more precisely, the conductivity of charge carriers not polarized at the gold electrode). For uniaxially pressed pellets of as prepared KO_2 not subjected to a further heat treatment (Figure 3.33a), the ionic conductivity is independent of the $p\text{O}_2$ in the range 1 bar to 1000 ppm (to avoid possible decomposition to the peroxide, the pellet was not exposed to $p\text{O}_2$ values < 1000 ppm, cf. Figure 3.24). The behavior changes drastically when the pellet is sintered for 12 hours at 450 °C in 1 bar oxygen partial pressure and a strong $p\text{O}_2$ dependence of the ionic conductivity is observed with a slope of -0.47 ± 0.04 at 250 °C (Figure 3.33b). XRD and Raman spectroscopy reveal no significant differences between as prepared and annealed KO_2 . In both cases, the apparent electronic conductivity is increasing with decreasing $p\text{O}_2$ with a slope of 0.16 and 0.12 ± 0.02 .

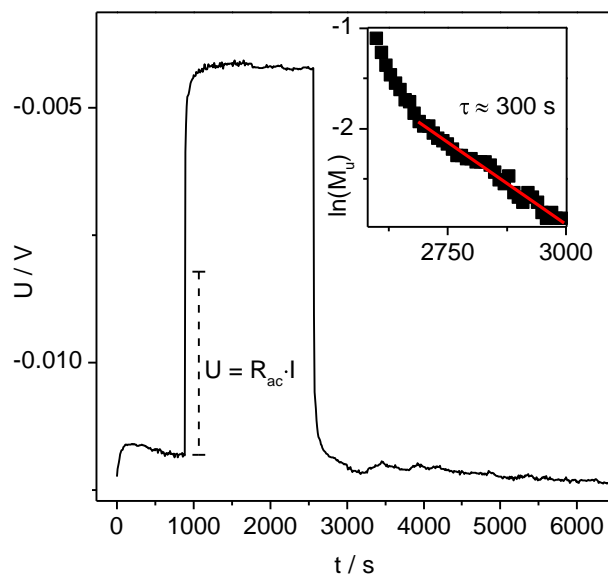


Figure 3.32: Dc polarization measurement of Au | KO₂ (annealed) | Au at T = 225 °C and 1000 ppm pO₂. The inset shows the linear fit of $\ln M_u$ (logarithm of the normalized voltage) vs. time for long depolarization times.

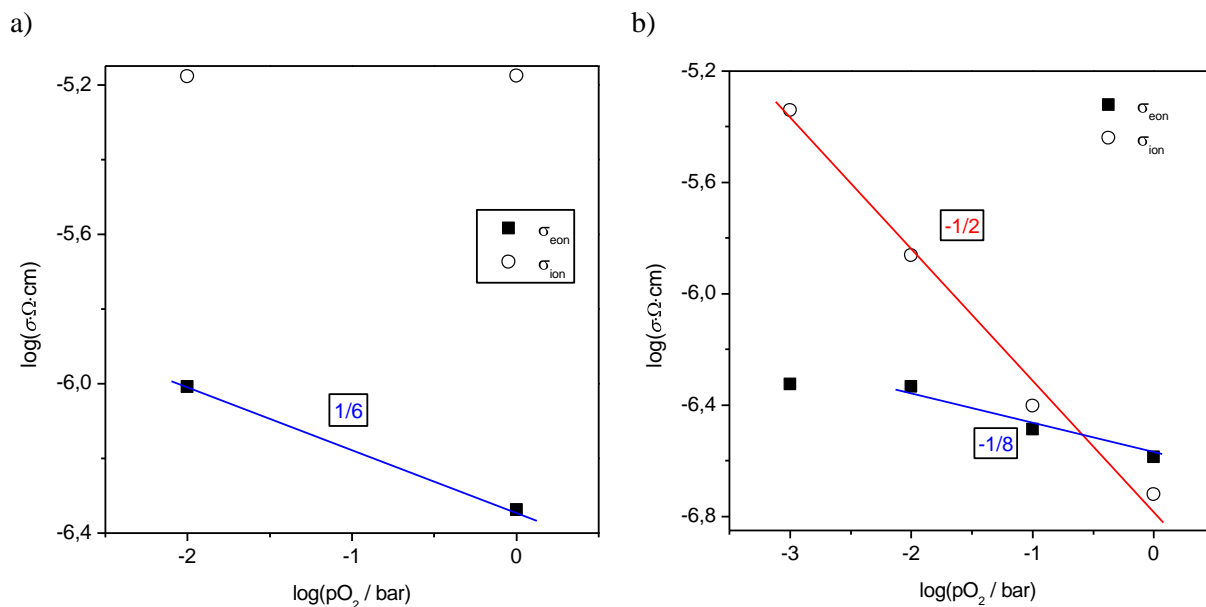


Figure 3.33: pO₂ dependence of electronic and ionic conductivity of Au | KO₂ | Au at 250 °C of a) as prepared KO₂ and b) 450 °C annealed KO₂.

The basic defect reactions that may take place in alkali superoxides, their mass actions laws as well as the electroneutrality condition are listed in Table 3.7 – band reaction, Schottky reaction, Frenkel reaction, formation of an oxide defect and formation of superoxide vacancies upon releasing oxygen. For analytical expressions of the pO₂ dependences of the defect concentrations, the electroneutrality condition needs to be simplified so that only one defect remains on each side of the equation (Table 3.8). The pO₂/metal activity dependence of the relative defect concentrations (for the absolute values, the mass action constants have to be known) are conveniently illustrated in the Kröger-Vink diagrams in Figure 3.34 and Figure 3.35.

It is noteworthy that the commonly observed negative relation between electronic conductivity and oxygen partial pressure is inverted in alkali superoxides when the condition of electroneutrality is governed by the oxide defect. In such a case, the electronic conductivity is expected to increase with increasing pO_2 . The number of electrons annihilated by the incorporation of oxygen is less than the number of electrons created by the annihilation of oxide defects due to the depletion of superoxide vacancies upon increasing pO_2 .

Table 3.7: Basic defect chemical reactions, mass action laws and electroneutrality condition for alkali superoxides

Band reaction	$0 \rightleftharpoons e' + h^\bullet$	$K_B = n \cdot p$
Schottky reaction	$M_M^x + O_2 O_2^x \rightleftharpoons V'_M + V^\bullet_{O_2} + MO_2$	$K_S = V'_M \cdot V^\bullet_{O_2}$
Frenkel reaction	$M \rightleftharpoons V'_M + M_i^\bullet$	$K_F = V'_M \cdot [M_i^\bullet]$
Oxide defect	$O_2 O_2^x + V^\bullet_{O_2} + 3e' \rightleftharpoons 2O'_{O_2}$	$K_O = \frac{O'^2_{O_2}}{V^\bullet_{O_2} \cdot n^3}$
Gas phase reaction	$O_2 O_2^x \rightleftharpoons V^\bullet_{O_2} + O_2(g) + e'$	$K_G = V^\bullet_{O_2} \cdot n \cdot p_{O_2}$
Electroneutrality condition	$n + V'_M + O'_{O_2} + O_2 O_2^x + A' = p + M_i^\bullet + V^\bullet_{O_2} + D^\bullet$	

Table 3.8: Oxygen partial pressure dependence of the basic defects in alkali superoxides. The numbers in the table indicate the exponent y in the relation $[\text{defect}] \sim pO_2^y$ for the various majority carrier situations.

Approx. neutrality condition	$[V'_M] = V^\bullet_{O_2}$ $V'_M = M_i^\bullet$ $V'_M = D^\bullet$ $A' = V^\bullet_{O_2}$ $A' = M_i^\bullet$	$O'_{O_2} = D^\bullet$	$O'_{O_2} = V^\bullet_{O_2}$ $O'_{O_2} = M_i^\bullet$	$n = V^\bullet_{O_2}$ $n = M_i^\bullet$ $[V'_M] = p$	$n = D^\bullet$ $n = p$
n	-1	+1/2	-1/4	-1/2	0
p	+1	-1/2	+1/4	+1/2	0
$V^\bullet_{O_2}$	0	-3/2	-3/4	-1/2	-1
V'_M	0	+3/2	+3/4	+1/2	+1
M_i^\bullet	0	-3/2	-3/4	-1/2	-1
$[O'_{O_2}]$	-3/2	0	-3/4	-1	-1/2

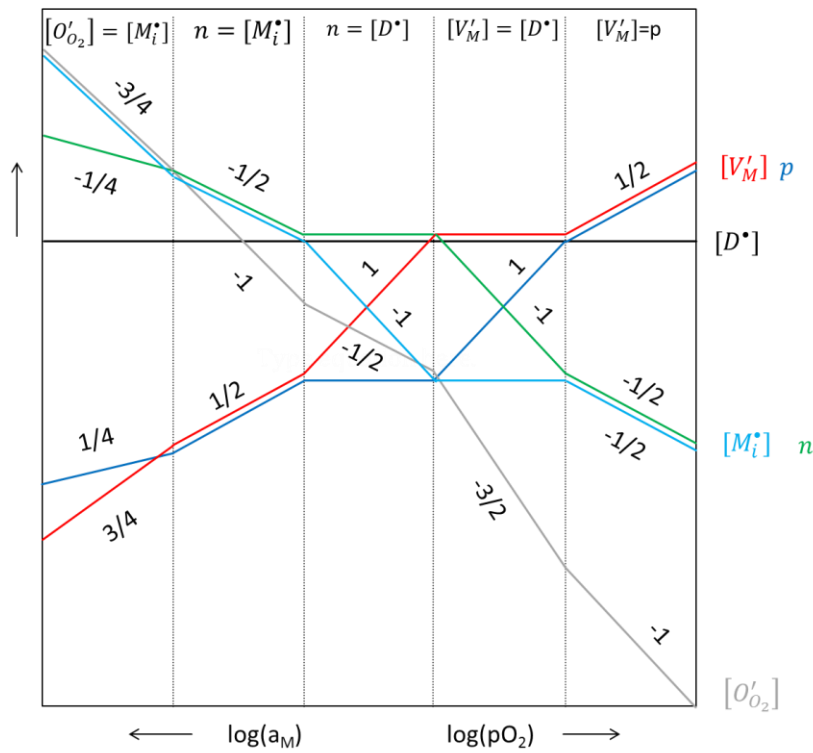


Figure 3.34: Dependence of defect concentrations on pO_2 and metal activity for donor doped alkali superoxides. Note that the superoxide vacancies V'_{O_2} show the same dependence as the metal interstitial ions M'_i .

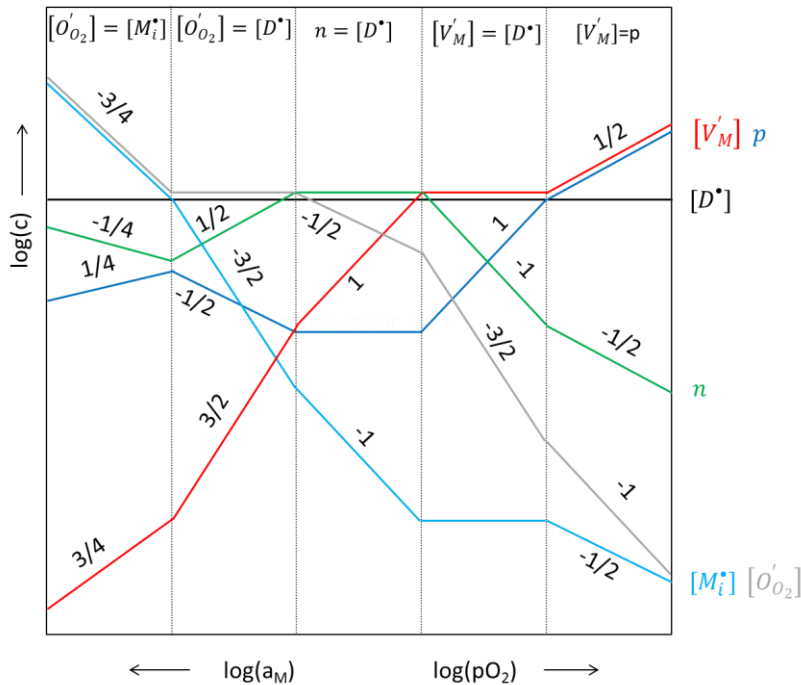


Figure 3.35: Dependence of defect concentrations on pO_2 and metal activity for donor doped alkali superoxides and the case of low formation enthalpy of the oxide defect O'_{O_2} . Note that the superoxide vacancies V'_{O_2} show the same dependence as the metal interstitial ions M'_i .

Again, not all regimes of the Kröger-Vink diagrams will be within the stability limit of the alkali superoxides and experimentally accessible (cf. Figure 3.24 and Figure 3.39). Also, electron holes p are expected to be energetically unfavourable as they would correspond either to an alkali metal with a valence of 2+ or a neutral O_2 in an ionic lattice.

The pO_2 independence of the ionic conductivity in as prepared KO_2 suggests that the main ionic charge carrier is compensated by pO_2 -independent intrinsic ionic defect formation reactions (Schottky, Frenkel) or by donor/acceptor impurities. On the other hand, the strong pO_2 dependence of the ionic conductivity in KO_2 annealed at 450 °C can only be explained by electronic compensation of ionic defects. The negative slope of the $\log\sigma_{ion}$ vs. $\log pO_2$ plot is consistent with both potassium interstitials and superoxide vacancies, but rules out potassium vacancies as main ionic charge carrier. The slopes of -0.47 ± 0.04 measured at 250 °C and -0.42 ± 0.03 measured at 225 °C coincide with the slope of $-1/2$ expected for the approximated neutrality conditions $n = V_{O_2}^{\bullet}$ and $n = M_i^{\bullet}$. The compensation of electrons by donor impurities $n = [D^{\bullet}]$ is considered less likely as it would result in a pO_2 independence of the electronic conductivity and a slope of -1 in the $\log\sigma_{ion}$ vs. $\log pO_2$ plot.

The negative slope in the pO_2 dependence of the apparent electronic conductivity corresponds to n-type conductivity, although the actual value of ≤ -0.16 considerably deviates from the slope of $-1/2$ that is expected for the intrinsic case with the electroneutrality conditions $n = V_{O_2}^{\bullet}$ or $n = M_i^{\bullet}$. Potassium superoxide is a wide band gap semiconductor with localized charges and the most reasonable electronic transport mechanism seems to be the hopping of excess electrons located on superoxides forming peroxide defects, i.e. the inverse relation of native species and electronic charge carrier as in the alkali peroxides. The presence of significant amounts of holes in alkali superoxides is discarded because of the already small electronic charge on the superoxide. Further oxidation of the superoxide would formally yield neutral molecular oxygen on a superoxide site.

A possible reason for the stark difference in the pO_2 dependence of the ionic conductivity between as prepared and annealed KO_2 could be a different level of acceptor or donor concentration, i.e. a purification of the sample by the heat treatment. As pointed out in the previous section on the chemical characterization, the main detectable cation impurities in KO_2 are lithium and sodium. These are isovalent to potassium and they should not alter the concentration of other defects. Furthermore, chemical analysis by ICP-OES of annealed KO_2 (450 °C for 10 h) shows that the concentration of the alkali impurities is in fact not affected by the annealing. On the other hand, the concentrations of possible donor impurities such as alkaline earth metals are below the detection limit of ICP-OES already in case of as prepared KO_2 and their actual concentrations before and after the annealing cannot be determined.

The temperature dependence of the total bulk conductivity of as prepared KO_2 indicates a change in the transport mechanism between 150 to 175 °C with a drop in the activation energy from 1.3 ± 0.1 to about 0.8 eV (Figure 3.36a). This cannot be explained by a transition from the extrinsic to the intrinsic regime as the high temperature transport mechanism has the lower activation energy. The behavior is, however, typical for crystallographic phase transitions. Potassium superoxide indeed changes from tetragonal to cubic above room temperature. The transition has only been poorly investigated so far and its estimated temperature ranges between 60 - 150 °C.^[124]

Potassium superoxide, which was previously annealed at 450 °C, shows the comparable low activation energy of about 0.56 eV over the entire measured temperature range 100 – 250 °C. The low activation energy is in contrast to the previous explanation that the $p\text{O}_2$ dependence of the ionic conductivity in annealed KO_2 may be due to a lower level of impurities. Furthermore, the lower ionic conductivity in annealed KO_2 cannot be explained by a frozen Schottky reaction after cooling down from 450 °C. If superoxide vacancies are the main ionic charge carrier in KO_2 , no $p\text{O}_2$ dependence of their concentration should be observed if it was fixed by a frozen Schottky reaction. On the other hand, if potassium interstitials are the dominating ionic defect, the coupling of the Frenkel reaction to the Schottky reaction predicts an increase of the conductivity of potassium interstitials upon freezing the superoxide vacancy concentration at a high value. Hence, both the low activation energy and lower ionic conductivity in annealed KO_2 compared to as prepared KO_2 cannot be explained for now.

Figure 3.36a also shows the temperature dependence of the chemical diffusivity of annealed KO_2 at 1000 ppm $p\text{O}_2$ obtained from exponential fit of the stoichiometry depolarization curve of the cell $\text{Au} | \text{KO}_2(\text{annealed}) | \text{Au}$ with an the activation energy of about 1.1 ± 0.02 eV.

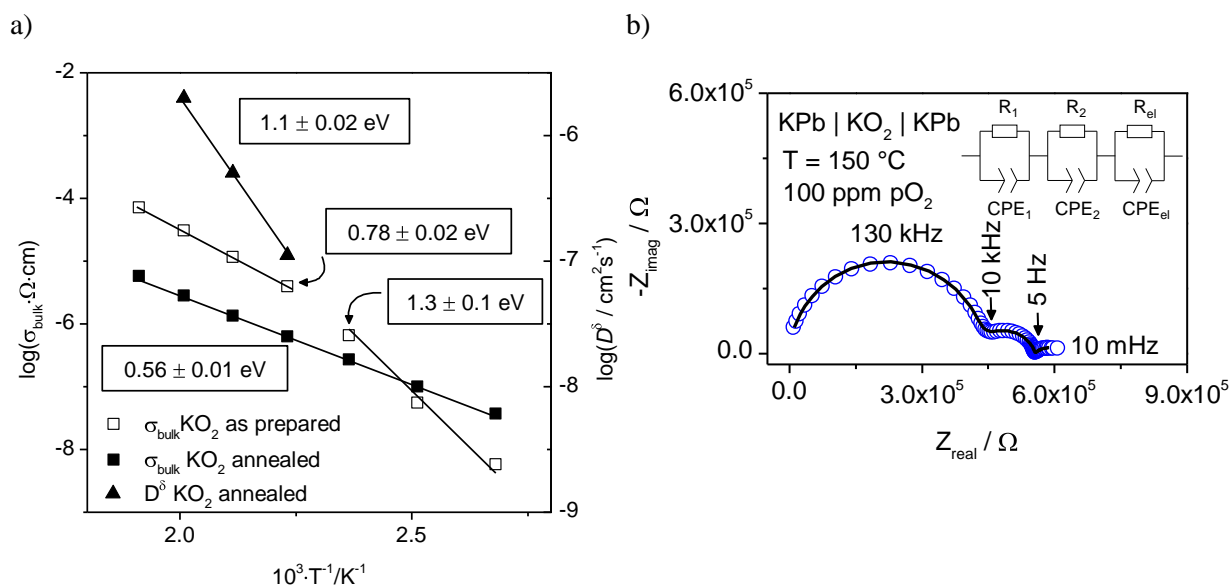


Figure 3.36: a) Temperature dependence of the total bulk conductivity of as prepared (open squares) and 450 °C annealed (solid squares) KO_2 at 1 bar $p\text{O}_2$ and chemical diffusivity of 450 °C annealed KO_2 (solid triangle) at 1000 ppm $p\text{O}_2$ and b) impedance spectrum of the cell $\text{KPb} | \text{KO}_2 | \text{KPb}$ at 150 °C and 100 ppm $p\text{O}_2$.

The cell $\text{KPb} | \text{KO}_2$ (as prepared) | KPb exhibits a significantly lower electrode contribution (Figure 3.36b). As in the case of K_2O_2 , the electrodes are not entirely reversible and some electrode polarization remains in the impedance spectrum at low frequencies. Moreover, another contribution appears at mid frequencies with a capacitance between typical values of bulk and electrode ($C = 10^{-9}$ F). Since the grain boundaries in KO_2 seem to be permeable for the main charge carriers (cf. Figure 3.30), an additional mid frequency contribution was observed only in one out of ten cells $\text{Au} | \text{KO}_2 | \text{Au}$, but in five out of five cells $\text{KPb} | \text{KO}_2 | \text{KPb}$, this additional relaxation process is more likely related to a blocking layer formed by the reaction of KO_2 with KPb . But then the electrode polarization can not only be caused by polarization of oxygen species at the KPb electrode, but also by blocking of electrons at this reaction layer if it has a higher electronic resistance than the KO_2 layer. In view of this, it cannot be reliably determined from the remaining electrode contribution in the impedance spectrum of $\text{KPb} | \text{KO}_2 | \text{KPb}$ that oxygen species are significantly contributing to the ionic conductivity.

3.5 Rubidium and Cesium Superoxide

3.5.1 Chemical Characterization, Thermodynamic Stability and Crystallographic Structure

The superoxide stretch vibration gives rise to strong Raman peaks in rubidium and cesium superoxide (1148 cm^{-1} for RbO_2 , 1135 cm^{-1} for CsO_2). As prepared powders of RbO_2 and CsO_2 are typically contaminated with small amounts of carbonate and other minor impurities (probably hydroxide in RbO_2 and peroxide in CsO_2) according to the Raman spectra (Figure 3.37). It is interesting to note that the black-brown intermediate product that is formed by oxidation of rubidium metal at room temperature and 1 bar $p\text{O}_2$ shows a Raman peak at 753 cm^{-1} , which is in the range of the peroxide stretch vibrations, but does not exactly match its frequency in pure, bulk Rb_2O_2 at 782 cm^{-1} .^[91] According to its XRD pattern, the powder is a mixture of the suboxide Rb_4O_6 and the peroxide Rb_2O_2 .

The carbonate and (presumably) hydroxide impurities are below the XRD detection limit in RbO_2 . CsO_2 is difficult to probe in transmission geometry with capillaries as the x-rays can barely penetrate the sample, because of the high atomic mass of Cs and thus high number of scattering electrons. Only upon diluting CsO_2 with glass powder by 1:5 it was possible to observe its reflections on a very noisy background (Figure 3.38). In principle, it would be more suitable to measure CsO_2 powder in reflection geometry to obtain strong peaks which enable one to identify possible impurities and to refine the lattice constants, but the available sample holder sealing the sample with Kapton (a polyimide film) is not sufficiently gas tight for these extremely air sensitive samples.

The thermodynamic stability of CsO_2 versus Cs_2O_2 according to ref.^[125] is depicted in Figure 3.39. No thermochemical data has been found for the corresponding rubidium compounds.

Both RbO_2 and CsO_2 crystallize in the tetragonal CaC_2 -type structure at room temperature, which transforms into the cubic NaCl -type structure at elevated temperatures. The transition temperatures at which both phases co-exist are reported as $130 - 150\text{ }^\circ\text{C}$ for RbO_2 and $130 - 200\text{ }^\circ\text{C}$ for CsO_2 . The unit cells of tetragonal and cubic CsO_2 are shown in Figure 3.40. The superoxide ions exhibit rotational disorder in the high temperature cubic phase.

The only detectable cation impurities in RbO_2 and CsO_2 are isovalent alkali metals (600 ppm Na, 100 ppm K and 15 ppm Li for RbO_2 ; 700 ppm Na, 20 ppm K and 5 ppm Li for CsO_2). In both materials alkaline earth metals are below the detection limit of ICP-OES (i.e., $c_{\text{Mg}} + c_{\text{Ca}} + c_{\text{Sr}} + c_{\text{Ba}} < 20\text{ ppm}$).

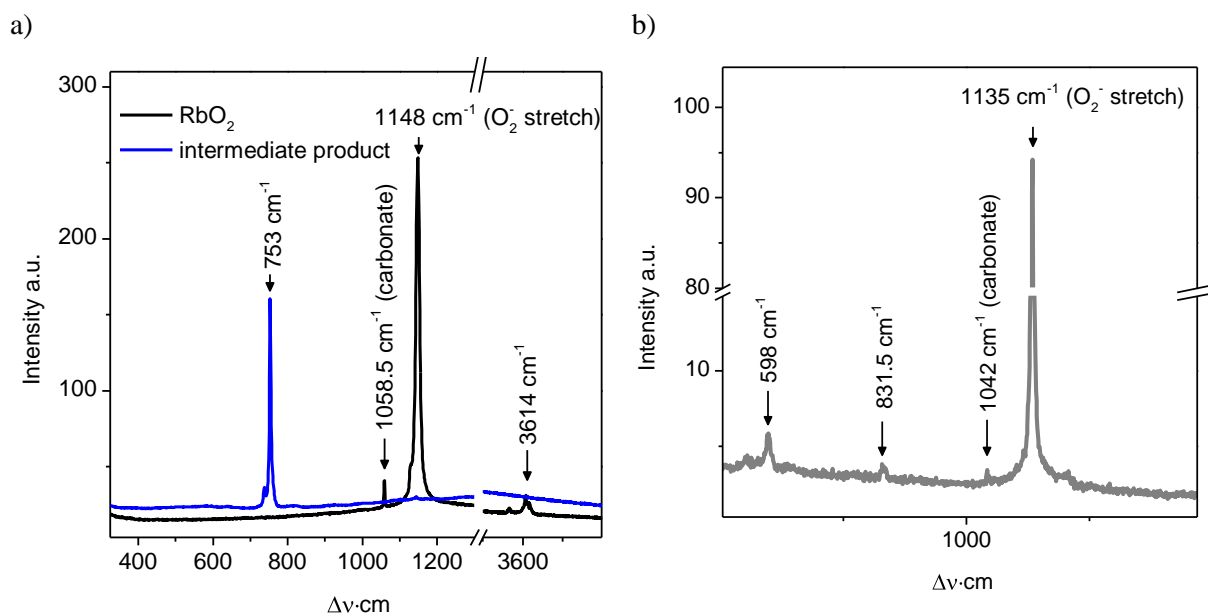


Figure 3.37: Raman spectrum of a) RbO₂ (black) and intermediate reaction product of metal Rb and O₂ at room temperature (blue) and b) CsO₂

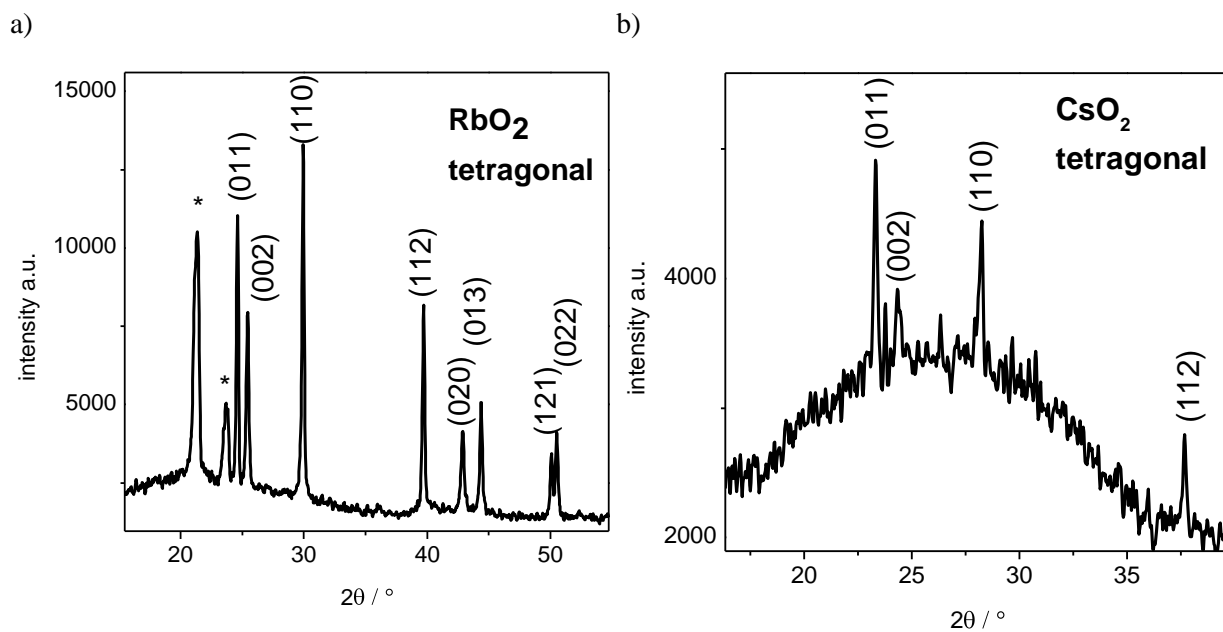


Figure 3.38: X-ray diffraction pattern of a) RbO₂ (reflections denoted with asterisk are from the sample holder puddy to fix the capillary) and b) CsO₂ (diluted with glass powder) indexed according to the data provided in the Inorganic Crystal Structure Database (ICSD) collection codes 647338 and 627060.

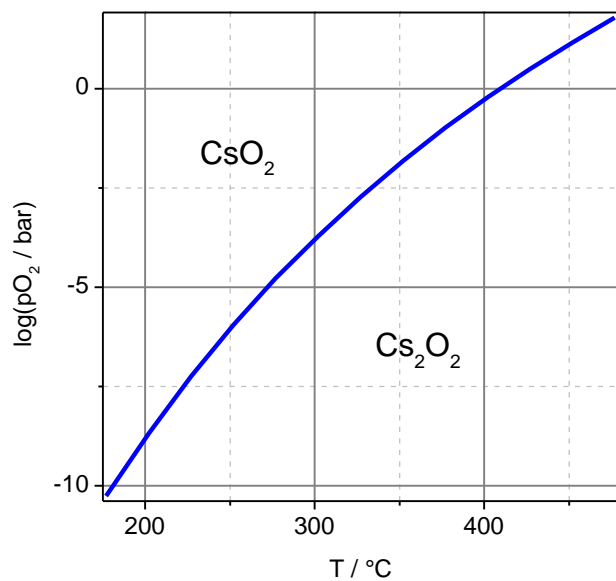


Figure 3.39: Thermodynamic stability of CsO_2 vs. Cs_2O_2 calculated according to thermochemical data published in ref.^[125].

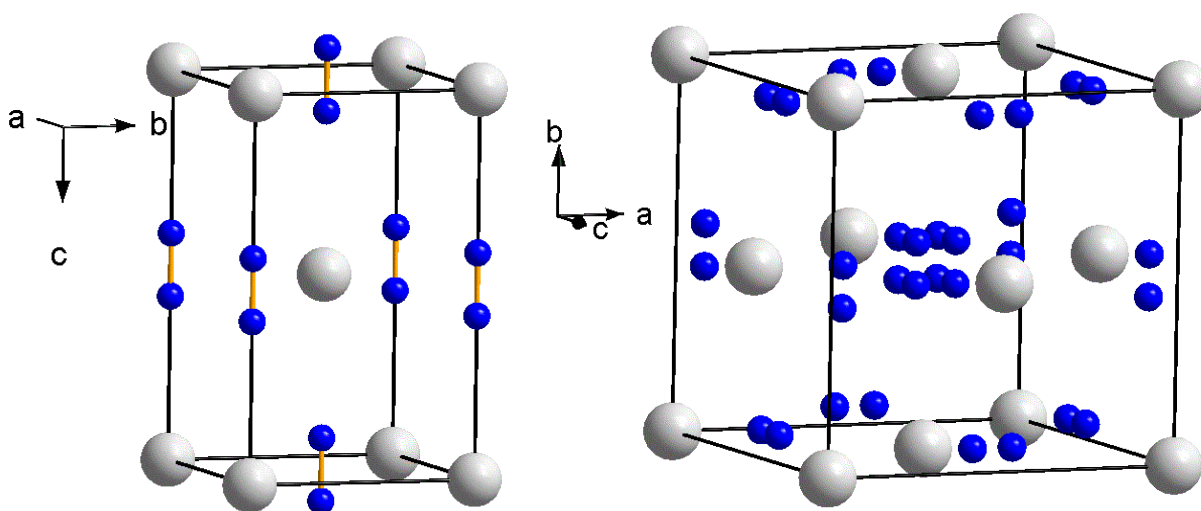


Figure 3.40: Unit cells of CsO_2 with a) tetragonal (space group $I 4/mmm$) and b) cubic ($Fm-3m$) modification. The oxygen cluster on the superoxide site is meant to indicate the rotational disorder of the superoxide ions in the cubic phase.

3.5.2 Electrochemical Characterization

The geometric density of uniaxially cold pressed pellets of RbO_2 and CsO_2 is $> 95\%$ of the theoretical density, i.e. the grains are heavily plastically deformed already at room temperature and 250 MPa uniaxial pressure. The impedance spectra of the cells $\text{Au} | \text{MO}_2 | \text{Au}$ ($\text{M} = \text{Rb}, \text{Cs}$) as shown in Figure 3.41 are characterized by a high frequency bulk response ($\epsilon_{\text{RbO}_2} \approx 15$ and $\epsilon_{\text{CsO}_2} \approx 13$) and a low frequency electrode polarization. At 250 °C a further relaxation process at mid frequencies with a capacitance $10^{-8} - 10^{-10}$ F is observed after some time. The capacitance is between the electrode and bulk contribution, which could point to blocking grain boundaries or more likely - since the phenomena developed at high temperatures after considerable time- to a reaction of the superoxide phases with the gold electrodes. Although gold is thermodynamically stable against oxidation by molecular oxygen at ambient pressure even at high temperatures, it has been shown to react with alkali peroxides and superoxides to ternary oxides at elevated temperatures^[126] and thin films of gold are known to oxidize to Au_2O_3 upon contact with highly reactive oxidizing agents even at low temperatures^{[127],[128]}.

The ionic conductivity was separated from the apparent electronic conductivity by dc polarization and electrochemical impedance measurements on the cells $\text{Au} | \text{MO}_2 | \text{Au}$ with $\text{M} = \text{Rb}, \text{Cs}$ (Figure 3.42). Both electronic and ionic conductivity depend significantly upon the oxygen partial pressure (see Figure 3.43). Based on the negative slope of the ionic conductivity in the $\log\sigma$ vs. $\log p_{\text{O}_2}$ plot, alkali vacancies with a p_{O_2} dependence of $[V'_M] \sim p_{\text{O}_2}^{\frac{1}{2}}$ in the intrinsic case (compensated by electronic defects) and with a p_{O_2} independence in the extrinsic case (controlled by donor impurities) can be immediately discounted as main ionic charge carrier.

The only electroneutrality conditions (disregarding electronic compensation by holes, which is unlikely to prevail due to the already highly oxidized state of the superoxide) yielding a negative p_{O_2} dependence of both electronic and ionic conductivities are the compensation of superoxide vacancies or alkali interstitials by electrons (cf. Table 3.8). Hence, the increasing ionic conductivity with decreasing p_{O_2} can be explained either by the transport of alkali metal ion interstitials ($[M_i^\bullet] \sim p_{\text{O}_2}^{\frac{1}{2}}$), superoxide vacancies ($V_{\text{O}_2}^\bullet \sim p_{\text{O}_2}^{-\frac{1}{2}}$) or oxide defects occupying superoxide sites ($O'_{\text{O}_2} \sim p_{\text{O}_2}^{-1}$).

The change of the ionic conductivity upon introducing donor dopants (excess positive charge) would allow distinguishing between negatively charge oxide defects and positively charged superoxide vacancies and alkali interstitials. But as efforts to introduce donors in KO_2 were already not successful (i.e. no significant change in the conductivity was found) despite the relatively small radius mismatch between potassium and barium ions of 2%, donor doping experiments were not conducted with RbO_2

and CsO_2 in course of this thesis. The crystal radii of Rb^+ and Cs^+ are the largest among single atomic cations (not taking into account the radioactive francium). The barium ion is the largest cation with a suitable valence > 1 to act as donor dopant, but the radius mismatch is already 10 % for Rb^+ and 17% for Cs^+ .^[107]

It is noteworthy that Cs-Pb reacts with CsO_2 already at room temperature upon uniaxial pressing as the color of the latter changed from orange to brown. Since also the K-Pb compound seemed to have reacted with KO_2 at measurement conditions, the preparation of Rb-Pb and its use as rubidium reversible electrode for RbO_2 did not seem promising and was not attempted.

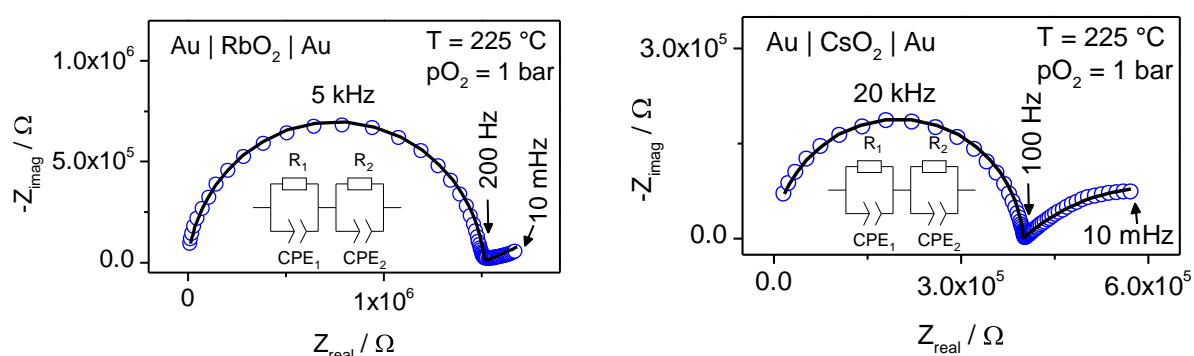


Figure 3.41: Impedance spectrum of the cell a) $\text{Au} | \text{RbO}_2 | \text{Au}$ and b) $\text{Au} | \text{CsO}_2 | \text{Au}$ at $225\text{ }^\circ\text{C}$ and $1\text{ bar } p\text{O}_2$ with equivalent circuit and fit. The fit parameters of the bulk contributions are $R_1 = 1.5 \cdot 10^6\ \Omega$, $Q_1 = 3.6 \cdot 10^{-12}$, $n_1 = 0.952$ for RbO_2 and $R_1 = 3.98 \cdot 10^5\ \Omega$, $Q_1 = 3.64 \cdot 10^{-12}$, $n_1 = 0.975$ for CsO_2 .

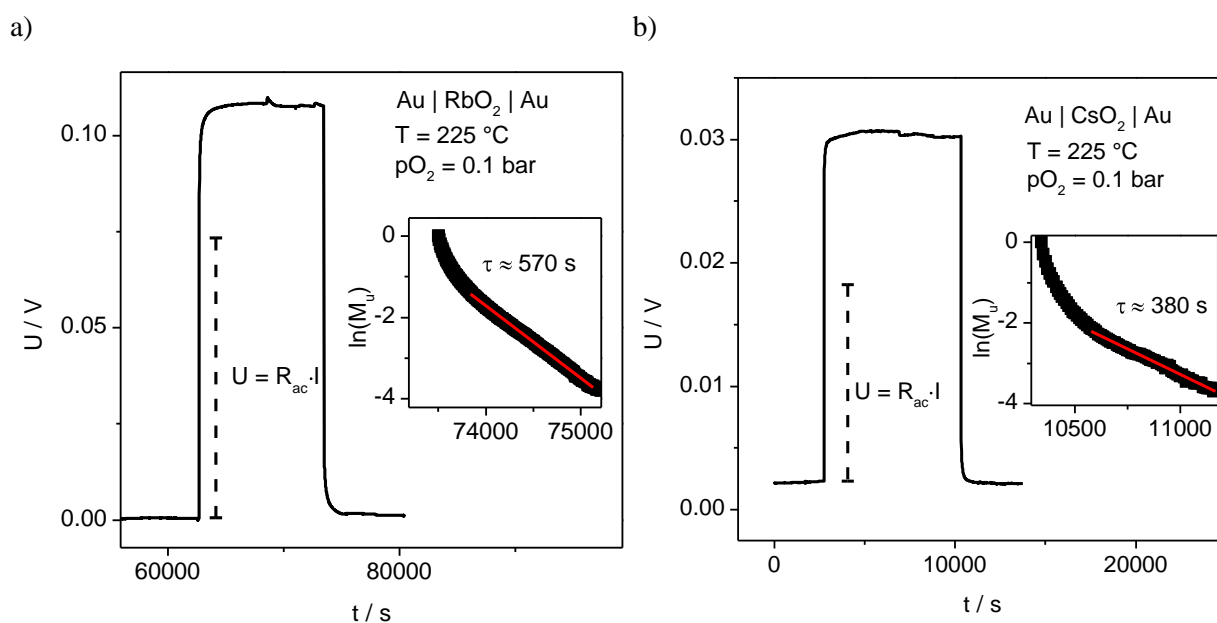


Figure 3.42: Dc stoichiometry polarization of the cell a) $\text{Au} | \text{RbO}_2 | \text{Au}$ and b) $\text{Au} | \text{CsO}_2 | \text{Au}$ at $225\text{ }^\circ\text{C}$ and $0.1\text{ bar } p\text{O}_2$ ($I = 50 \cdot 10^{-9}\text{ A}$). The insets show the linear fit of the $\log M_u$ (M_u : normalized voltage) vs. time for long depolarization times. These dc polarization curves are not representative for the entire $p\text{O}_2$ range. At $p\text{O}_2 = 1\text{ bar}$, a true stationary state is usually not observed, but instead a slow drift towards higher polarization voltages.

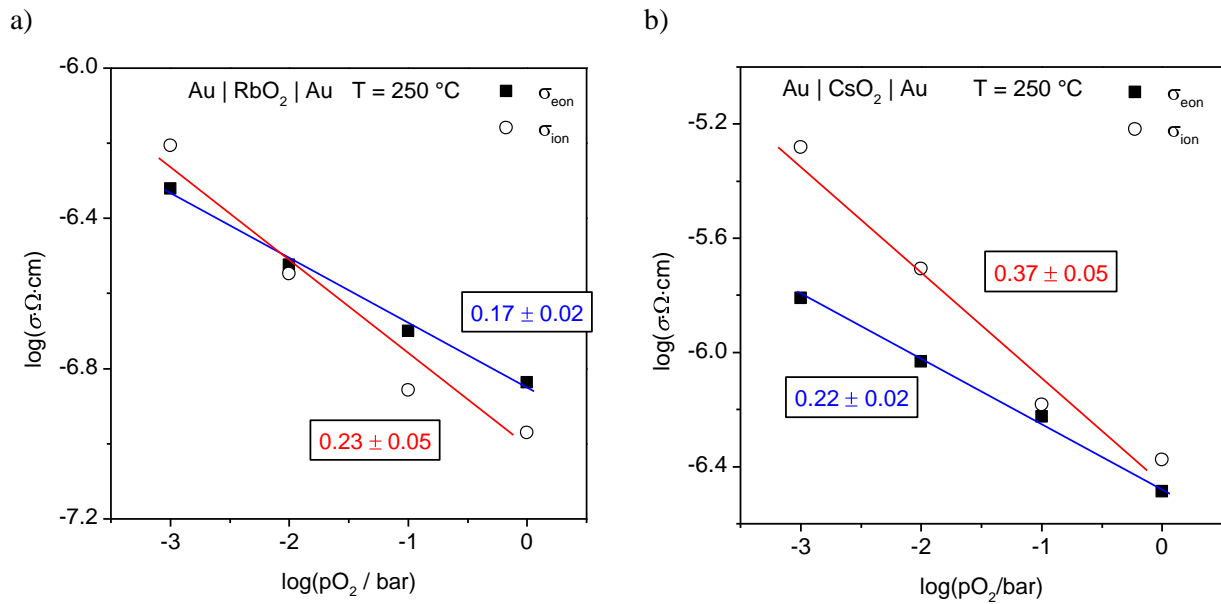


Figure 3.43: pO_2 dependence of the electronic and ionic conductivity of uniaxially pressed a) RbO_2 and b) CsO_2 at 250 °C . For reasons of thermodynamic stability, the samples were not subjected to $pO_2 < 1000\text{ ppm}$.

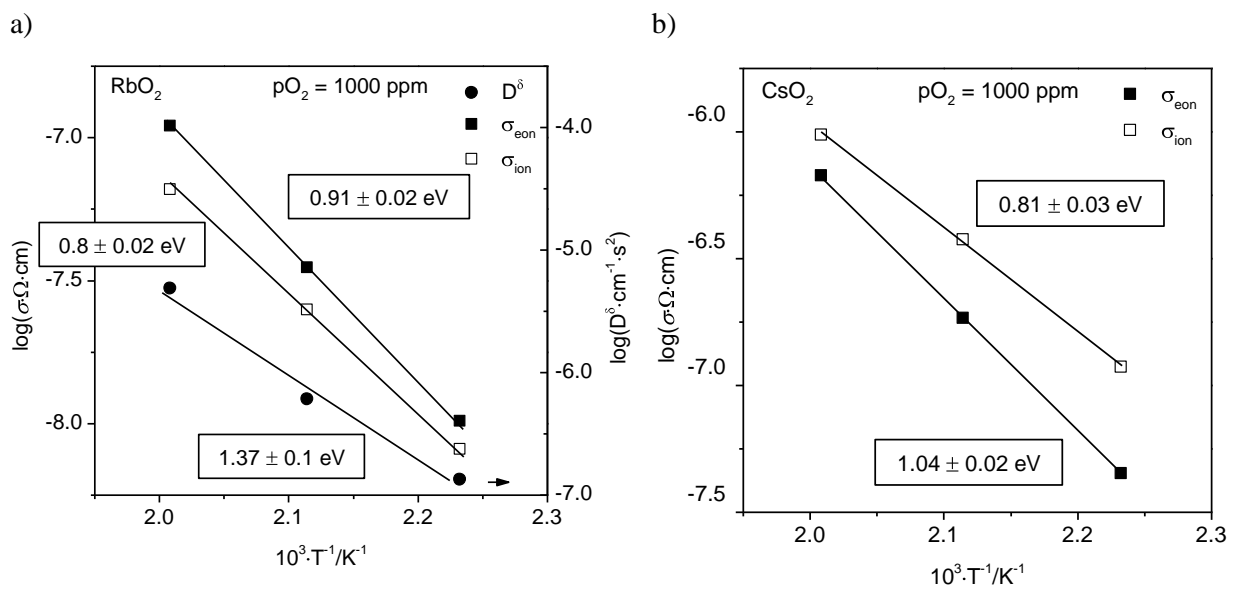


Figure 3.44: Temperature dependence of the electronic and ionic conductivity of uniaxially pressed a) RbO_2 and b) CsO_2 at $1000\text{ ppm } pO_2$. In b) also the temperature dependence of the chemical diffusion coefficient of RbO_2 is plotted (right y-axis).

3.6 Electromotive Force Measurements of Alkali Superoxides

The electromotive force measurement (EMF) is another electrochemical method to separate ionic and electronic conductivity. The transference number of the ionic species is obtained from the EMF loss relative to the Nernst potential (calculated according to equation (12)) and related to the total bulk conductivity obtained from electrochemical impedance spectroscopy:

$$\sigma_{ion} = t_{ion} \cdot \sigma_{bulk} \quad (36)$$

$$\sigma_{eon} = (1 - t_{ion}) \cdot \sigma_{bulk} \quad (37)$$

Ideally, the ratio between ionic and electronic conductivity is not larger than 1 – 2 orders of magnitude (depending on the measurement conditions and background noise), otherwise only an upper limit of the lower conductivity can be provided. For the case that the EMF is generated by a difference in the oxygen partial pressure on each side of an oxide based material, the method is typically limited to high temperatures with sufficiently fast oxygen exchange kinetics.^[90] However, for potassium and cesium superoxide it was found that EMF measurements are possible even at low temperatures < 200 °C with platinum electrodes. It should be noted that fresh EMF cells of the superoxides need to be annealed at 225 -250 °C before a baseline close to 0 mV for the symmetric cell with $pO_2(1) = pO_2(2)$ and a stable and fast EMF response for $pO_2(1) \neq pO_2(2)$ is observed. This conditioning is likely related to the activation of the electrodes, i.e. creating sufficient triple phase boundary.

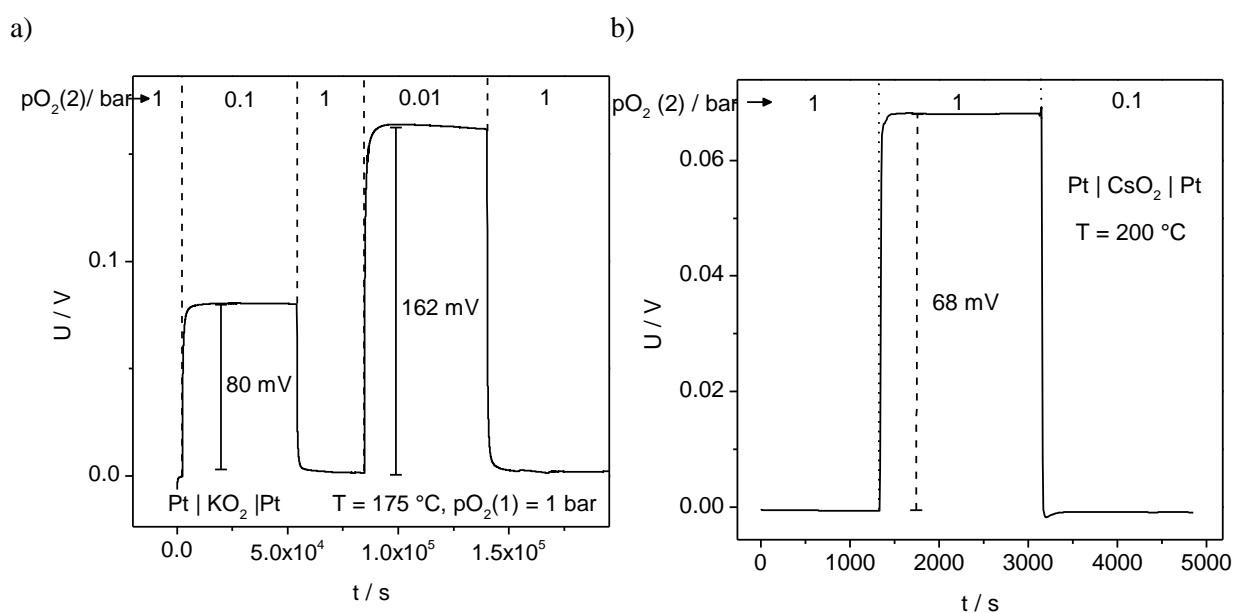


Figure 3.45: EMF measurement of $pO_2(1) | Pt | MO_2 | Pt pO_2(2)$ with $pO_2(1) = 1 \text{ bar}$ of a) as prepared KO_2 at $175 \text{ }^\circ\text{C}$ and b) as prepared CsO_2 at $200 \text{ }^\circ\text{C}$.

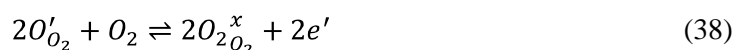
EMF measurements of the cell $\text{pO}_2(1) \mid \text{Pt} \mid \text{KO}_2 \mid \text{Pt} \mid \text{pO}_2(2)$ with as prepared KO_2 are shown in Figure 3.45a. The EMF values in the temperature range 150 to 225 °C correspond to about 90 % of the value calculated from the Nernst equation with $z = 1$ (compare with Table 3.9). If the EMF losses can be attributed to electronic current, the ionic transference number of as prepared KO_2 amounts to $t_{\text{ion}}(\text{EMF}, 1 \text{ bar} - 0.01 \text{ bar pO}_2) = 0.9$. The result would well correspond to the dc conductivity measurement with $t_{\text{ion}}(\text{dc conductivity}, 1 \text{ bar pO}_2) = 0.93$ and $t_{\text{ion}}(\text{dc conductivity}, 1000 \text{ ppm pO}_2) = 0.87$.

For annealed KO_2 , the ionic and apparent electronic conductivity are of the same magnitude according to dc polarization and ac impedance spectroscopy measurements, which would result in an ionic transference number of around 1/2. However, the EMF of the cell $\text{pO}_2(1) \mid \text{Pt} \mid \text{KO}_2 \mid \text{Pt} \mid \text{pO}_2(2)$ with annealed KO_2 is again close to the Nernst potential suggesting an ionic transference number > 0.9 with only minor electronic conductivity. Likewise, a significant deviation is found for the transference number of CsO_2 as measured by the EMF method with platinum electrodes ($t_{\text{ion}}(\text{EMF}, 1 - 0.1 \text{ bar pO}_2) \geq 0.7$, Figure 3.45b) and by dc polarization technique with gold electrodes ($t_{\text{ion}}(\text{dc conductivity}, 1 \text{ bar pO}_2) \approx 0.5$).

Table 3.9: Difference in the reversible cell voltage according to the Nernst equation with $z = 1$ (i.e. one electron transferred as in alkali superoxides) upon changing the pO_2 by one order of magnitude for various temperatures.

T / °C	175	200	225
$\Delta E / \text{mV}$	88.9	93.9	98.8

EMF losses may not only occur because of electronic current, but also by currentless counterdiffusion of ionic species^[84]. But such phenomena cannot explain why the measured EMF is actually higher than expected from the ac and dc conductivity measurements. The equilibration of oxide defects with the gas phase according to equation (38) would generate an EMF with the opposite sign than the EMF related to the equilibration of superoxide with the gas phase and it would therefore also decrease the potential difference at the electrodes.



On the other side, it is in principle conceivable that the electrodes of the nominally ionic blocking cell $\text{Au} \mid \text{MO}_2 \mid \text{Au}$ (with $M = \text{K}, \text{Rb}, \text{Cs}$) are actually permeable for oxygen species under the measurement conditions. In this case, the apparent electronic conductivity obtained from the stationary state of the dc stoichiometry polarization corresponds to the transport of superoxide (or oxide) defects. This requires sufficient porosity and triple phase boundary for a significant flux of oxygen from the MO_2/Au interface to the gas phase. It was not possible so far to characterize the porosity of the gold electrode on MO_2 by scanning electron microscopy due to their high reactivity

when exposed to air, but only of gold films sputtered under the same conditions on a glass substrate (cf. Figure 2.2). These films show no porosity above the resolution limit of the SEM (≈ 20 nm). The same is observed for a gold film annealed for 12 hours at 225 °C and when the glass substrate is roughened with sandpaper to create a similar thermal load and roughness of the surface of MO_2 samples.

However, it is possible that an originally dense gold film on MO_2 is shattered and fissured at elevated temperatures because of a crystallographic phase transition (reported at 60–150 °C for KO_2 ^[124], 130 - 150 °C for RbO_2 and 130 – 200 °C for CsO_2 ^[129]) or because of reactivity of the superoxides with the electrode (e.g. reaction to ternary oxides^[126]). This is supported by the observation that freshly prepared EMF cells $\text{pO}_2(1) | \text{Pt} | \text{MO}_2 | \text{Pt} | \text{pO}_2(2)$ ($M = \text{K}, \text{Cs}$) show only poor response and performance upon changing the $\text{pO}_2(2)$ before they are exposed to at least 225 °C. Therefore, the electronic conductivity as extracted from EMF measurements is regarded as more reliable than the values obtained from dc polarization technique. The difference is likely due to oxygen species exchanged with the gas phase at the gold electrodes.

In view of this, the dependence of the electronic conductivity on pO_2 was studied by EMF measurements of the cell $\text{pO}_2(1) | \text{Pt} | \text{CsO}_2 | \text{Pt} | \text{pO}_2(2)$ at 200 °C and $\text{pO}_2(2) = 1/2 \cdot \text{pO}_2(1)$ (e.g. 1 bar vs. 0.5 bar). The total bulk conductivity of the sample pellet under these conditions was approximated by the total bulk conductivity when the whole pellet is exposed to $\text{pO}_2(1)$ (since the total bulk conductivity is increasing with decreasing pO_2 , this leads to an underestimation of the electronic conductivity by up to 10%). Figure 3.46a compares the electronic conductivity obtained from the EMF method with the electronic conductivity obtained from dc polarization technique on the same sample with the same electrodes. At high pO_2 , the dc polarization technique yields an apparent electronic conductivity which is about half an order of magnitude higher than the value from the EMF measurements. The difference in σ_{eon} from both methods seems to decrease with decreasing pO_2 , as it is expected for leakage currents involving oxygen exchange with the gas phase, since the oxygen surface exchange rate decreases with decreasing pO_2 . At 1000 ppm, the electronic conductivities obtained from both methods are comparable. Accordingly, the apparent electronic conductivities reported for $\text{Au} | \text{MO}_2 | \text{Au}$ ($M = \text{K}, \text{Cs}$ and probably also Rb) in the previous section are only reliable for low pO_2 , but may include contributions from transport of oxygen species at high pO_2 .

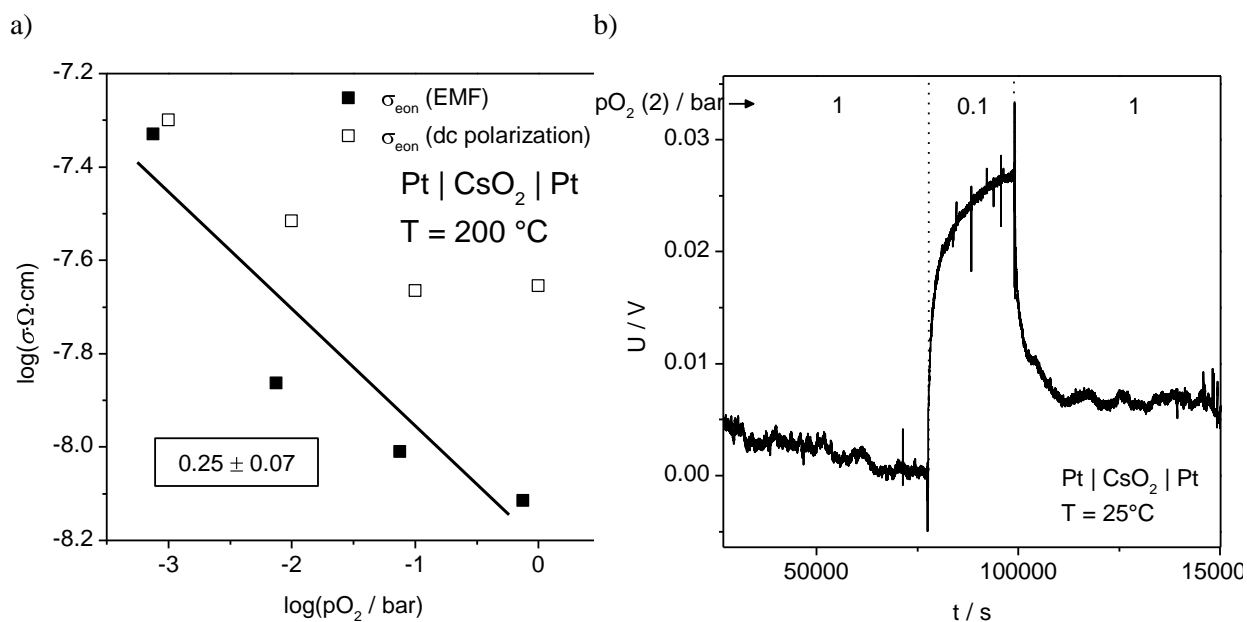


Figure 3.46: a) Oxygen partial pressure dependence of the electronic conductivity of CsO₂ according to EMF measurements (solid squares) and dc polarization technique (open squares) on the same cell Pt | CsO₂ | Pt at 200 °C (the cell was previously annealed for 1 h at 225 °C to improve the EMF response) and b) EMF measurement of the cell pO₂(1) | Pt | CsO₂ | Pt | pO₂(2) with pO₂(1) = 1 bar at 25 °C.

It is interesting to note that the cell pO₂(1) Pt | CsO₂ | Pt | pO₂(2) responds to a pO₂(2) change even at room temperature, but the relaxation is very slow, noisy and extremely sensitive to disturbances (e.g. already approaching the measurement setup by 1 m causes spikes in the curve). The poor performance at low temperatures is inevitably caused already by the high ionic resistance $\geq 1 \text{ G}\Omega$ of the CsO₂ pellet. Figure 3.47 demonstrates that a reasonable EMF can be measured at a temperature as low as 75 °C (after it was conditioned at 225 °C for 12 h). The kinetics of the relaxation upon switching pO₂ (2) from 1 bar to 0.1 bar is still slow at this temperature with $\tau = 700 \text{ s}$ (time to reach 70% of the final voltage), but decreases to $\tau = 20 \text{ s}$ already at 125 °C. In terms of performance, the cell Pt | CsO₂ | Pt cannot compete as a low temperature oxygen gas sensor with potentiometric and amperometric oxygen sensors based on halide containing fast ionic conductors that provide reasonable sensor signals and response even at ambient temperature.^{[130],[131]}

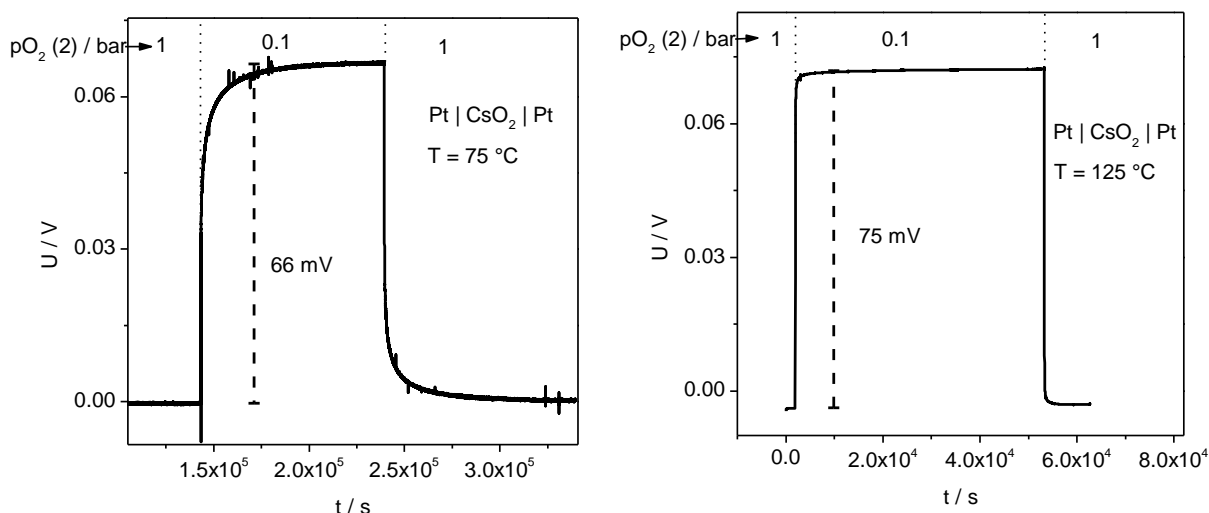


Figure 3.47: EMF measurement of the cell $\text{pO}_2(1) | \text{Pt} | \text{CsO}_2 | \text{Pt} | \text{pO}_2(2)$ with $\text{pO}_2(1) = 1$ bar at 75°C and 125°C .

EMF cells were also prepared with gold instead of platinum electrodes. The cell $\text{pO}_2(1) \text{Au} | \text{CsO}_2 | \text{Au} | \text{pO}_2(2)$ shows a voltage relaxation that is about one order of magnitude slower than of the cell with platinum electrodes when switching $\text{pO}_2(2)$ from 1 bar to 0.1 bar at 225°C . This is likely because of a lower catalytic activity of gold for the oxygen exchange reaction, but may be also due to a different morphology and nature of the triple phase boundary between CsO_2 , electrode and gas phase.

3.7 Oxygen Isotope Exchange

To gain further insight into the mechanism of oxygen exchange in alkali peroxides and superoxides, oxygen isotope exchange measurements with analysis of the gas phase isotope ratio were performed. These experiments reveal if oxygen exchange is limited to the surface layer or actually penetrates into the bulk and further, and whether or not the oxygen exchange involves breaking of the O-O bond. In contrast to a chemical relaxation experiment with the chemical surface reaction rate constant k^δ and the chemical diffusivity D^δ (e.g. conductivity relaxation upon changing pO_2), which may proceed by ambipolar transport of electronic charge carriers and either cations or anions, the tracer relaxation experiment with the tracer surface reaction rate constant k^* and the tracer diffusivity D^* requires specifically the transport of the species whose isotope composition is changed, i.e. diffusion of superoxides/peroxides via vacancies or interstitials upon changing the gas phase from $^{16}\text{O}_2$ to $^{18}\text{O}_2$.

Sample powders of Na_2O_2 (with about 500 nm particle size) and Li_2O_2 (with 200 nm to 1 μm particle size) were exposed to 1% $^{18}\text{O}_2$ in N_2 for several hours. Then the capillaries were purged with 1% $^{16}\text{O}_2$ and the exhaust gas was analyzed for $^{18}\text{O}_2$ and $^{16}\text{O}-^{18}\text{O}$ by mass spectrometry. For Li_2O_2 , the amount of exchanged oxygen turned out to be below the detection limit of the mass spectrometer with the standard size capillary described in the experimental section, therefore the bulge in the capillary for taking up the sample powder was significantly increased to 25 mm thickness and 40 mm length. The modified capillary could take up about 8.8 g of Li_2O_2 powder (for comparison, only 0.3 g of Na_2O_2 was needed). The volume behind the glass frit was filled with glass wool to reduce the free gas volume in the capillary. The flushing time from 1% $^{18}\text{O}_2$ to its baseline level was about 1 hour for this larger capillary, but which is still fast compared to the oxygen exchange of the sample powder.

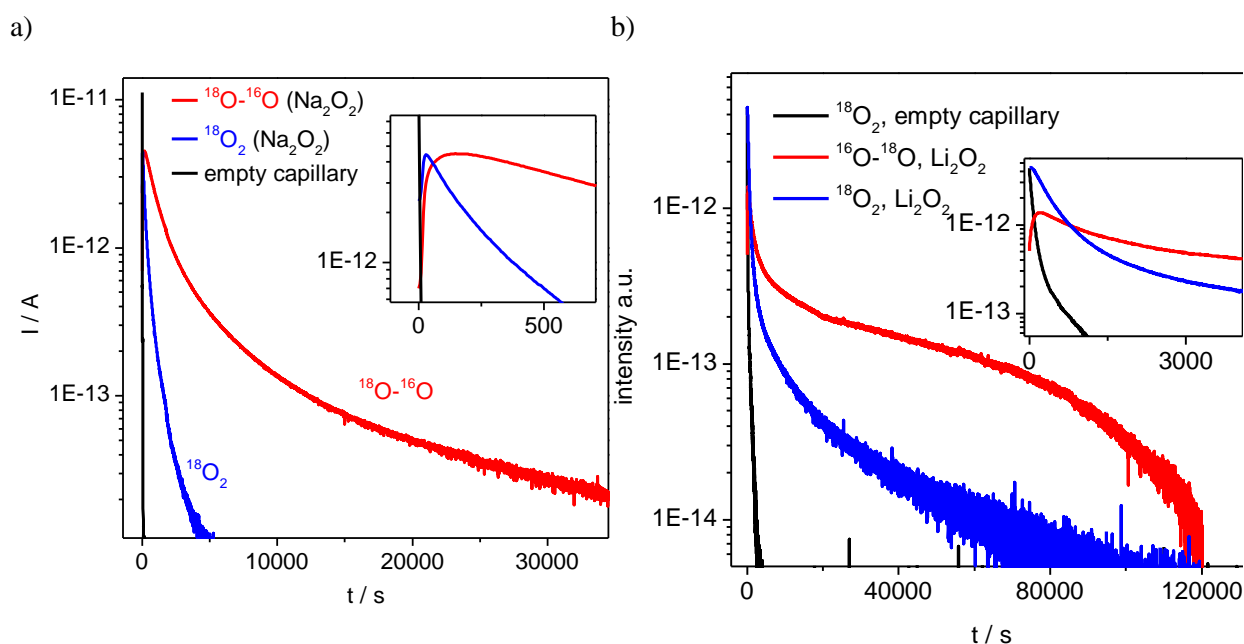


Figure 3.48: $^{18}\text{O}_2$ (blue) and $^{18}\text{O}-^{16}\text{O}$ (red) mass spectrometry signals of a) Na_2O_2 and b) Li_2O_2 in 3 ml/min 1% $^{16}\text{O}_2/\text{N}_2$ at 200 °C after exposing the sample powders to 1% $^{18}\text{O}_2$ for several hours. Also shown is the relaxation of the $^{18}\text{O}_2$ signal for the empty capillary.

Figure 3.48a/b show the $^{18}\text{O}_2$ and $^{18}\text{O}-^{16}\text{O}$ relaxation curves of Na_2O_2 and Li_2O_2 in 3 ml/min 1% $^{16}\text{O}_2/\text{N}_2$ at 200 °C. In the case that oxygen incorporation into peroxides proceeds preferable without breaking up the molecular unit, mainly $^{18}\text{O}_2$ species are expected to be detected in the exhaust gas after passing the sample. But interestingly, it is the mixed species $^{16}\text{O}-^{18}\text{O}$ that is predominantly obtained from Na_2O_2 and Li_2O_2 . Clearly, the O-O bond is broken during some step of the oxygen exchange in these peroxides. The ratio of 18-oxygen released as $^{16}\text{O}-^{18}\text{O}$ and as $^{18}\text{O}_2$ from the sample powder is 5:1 for Na_2O_2 and 3:2 for Li_2O_2 according to the integrated intensities of the mass spectrometry signals and taking into account that the mixed species consists only to 50% of 18-oxygen.

The amount of oxygen exchanged with the sample can be calculated by relating the ion current of the $^{16}\text{O}_2$ signal as generated by 1% O_2/N_2 to the integrated intensity of the $^{18}\text{O}_2$ and $^{18}\text{O}-^{16}\text{O}$ signals. The total number of O_2^{2-} in the sample is given by $N = \frac{N_A \cdot m}{M}$ (N_A : Avogadro constant, m : sample mass, M : molar mass). According to this, only about 10^{-3} and $5 \cdot 10^{-5}$ of the peroxide ions in Na_2O_2 and Li_2O_2 respectively were exchanged during the measurement. For Li_2O_2 , this corresponds to less than the amount of peroxide ions contained in the elementary cells, which are located just at the surface of the particles (the ratio of surface to bulk elementary cells is about $10^{-4} - 10^{-3}$ for 1 to $0.1 \mu\text{m}$ spherical particles).

The relation $L_c = \frac{D^*}{k^*}$ defines the critical length for ceramic materials above/below which the oxygen exchange is limited by diffusion/surface reaction^[132] (the relation is a consequence of the linear and quadratic dependence of the equilibration time on the particle size for surface reaction and for bulk diffusion, respectively). The values of L_c vary from 10 nm (e.g. for ZnO_2 at 1038°C) to several cm (e.g. for Europium doped Bi_2O_3 at 500°C).^[133] For alkali peroxides, the critical length is not known so far. However, it is reasonable to assume that L_c of Li_2O_2 and Na_2O_2 is rather low because the diffusion of the bulky O_2^{2-} in the environment of cations with low polarizabilities can be expected to be relatively sluggish and/or because the surface reaction is fast since breaking of the molecular oxygen bond is not necessarily required, at least for exchange with the first layer of the material.

This is supported by the fact that the measured relaxation curves deviate from a simple exponential decay as expected for surface reaction limitation (cf. simulated curve in Figure 3.49) and are strongly bent in the logarithmic representation. In contrast to this, an exponential relaxation of the outgoing flux is expected only for long times in the case of diffusion limitation. Moreover, the sample powder was only partially loaded with 18-oxygen (because of long equilibration times and high cost of $^{18}\text{O}_2$ gas), which has two effects on the 18-oxygen flux from sample powder. First of all, a maximum in the 18-oxygen profile is established within the sample particles with 18-oxygen gradients both to the surface as well as further into the sample upon changing to 16-oxygen (Figure 3.50a). Only when the gradient towards the interior of the sample is leveled out, the 18-oxygen flux from the sample to the atmosphere decays exponentially. The exponential relaxation is thus shifted to longer waiting times. Secondly, the magnitude of the outgoing 18-oxygen flux is decreased. Both result in a decrease of the 18-oxygen flux when the exponential relaxation at long times is reached. But if the flux is then already below the baseline of 18-oxygen species in the 16-oxygen gas stream as detected by the mass spectrometer, the exponential decay is not observed because of this technical limitation (as illustrated by the lower limit of the y-axis in Figure 3.50b).

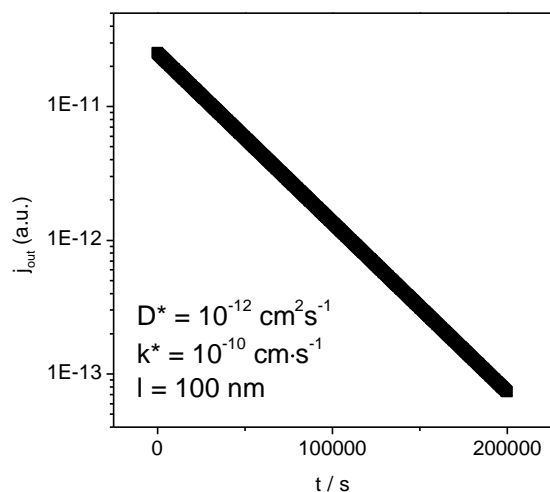


Figure 3.49: Simulated 18-Oxygen flux from a spherical particle with a radius of 100 nm (exposed to an 18-oxygen atmosphere for 1000 s before switching to 16-oxygen atmosphere) for surface reaction limitation according to finite difference method. The matlab code was originally written by Roger de Souza and strongly modified by Rotraut Merkle.

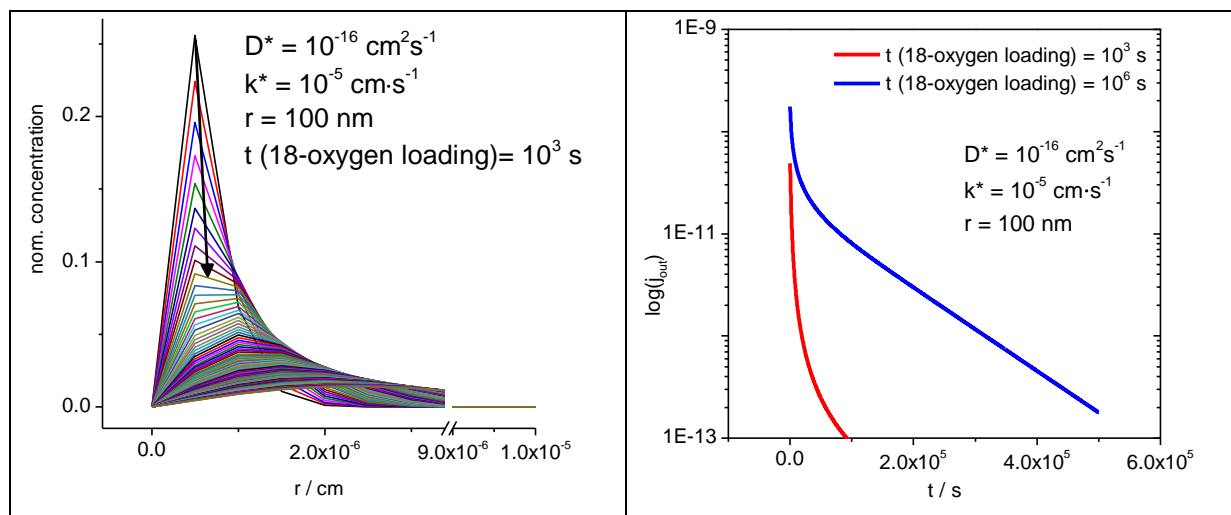


Figure 3.50: a) Simulated 18-oxygen profile in partially 18-oxygen loaded spherical particle after switching from 18-oxygen to 16-oxygen gas atmosphere (diffusion limitation) and b) simulated 18-oxygen flux from a spherical particle after switching from 18-oxygen to 16-oxygen gas atmosphere for partially (red) and almost full exchange (blue) of the particle with 18-oxygen (diffusion limitation). D^* , k^* and the lower limit of the y-axis have been arbitrarily chosen to illustrate the situation.

The oxygen exchange is significantly enhanced in the heavy alkali superoxides KO_2 , RbO_2 , CsO_2 compared to the light peroxides Na_2O_2 and Li_2O_2 as already evidenced by the much higher mass spectrometry signals of 18-oxygen species released after exposing the same amount of sample powder to $^{18}\text{O}_2$ (or conversely, much less sample powder was needed to obtain reasonable ion current intensities, namely ≈ 0.02 g of alkali superoxides compared to ≈ 0.3 g of Na_2O_2 and several g of Li_2O_2).

The $^{18}\text{O}_2$ and ^{18}O - ^{16}O relaxation curves of the superoxides are shown in Figure 3.51. Similar to the peroxides, most of the 18-oxygen is released as ^{18}O - ^{16}O from the sample in the case of KO_2 . In contrast, the amount of 18-oxygen released from RbO_2 as $^{18}\text{O}_2$ and as ^{18}O - ^{16}O is comparable, while

the main oxygen species retrieved from CsO₂ after it was loaded with 18-oxygen is ¹⁸O₂. Thus, in CsO₂ the oxygen incorporation and – since several % of the oxygen contained in the sample were exchanged – also the bulk transport proceed mainly without breaking the covalent O-O bond. The percentage of 18-oxygen released as ¹⁸O₂ increases from KO₂ (10%) to RbO₂ (50%) to CsO₂ (87%). The incorporation and transport of O₂⁻ as a molecular unit is clearly facilitated by a larger cation, i.e. higher polarizability and larger lattice constant.

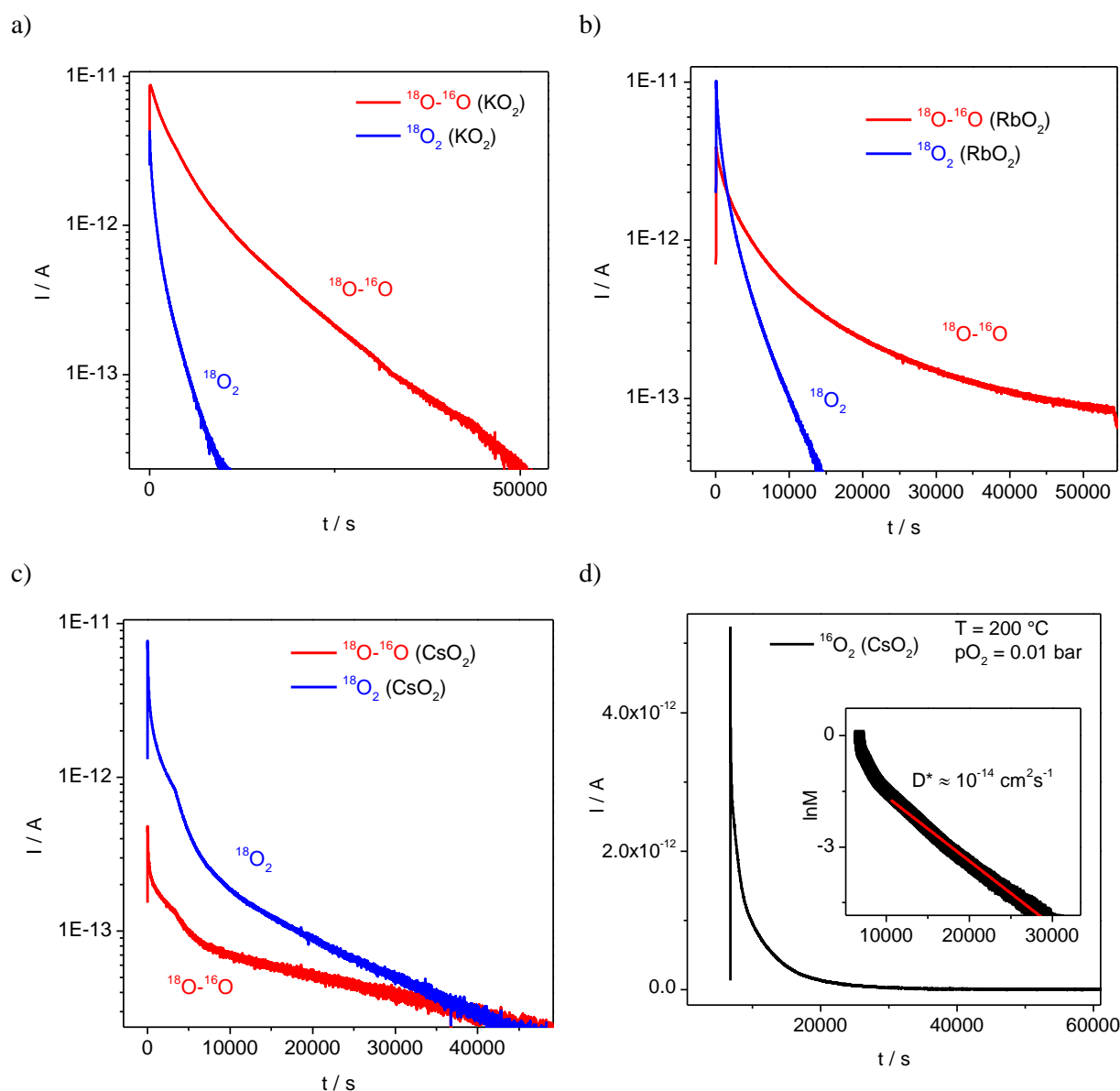


Figure 3.51: ¹⁸O₂ (blue) and ¹⁸O-¹⁶O (red) mass spectrometry signals of a) KO₂, b) RbO₂ and c) CsO₂ in 3 ml/min 1% ¹⁶O₂/N₂ after exposing the sample powder to 1% ¹⁸O₂/N₂ for several hours at 200 °C and d) ¹⁶O₂ mass spectrometry signal of CsO₂ after switching from 3 ml/min 1% ¹⁶O₂/N₂ to 3 ml/min 1% ¹⁸O₂/N₂ at 200 °C. The inset in d) shows linear fit of the logarithmic normalized ion current M vs. t .

For CsO₂, the oxygen exchange is fast enough at 200 °C to observe the full relaxation of the ¹⁶O₂ mass spectrometric signal towards its baseline value within several hours after switching from 3 ml/min 1% ¹⁶O₂/N₂ to 3 ml/min 1% ¹⁸O₂/N₂ (Figure 3.51d). It should be noted that the ¹⁶O₂ amount retrieved from the sample according to its integrated intensity is only about 25% of what is actually contained in the sample (as superoxide) according to the weighed mass of the powder. The mismatch is partly because of the relatively high baseline levels of ¹⁶O₂ ($\approx 4 \cdot 10^{-13}$ A) and ¹⁶O-¹⁸O ($\approx 10^{-12}$ A) in the ¹⁸O₂ gas stream lowering the amount of 16-oxygen that can be still detected as originating from the sample powder. Compared to this, the baseline levels of ¹⁸O₂ and ¹⁶O-¹⁸O in the ¹⁶O₂ gas stream are negligible ($\approx 10^{-14}$ A). Upon purging the capillary containing Cs¹⁸O₂ with 1% ¹⁶O₂, the amount of 18-oxygen released from the sample corresponds to about 50 % of what is expected to be contained in the sample. The remaining difference might be explained by an inhomogenous particle distribution or reaction of some of the CsO₂ with the glass capillary/frit.

The ¹⁶O₂ relaxation can be mainly described by an exponential decay (except for the initial hour) with a relaxation time yielding the superoxide tracer diffusion coefficient of $D^* \approx 10^{-14}$ cm²s⁻¹ and a lower limit of the tracer surface reaction rate constant $k^* < 5 \cdot 10^{-9}$ cm·s⁻¹ at 200 °C assuming diffusion limitation and particles of 500 nm size (due to the extremely high reactivity of CsO₂ with CO₂ and H₂O, the size of the particles could not be determined with SEM so far, as the transfer from the glove box to the SEM requires a short exposure to air; the value of 500 nm is based on the particle size of Na₂O₂ prepared by the same method, i.e. oxidation of the alkali metal). The chemical diffusivity of CsO₂ as determined from dc stoichiometry polarization experiments amounts to $D^\delta \approx 10^{-5}$ cm²s⁻¹ at 200 °C. This large difference between tracer and chemical diffusivity can be explained by the contribution of cation diffusion to D^δ and/or by a large thermodynamic factor of oxygen w_O (relating the chemical diffusivity to the tracer diffusivity^[84]).

For comparison, the oxygen surface exchange rate constant of the perovskite material La_{0.6}Sr_{0.4}Co_{0.2}Fe_{0.8}O_{3-δ} used in solid oxide fuel cells as cathode amounts to $k \approx 10^{-13}$ - 10^{-11} cm·s⁻¹ at the same temperature of 200 °C (estimated by extrapolating high temperature data from isotope exchange depth profiling experiments as well as from electrochemical impedance spectroscopy summarized in ref.^[134]). Hence, the oxygen tracer surface reaction is at least two orders of magnitude faster in CsO₂. On the other side, the oxygen tracer diffusion coefficient in CsO₂ is much lower than that of highly doped solid electrolytes such as yttrium stabilized ZrO₂ with $D \approx 10^{-12}$ cm²s⁻¹ at 200 °C (estimated by extrapolating high temperature data from ref.^[135]).

To verify whether the employed technique of oxygen isotope exchange and gas phase analysis yields reliable results on the oxygen exchange kinetics, the experiment was also carried out with La_{0.6}Sr_{0.4}Co_{0.2}Fe_{0.8}O_{3-δ} (LSCF, commercial powder, purchased from NEXTECH materials) as sample

powder, which is - at least in terms of its oxygen surface reaction - a well-studied material. At 200 °C, the ^{18}O -oxygen exchange with about 0.014 g LSCF powder (which corresponds to about roughly the same molar number as that of CsO_2 previously used) is below the detection limit of the mass spectrometer. Only upon heating the capillary to 600 °C, reasonable intensities of the exchanged oxygen isotopes are obtained (Figure 3.52). The critical length L_c of LSCF is about 10 μm at 600 °C.^[136] The particle size of the powder used in this work is only about 200 nm according to its specific surface area. Therefore, the oxygen exchange can be expected to be surface reaction limited. Indeed, the relaxation of the ^{18}O - ^{16}O signal can be fitted with an exponential decay for all times as expected for surface limitation yielding $k^* \approx 10^{-7} \text{ cm}\cdot\text{s}^{-1}$ at 600 °C and 0.01 bar $p\text{O}_2$. The value is about one order of magnitude higher than the oxygen surface reaction rate constant obtained from the surface resistance by electrochemical impedance spectroscopy on dense material at 1 bar $p\text{O}_2$ ^[137], but comparable to the value from oxygen isotope exchange at 1 bar $p\text{O}_2$ and secondary ion mass spectrometry depth profiling.^[136]

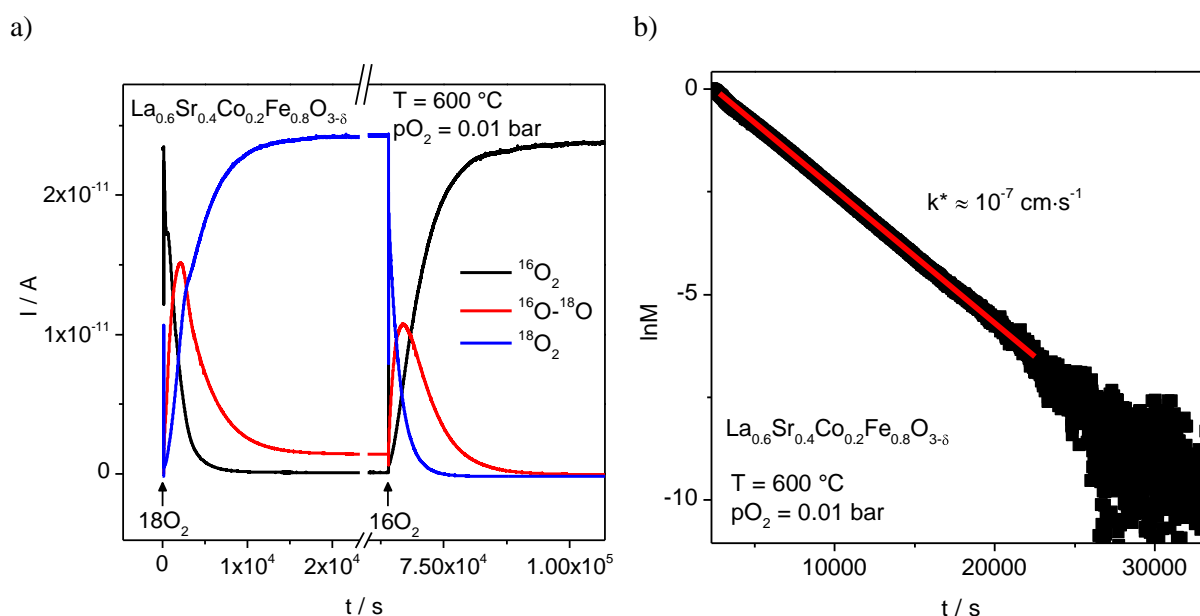


Figure 3.52: a) $^{16}\text{O}_2$ (black), ^{18}O - ^{16}O (red) and $^{18}\text{O}_2$ (blue) mass spectrometry signals of $\text{La}_{0.6}\text{Sr}_{0.4}\text{Co}_{0.2}\text{Fe}_{0.8}\text{O}_{3-\delta}$ after switching 3 ml/min 1% $^{16}\text{O}_2/\text{N}_2$ to 3 ml/min 1% $^{18}\text{O}_2/\text{N}_2$ and then back to 3 ml/min 1% $^{16}\text{O}_2/\text{N}_2$ again at 600 °C and b) linear fit of the logarithmic normalized ion current of the ^{18}O - ^{16}O signal (in 3 ml/min 1% $^{18}\text{O}_2/\text{N}_2$) vs. t .

3.8 Concluding Discussion

Table 3.10 summarizes some of the properties and parameters of the alkali peroxides and superoxides as obtained in this work.

With increasing atomic number of the alkali ion, the color changes from bright white to ivory for the peroxides and the materials become softer (i.e. a higher density is achieved upon pressing at room temperature). The alkali superoxides appear yellow as powder and orange as dense pellet. CsO₂ and RbO₂ are softer materials than KO₂ and require lower pressing pressures to achieve pellets with a density close to the theoretical density. This indicates an increased polarizability and increasing mobility of defects on both cation and anion sub-lattice. The increase of the anion mobility with increasing atomic number is confirmed by oxygen isotope exchange measurements. The most sluggish oxygen exchange is observed for Li₂O₂, but it is greatly enhanced for Na₂O₂ and further for KO₂. For the heaviest superoxide CsO₂, almost all exchanged oxygen is retrieved again as ¹⁸O₂, i.e. the O-O bond remained intact both during surface incorporation and bulk transport.

Table 3.10: Overview table on M₂O₂ (M = Li, Na, K) and MO₂ (M = K, Rb, Cs).

	Li ₂ O ₂	Na ₂ O ₂	K ₂ O ₂	KO ₂	RbO ₂	CsO ₂
Color (powder)	white	white - ivory	ivory	bright yellow	yellow	yellow
Relative density / % (green body)	65 – 70 (750 MPa isostatic)	75 – 80 (750 MPa isostatic)	90 (250 MPa uniaxial)	> 95 (500 MPa uniaxial)	> 95 (250 MPa uniaxial)	> 95 (250 MPa uniaxial)
Reactivity with air at RT	slow	modest	fast	fast	-	extremely fast
Fraction of molecular O₂ exchange	0.3 (only surface)	0.2 (into bulk)	N/A	0.1 (into bulk)	0.5 (into bulk)	0.87 (into bulk)
ε_r	35	24	22	29	15	13
				as prepared	an-nealed	

	Li₂O₂	Na₂O₂	K₂O₂	KO₂		RbO₂	CsO₂	
σ_{eon}	E_a / eV	1.3 ±0.1	1.15 ±0.03	N/A	N/A	0.84 ±0.03	0.91 ±0.02	1.04 ±0.02
	pO₂ dependence	+0.25 ^c	+0.17	positive	negative	negative	negative	-0.25 ±0.07
	Carrier	p (trapped as $O_{2O_2}^{\bullet}$)			n (trapped as O_{2O_2}')			
σ_{ion}	E_a / eV	0.95 ±0.05	1.3 ±0.05	0.9 ±0.03	0.78–1.3	0.56 ±0.01	0.8 ±0.02	0.81 ±0.02
	pO₂ dependence	const.	-0.04	const.	const.	-0.5	-0.23	-0.37
	Carrier	V_{Li}'	Na_i^{\bullet}	K_i^{\bullet} possibly $V_{O_2}^{\bullet\bullet}$	K_i^{\bullet} and/or $V_{O_2}^{\bullet}$	K_i^{\bullet} and/or $V_{O_2}^{\bullet}$	Rb_i^{\bullet} and/or $V_{O_2}^{\bullet}$	Cs_i^{\bullet} and/or $V_{O_2}^{\bullet}$

The electronic and ionic conductivities of the studied alkali peroxide and superoxides are found within a range of one and two orders of magnitude at 200 °C (Figure 3.53a,b). The dependences of conductivities on the atomic mass are non-monotonic and furthermore, the most significant differences are found between compounds that are chemically the most similar (e.g. compare conductivities of Li₂O₂ vs. Na₂O₂ and RbO₂ vs. CsO₂). The activation energies for both electronic and ionic transport range between 0.8 – 1.3 eV with a slight tendency of E_a(σ_{eon}) > E_a(σ_{ion}), but show likewise no clear trend indicating the influence of the cation size or anion charge.

The cation conductivities (e.g. $\approx 10^{-9} \Omega^{-1}\text{cm}^{-1}$ for Li₂O₂ and $\approx 10^{-11} \Omega^{-1}\text{cm}^{-1}$ for Na₂O₂ at 100 °C) are far below those of typical solid electrolytes (e.g. $\approx 5 \cdot 10^{-3} \Omega^{-1}\text{cm}^{-1}$ for Li₇La₃Zr₂O₁₂^[138] and $\approx 10^{-2} \Omega^{-1}\text{cm}^{-1}$ for NaAl₁₁O₁₇^[139] at 100 °C) - even more so at room temperature due to their much higher activation energy – but on the other hand comparable to that of a well-investigated cathode material already employed in conventional alkali ion batteries (viz. LiFePO₄ $\approx 10^{-11}$ - $10^{-10} \Omega^{-1}\text{cm}^{-1}$ at 100 °C^[140]). The electronic conductivity in the studied materials is, however, much lower (e.g. $\approx 10^{-11} \Omega^{-1}\text{cm}^{-1}$ for Li₂O₂ and $\approx 5 \cdot 10^{-9} \Omega^{-1}\text{cm}^{-1}$ for K₂O at 100 °C) than that of LiFePO₄ ($\approx 2 \cdot 10^{-7}$ - $4 \cdot 10^{-6} \Omega^{-1}\text{cm}^{-1}$ ^[140]). According to the oxygen partial pressure dependence of the electronic conductivity, the alkali peroxides and superoxides exhibit p- and n-type conductivity, respectively.

The chemical diffusivities of the peroxides and superoxides are within a range of one order of magnitude too. The fastest ambipolar diffusion is obtained for the heaviest compounds RbO₂ and CsO₂ (the latter is not included in the Arrhenius plot due to a much scattering and hence unreliable

^c only at high pO₂, decreasing for lower pO₂.

temperature dependence, probably because of the small stoichiometry polarization voltages of only few mV in the raw data; D^δ of CsO_2 seems to be up to half an order of magnitude higher than the value of RbO_2 at 200 °C and 1000 ppm $p\text{O}_2$). The chemical diffusion coefficient is composed of contributions from both electronic and ionic diffusion weighted by the corresponding trapping factors and the transference number of the other species (see also equation (29)). Considerable association of oppositely charged defects is expected for low temperatures, but the extent of trapping and the values of the trapping factors are not generally known. Since the activation energies of σ_{eon} and σ_{ion} are comparable, it is presently not possible to decide whether the ambipolar diffusion is limited by electronic or ionic transport.

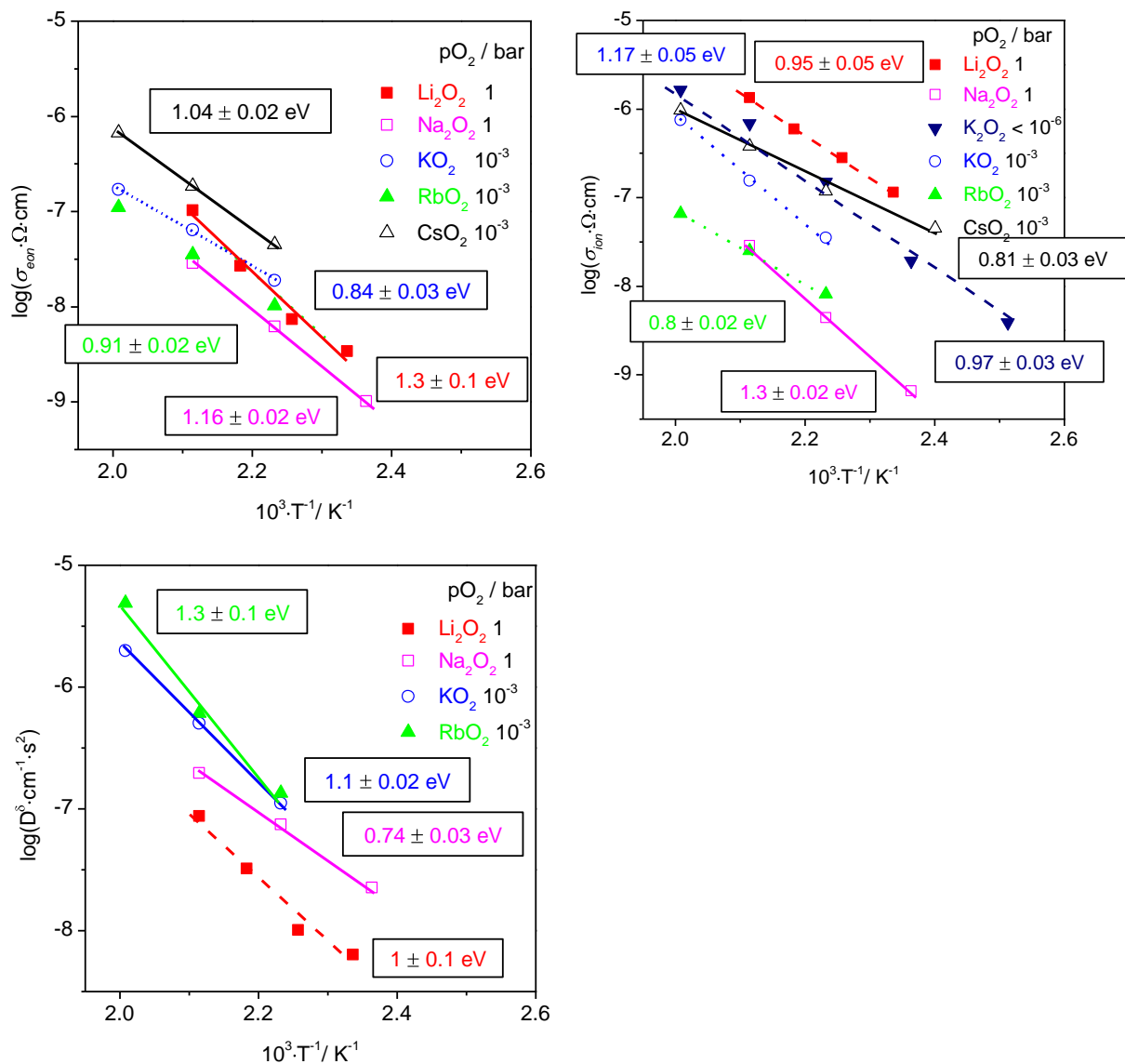


Figure 3.53: Temperature dependence of the electronic and ionic conductivity and chemical diffusivity of the studied alkali peroxides and oxides. Li_2O_2 , K_2O_2 , RbO_2 and CsO_2 pellets were only cold pressed, Na_2O_2 and KO_2 pellets sintered at 475 °C and 450 °C respectively. The ionic conductivity of K_2O_2 was approximated by the total bulk conductivity from ac impedance spectroscopy.

Unlike in conventional lithium ion batteries, the discharging of the alkali-oxygen battery is not associated with a solid state phase transformation of the host material or intercalation of the alkali metal into a typically mixed conducting cathode. Instead, the cathodic reaction takes place only at the interface between the electrolyte and the current collector and/or already precipitated alkali peroxide and superoxide. The alkali ions are supplied via the liquid electrolyte without the need of ionic bulk transport in the peroxides/superoxides. The electronic conduction is more likely to be relevant and a potential bottleneck in the formation and decomposition kinetics at the cathode. In principle, three different mechanisms upon discharging the cell are conceivable (after the first nuclei of M_xO_2 has formed), which are depicted in Figure 3.54.

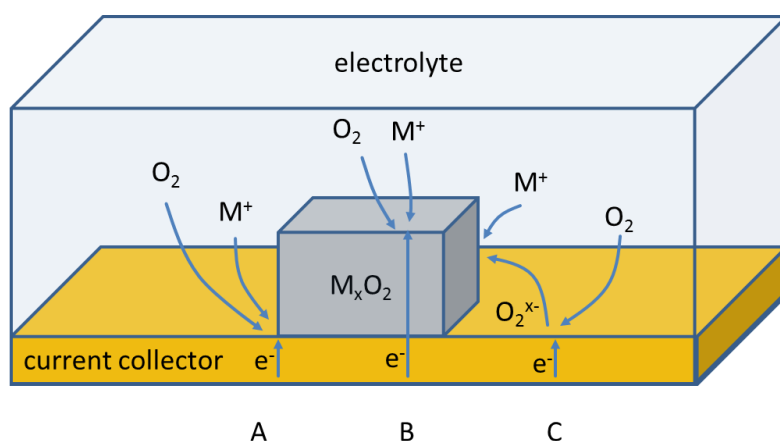


Figure 3.54: Schematic representation of the possible cathodic reaction mechanisms in peroxide/superoxide based alkali-oxygen batteries. See the list below for an explanation of the different mechanisms A, B and C.

- A – Oxygen reduction and peroxide/superoxide precipitation take place at the triple phase boundary between electrolyte, current collector and already deposited M_xO_2 .
- B – Oxygen reduction and peroxide/superoxide precipitation occur at the two phase boundary between the electrolyte and already deposited M_xO_2 .
- C – Oxygen is reduced at the current collector and O_2^{x-} species diffuse through the electrolyte and precipitate with Li^+ from the electrolyte on the M_xO_2 surface.^[141]

Mechanisms A and C are not relying on electronic transport in M_xO_2 . However, the former is limited to the deposition of only a single monolayer of M_xO_2 , while the latter requires diffusion of chemically reactive O_x^- species with limited solubility in liquid organic electrolytes. In mechanism B, the electrons need to be supplied via M_xO_2 either by electronic tunneling for very thin films or in the case of thicker films by hopping of electronic charge carriers in the bulk or at the surface.

It has been previously hypothesized that the low overpotential of sodium and potassium-oxygen batteries with superoxides precipitating at the cathode might be due to a higher electronic conductivity in NaO_2 and KO_2 compared to Li_2O_2 .^{[51],[50]} This seemed to have been supported by an earlier study reporting an extremely high electronic conductivity of KO_2 of $> 10 \Omega^{-1}cm^{-1}$ at room temperature.^[76]

However, according to the results of the present thesis, this value has to be considered incorrect and grossly exaggerated. The electrical resistance of the cell Au | KO₂ | Au (1 mm thick and 5 mm diameter) at room temperature is even beyond the measurement limit of an electrometer with > 100 GΩ input resistance. The actual electronic conductivity of KO₂ (and Li₂O₂ for comparison) at room temperature can only be estimated by extrapolating high temperature data yielding $\approx 10^{-14} \Omega^{-1}\text{cm}^{-1}$ for KO₂ and $\approx 10^{-16} \Omega^{-1}\text{cm}^{-1}$ for Li₂O₂. Thus, the electronic conductivity of KO₂ is not as extraordinary high as previously assumed (such a huge error of more than 10 orders of magnitude is likely explained by a short circuit in the measurements cell), but still seems to be higher than that of Li₂O₂. The values should be taken carefully though, since they are very sensitive to errors in the activation energies, which are only based on few data points of the electronic conductivity at much higher temperatures.

4 Summary

In the present thesis, the electrical transport properties and reaction kinetics of alkali peroxides and superoxides have been investigated. This class of materials recently caught attention as reaction products at the cathode of reversible alkali-oxygen batteries, but the defect chemistry, charge transport and in particular the oxygen exchange kinetics and mechanism compared to oxides is likewise interesting from a fundamental point of view. However, the high reactivity of the materials with water and carbon dioxide and their limited stability ranges makes the sample preparation challenging.

Electrochemical techniques such as impedance spectroscopy and dc polarization measurements with selectively blocking electrodes and electromotive force measurements were employed for the electrochemical characterization of the transport processes. The electrical conductivity was separated into its electronic and ionic contributions, and chemical diffusivity was obtained from the transient behavior of the polarized cells with selectively blocking electrodes. All materials exhibit mixed conductivity, with more or less predominance of the ionic conductivity.

The oxygen partial pressure was used as a control parameter to identify the main electronic charge carrier. The pO_2 dependence of the electronic conductivity supports p-type (hole) conduction in alkali peroxides and n-type (electron) conduction in alkali superoxides. With electron paramagnetic resonance spectroscopy superoxide defects were identified in alkali peroxides, i.e. the holes are localized forming superoxide ions. The most probable electronic transport mechanism is the hopping of a hole, transforming a neighboring peroxide ion into superoxide ion. Conversely, electronic transport in alkali superoxides occurs by electron hopping, i.e. the reduction of superoxide to a peroxide defect.

Considerable attention was paid to the possibility that ionic charge carriers are not entirely blocked at nominally ionic blocking electrodes such as sputtered films of gold. In such a case, the apparent electronic conductivity as determined from dc conductivity measurements would actually correspond to ionic transport and fast oxygen exchange. This phenomenon can indeed be shown to be relevant at least for the alkali superoxides at high oxygen partial pressures by cross-checking with electromotive force measurements. A setup was developed in course of this thesis to measure the cell voltage of $pO_2(1) | \text{electrode} | \text{sample pellet} | \text{electrode} | pO_2(2)$ for $0.01 \leq pO_2(1)/pO_2(2) \leq 1$ without the need of an additional sealant.

By means of donor doping it was possible to identify the actual cation transport mechanism in alkali peroxides. Cation vacancies are found to be the main ionic carrier in lithium peroxide in accordance to theoretical predictions, whereas an interstitial mechanism seems to prevail in sodium and potassium peroxide. The formation and migration of interstitial cations of relatively large size is possibly facilitated by the asymmetric occupation of the anion site by the dumbbell shaped peroxide ions.

Likewise, in alkali superoxides a cation interstitial mechanism is consistent with the negative pO_2 dependence of the ionic conductivity, which, however, may also be due to the transport of superoxide vacancies. Further conductivity experiments with selectively blocking electrodes (i.e. alkali metal | alkali conductor | alkali superoxide | alkali conductor | alkali metal) are required in the future to distinguish between alkali ion and superoxide transport. The fast oxygen exchange into the bulk observed for alkali superoxides (by oxygen isotope exchange and gas phase analysis) at relatively low temperatures already indicates that the superoxide vacancies might contribute significantly to the ionic transport in these compounds.

The oxygen isotope exchange experiments further show that the covalent oxygen bond tends to get broken upon exchanging oxygen in Li_2O_2 , Na_2O_2 and KO_2 , while the large cation radius in CsO_2 provides a crystallographic framework for the transport of O_2^- as a molecular unit. The surface reaction in CsO_2 proceeds very fast even compared to solid oxide fuel cells cathodes based on oxide materials. The enhanced kinetics of oxygen incorporation, which requires only the transfer of a single electron and annihilation of a superoxide vacancy in the first monolayer of the material, is also reflected in the unusually fast EMF response of the cell $pO_2(1) | Pt | CsO_2 | Pt | pO_2(2)$ at low temperatures. The promising oxygen exchange kinetics in alkali superoxides should be further investigated by an independent method such as analysis of ^{18}O profiles in dense pellets by secondary ion mass spectrometry.

Defect models were proposed for alkali peroxides and superoxides and the dependence of defect concentration upon the oxygen partial pressure and the alkali metal activity (Kröger-Vink diagrams) was derived from the mass action laws and proper approximations of the electroneutrality condition. For lithium peroxide – the technologically most relevant of the studied materials - the defect model with lithium vacancies and defect electrons as main charge carriers was refined by taking into account strong association of oppositely charged defects, namely the trapping of holes at lithium vacancies and the trapping of lithium vacancies at donor impurities. Theoretical studies predicting migration and interaction enthalpies of the defects are lacking for the other alkali peroxides and superoxides, but such trapping effects are probably also relevant for these systems (at least at low temperatures).

Moreover, it has been shown in the present thesis that gold nano-particles on lithium peroxide result in an electronic redistribution at the surface yielding a high concentration of holes trapped as superoxide defects. Such acceptor doping is expected to increase the electronic transport in Li_2O_2 and thus decrease the high overpotential of the Li- O_2 cell if its origin is found in the poor electron conduction.

The findings of this work are considered important for understanding and addressing limitations and problems in the cathodic reaction in alkali oxygen batteries and indicate that for Li_2O_2 the presence of superoxide ions is ambivalent: on the one hand they are degrading the common electrolytes, but one

the other hand they necessary for the electronic transport. Furthermore, the comparison with the compounds of the heavier alkali metals elucidates systematic trends: p-type electronic conductivity in peroxides compared to n-type conductivity in superoxides, increasing contribution of superoxide/peroxide vacancies to the ionic transport (as well as increasing amount of dioxygen species exchanged without bond breaking for the superoxides) with increasing cation size. Thus, a more general understanding of this important class of materials could be achieved.

References

- [1] A. L. Allred, *Journal of Inorganic and Nuclear Chemistry* 1961, 17, 215.
- [2] I. I. Vol'nov, *Peroxides, in Superoxides, and Ozonides of Alkali and Alkaline Earth metals*, Plenum Press, New York 1966.
- [3] N.-G. Vannerberg, in *Progress in Inorganic Chemistry*, John Wiley & Sons, Inc., 1962, 125.
- [4] W. Hesse, M. Jansen, W. Schnick, *Progress in Solid State Chemistry* 1989, 19, 47.
- [5] L. Q. Brin, A. Brin, *USA Patent 359,424*, 1887.
- [6] W. B. Jensen, *Journal of Chemical Education* 2009, 86, 1266.
- [7] J. D. Bernal, E. Djaltova, I. Kasarnowsky, S. Reichstein, A. G. Ward, *Zeitschrift Fur Kristallographie* 1935, 92, 344.
- [8] W. Kassatochkin, W. Kotow, *The Journal of Chemical Physics* 1936, 4, 458.
- [9] A. Helms, W. Klemm, *Zeitschrift für anorganische und allgemeine Chemie* 1939, 241, 97.
- [10] D. H. Templeton, C. H. Dauben, *Journal of the American Chemical Society* 1950, 72, 2251.
- [11] H. Föppl, *Zeitschrift für anorganische und allgemeine Chemie* 1957, 291, 12.
- [12] R. L. Tallman, J. L. Margrave, S. W. Bailey, *Journal of the American Chemical Society* 1957, 79, 2979.
- [13] R. M. Bovard, *Aerospace Medicine* 1960, 31, 407.
- [14] D. L. Kraus, A. W. Petrocelli, *The Journal of Physical Chemistry* 1962, 66, 1225.
- [15] M. M. Markowitz, E. W. Dezmelyk, (Ed: D. A. Keating), Foote Mineral Company, Research and Engineering Center, Exton 1964, 190.
- [16] A. J. Capotosto, A. W. Petrocelli, *US Air Force Technical Documentary Report AMRL-TDR* 1968, 1.
- [17] J. L. Manganaro, *Industrial & Engineering Chemistry Process Design and Development* 1970, 9, 1.
- [18] H. Ducros, C. Laurent, F. Joannes, *Rev Corps Sante Armees Terre Mer Air* 1970, 11, 887.
- [19] F. E. Clarke, *Journal of the American Society of Naval Engineers* 1956, 68.
- [20] M. A. Fahim, J. D. Ford, *The Chemical Engineering Journal* 1983, 27, 21.
- [21] O. V. Kedrovskii., I. V. Kovtunencko, E. V. Kiseleva, A. A. Bundel, *Russian Journal of Physical Chemistry* 1967, 41, 205.
- [22] A. F. Mayorova, S. N. Mudretsova, M. N. Mamontov, P. A. Levashov, A. D. Rusin, *Thermochemica Acta* 1993, 217, 241.
- [23] K. S. Gavrichev, V. E. Gorbunov, M. V. Gorbacheva, A. F. Maiorova, S. N. Mudretsova, Y. Y. Skolis, M. L. Kovba, *Zhurnal Neorganicheskoi Khimii* 1997, 42, 1158.

- [24] E. Zimmermann, K. Hack, D. Neuschütz, *Calphad* 1995, 19, 119; M. J. Tribelhorn, M. E. Brown, *Thermochimica Acta* 1995, 255, 143.
- [25] J. L. Jorda, T. K. Jondo, *Journal of Alloys and Compounds* 2001, 327, 167.
- [26] S. L. Qiu, C. L. Lin, J. Chen, M. Strongin, *Physical Review B* 1990, 41, 7467.
- [27] A. Band, A. Albu-Yaron, T. Livneh, H. Cohen, Y. Feldman, L. Shimon, R. Popovitz-Biro, V. Lyahovitskaya, R. Tenne, *The Journal of Physical Chemistry B* 2004, 108, 12360.
- [28] Y. Sun, Z. Liu, P. Pianetta, D.-I. Lee, *Journal of Applied Physics* 2007, 102.
- [29] M. Y. Sinev, V. N. Korchak, O. V. Krylov, *Kinetics and Catalysis* 1986, 27, 1110.
- [30] K. Otsuka, A. A. Said, K. Jinno, T. Komatsu, *Chemistry Letters* 1987, 16, 77.
- [31] H. Shimada, J. Galuszka, in *Studies in Surface Science and Catalysis*, Vol. 73 (Eds: K. J. Smith, E. C. Sanford), Elsevier, 1992, 99.
- [32] I. Balint, G. Dobrescu, M. Vass, *Revue Roumaine De Chimie* 1997, 42, 1009.
- [33] H. Yamashita, Y. Machida, A. Tomita, *Applied Catalysis A: General* 1991, 79, 203.
- [34] J. H. Lunsford, X. Yang, K. Haller, J. Laane, G. Mestl, H. Knoezinger, *The Journal of Physical Chemistry* 1993, 97, 13810.
- [35] Y.-D. Liu, H.-B. Zhang, G.-D. Lin, Y.-Y. Liao, K. R. Tsai, *Journal of the Chemical Society, Chemical Communications* 1994, 1871.
- [36] H. B. Zhang, G. D. Lin, H. L. Wan, Y. D. Liu, W. Z. Weng, J. X. Cai, Y. F. Shen, K. R. Tsai, *Catalysis Letters* 2001, 73, 141.
- [37] L. Wang, X. Yi, W. Weng, C. Zhang, X. Xu, H. Wan, *Catalysis Letters* 2007, 118, 238.
- [38] Y. Wang, K. Otsuka, K. Ebitani, *Catalysis Letters* 1995, 35, 259.
- [39] L. M. Madeira, R. M. Martín-Aranda, F. J. Maldonado-Hódar, J. L. G. Fierro, M. F. Portela, *Journal of Catalysis* 1997, 169, 469.
- [40] G. Mestl, M. P. Rosynek, J. H. Lunsford, *The Journal of Physical Chemistry B* 1997, 101, 9329.
- [41] E. I. Vovk, E. Emmez, M. Erbudak, V. I. Bukhtiyarov, E. Ozensoy, *The Journal of Physical Chemistry C* 2011, 115, 24256.
- [42] A. M. Bol'shakov, V. V. Minin, L. V. Khmelevskaya, *Russian Journal of Inorganic Chemistry* 1998, 43, 1648.
- [43] H. X. Dai, C. F. Ng, C. T. Au, *Applied Catalysis A: General* 2000, 202, 1.
- [44] M. Machida, Y. Murata, K. Kishikawa, D. Zhang, K. Ikeue, *Chemistry of Materials* 2008, 20, 4489.
- [45] X. Wang, Y. Zhang, Q. Li, Z. Wang, Z. Zhang, *Catalysis Science & Technology* 2012, 2, 1822.
- [46] G. Corro, U. Pal, E. Ayala, E. Vidal, *Catalysis Today* 2013, 212, 63.
- [47] K. M. Abraham, Z. Jiang, *Journal of The Electrochemical Society* 1996, 143, 1.
- [48] Z. Peng, S. A. Freunberger, Y. Chen, P. G. Bruce, *Science* 2012, 337, 563.

- [49] Q. Sun, Y. Yang, Z.-W. Fu, *Electrochemistry Communications* 2012, 16, 22.
- [50] P. Hartmann, C. L. Bender, M. Vračar, A. K. Dürr, A. Garsuch, J. Janek, P. Adelhelm, *Nature Materials* 2013, 12, 228.
- [51] X. Ren, Y. Wu, *Journal of the American Chemical Society* 2013, 135, 2923.
- [52] N. Garcia-Araez, P. Novák, *Journal of Solid State Electrochemistry* 2013, 17, 1793.
- [53] Y.-C. Lu, Y. Shao-Horn, *The Journal of Physical Chemistry Letters* 2013, 4, 93.
- [54] B. M. Gallant, D. G. Kwabi, R. R. Mitchell, J. Zhou, C. V. Thompson, Y. Shao-Horn, *Energy & Environmental Science* 2013, 6, 2518.
- [55] R. R. Mitchell, B. M. Gallant, Y. Shao-Horn, C. V. Thompson, *The Journal of Physical Chemistry Letters* 2013, 4, 1060.
- [56] L. Zhong, R. R. Mitchell, Y. Liu, B. M. Gallant, C. V. Thompson, J. Y. Huang, S. X. Mao, Y. Shao-Horn, *Nano Letters* 2013, 13, 2209.
- [57] V. Viswanathan, J. K. Nørskov, A. Speidel, R. Scheffler, S. Gowda, A. C. Luntz, *The Journal of Physical Chemistry Letters* 2013, 4, 556.
- [58] Y.-C. Lu, E. J. Crumlin, G. M. Veith, J. R. Harding, E. Mutoro, L. Baggetto, N. J. Dudney, Z. Liu, Y. Shao-Horn, *Scientific Reports* 2012, 2.
- [59] S. Nicola, *Nanotechnology* 2009, 20, 445703.
- [60] M. K. Y. Chan, E. L. Shirley, N. K. Karan, M. Balasubramanian, Y. Ren, J. P. Greeley, T. T. Fister, *The Journal of Physical Chemistry Letters* 2011, 2, 2483.
- [61] K. C. Lau, L. A. Curtiss, J. Greeley, *The Journal of Physical Chemistry C* 2011, 115, 23625.
- [62] M. Radin, F. Tian, D. Siegel, *Journal of Materials Science* 2012, 47, 7564.
- [63] M. D. Radin, J. F. Rodriguez, F. Tian, D. J. Siegel, *Journal of the American Chemical Society* 2012, 134, 1093.
- [64] K. C. Lau, R. S. Assary, P. Redfern, J. Greeley, L. A. Curtiss, *The Journal of Physical Chemistry C* 2012, 116, 23890.
- [65] V. Timoshevskii, Z. Feng, K. H. Bevan, J. Goodenough, K. Zaghbi, *Applied Physics Letters* 2013, 103.
- [66] J. S. Hummelshøj, J. Blomqvist, S. Datta, T. Vegge, J. Rossmeisl, K. S. Thygesen, A. C. Luntz, K. W. Jacobsen, J. K. Nørskov, *The Journal of Chemical Physics* 2010, 132.
- [67] Y. Mo, S. P. Ong, G. Ceder, *Physical Review B* 2011, 84, 205446.
- [68] J. Chen, J. S. Hummelshøj, K. S. Thygesen, J. S. G. Myrdal, J. K. Nørskov, T. Vegge, *Catalysis Today* 2011, 165, 2.
- [69] V. Viswanathan, K. S. Thygesen, J. S. Hummelshøj, J. K. Nørskov, G. Girishkumar, B. D. McCloskey, A. C. Luntz, *The Journal of Chemical Physics* 2011, 135.
- [70] S. P. Ong, Y. Mo, G. Ceder, *Physical Review B* 2012, 85, 081105.
- [71] J. Kang, Y. S. Jung, S.-H. Wei, A. C. Dillon, *Physical Review B* 2012, 85, 035210.
- [72] J. S. Hummelshøj, A. C. Luntz, J. K. Nørskov, *The Journal of Chemical Physics* 2013, 138.

- [73] O. Gerbig, R. Merkle, J. Maier, *Advanced Materials* 2013, 25, 3129.
- [74] J. Rudolph, *Zeitschrift für Naturforschung Part A - Astrophysik, Physik und Physikalische Chemie* 1958, 13, 757.
- [75] M. Königstein, *Journal of Solid State Chemistry* 1999, 147, 478.
- [76] A. U. Khan, S. D. Mahanti, *The Journal of Chemical Physics* 1975, 63, 2271.
- [77] J. Maier, *Physical Chemistry of Ionic Materials*, John Wiley & Son Ltd., West Sussex 2004.
- [78] F. A. Kröger, H. J. Vink, in *Solid State Physics, 3: Advances in Research and Applications*, Vol. 3 (Eds: F. Seitz, D. Turnbull), Academic Press, New York 1956, 307.
- [79] F. Fehér, I. Von Wilucki, G. Dost, *Chemische Berichte* 1953, 86, 1429.
- [80] G. Brauer, *Handbuch der präparativen anorganischen Chemie*, Enke Ferdinand, Stuttgart 1981.
- [81] B. Predel, in *SpringerMaterials - The Landolt-Börnstein Database*, (Ed: O. Madelung).
- [82] B. Predel, in *SpringerMaterials - The Landolt-Börnstein Database*, (Ed: O. Madelung).
- [83] I. Yokota, *Journal of the Physical Society of Japan* 1961, 16, 2213.
- [84] J. Maier, in *Modern Aspects Of Electrochemistry*, Vol. 41 (Eds: C. Vayenas, R. White, M. Gamboa-Aldeco), Springer New York, 2007, 1.
- [85] E. Barsoukov, J. R. Macdonald, *Impedance Spectroscopy*, John Wiley & Sons, New Jersey 2005.
- [86] M. E. Orazem, B. Tribollet, *Electrochemical Impedance Spectroscopy*, John Wiley & Sons, New Jersey 2008.
- [87] K. S. Cole, R. H. Cole, *The Journal of Chemical Physics* 1941, 9, 341.
- [88] J. Fleig, *Solid State Ionics* 2002, 150, 181.
- [89] J. Crank, *The mathematics of diffusion / by J. Crank*, Clarendon Press, Oxford [England] 1975.
- [90] I. Denk, W. Münch, J. Maier, *Journal of the American Ceramic Society* 1995, 78, 3265.
- [91] H. H. Eysel, S. Thym, *Zeitschrift für anorganische und allgemeine Chemie* 1975, 411, 97.
- [92] L. Barin, I. Knacke, *Thermochemical properties of inorganic substances*, Springer, 1973.
- [93] T. V. Rode, T. A. Dobrynina, G. A. Golder, *Bulletin of the Academy of Sciences of the USSR, Division of chemical science* 1954, 4, 545.
- [94] I. I. Vol'nov, *Russian Chemical Reviews* 1965, 34.
- [95] A. B. Tsentsiper, Z. I. Kuznetsova, *Bulletin of the Academy of Sciences of the USSR, Division of chemical science* 1965, 14, 1873.
- [96] Y. A. Ferapontov, N. V. Kokoreva, N. P. Kozlova, M. A. Ul'yanova, *Russian Journal of General Chemistry* 2009, 79, 891.
- [97] K. P. C. Yao, D. G. Kwabi, R. A. Quinlan, A. N. Mansour, A. Grimaud, Y.-L. Lee, Y.-C. Lu, Y. Shao-Horn, *Journal of The Electrochemical Society* 2013, 160
- [98] T. Osaka, I. Shindo, *Solid State Communications* 1984, 51, 421.

- [99] E. G. Bunzel, E. J. Kohlmeyer, *Zeitschrift für anorganische Chemie* 1947, 254, 1.
- [100] L. Brewer, J. Margrave, *Journal of physical chemistry* 1955, 59, 421.
- [101] S. Chaoming, W. Ping, A. M. Hernán, *Nature* 2008, 453, 629.
- [102] J. Fleig, J. Maier, *Journal of the American Ceramic Society* 1999, 82, 3485.
- [103] H. J. Juretschke, R. Landauer, J. A. Swanson, *Journal of Applied Physics* 1956, 27, 838.
- [104] M. W. den Otter, H. J. M. Bouwmeester, B. A. Boukamp, H. Verweij *Journal of The Electrochemical Society* 2001, 148, J1.
- [105] C. K. Ho, S. W. Webb, (Eds: C. K. Ho, S. W. Webb), *Gas Transport in Porous Media*, Springer, Dordrecht 2006, 13.
- [106] G. Brouwer, *Philps Research Reports* 1954, 366.
- [107] R. Shannon, *Acta Crystallographica Section A* 1976, 32, 751.
- [108] M. Sharon, R. R. Pradhananga, *Journal of Solid State Chemistry* 1981, 40, 20.
- [109] J. M. Garcia-Lastra, J. D. Bass, K. S. Thygesen, *The Journal of Chemical Physics* 2011, 135.
- [110] C. Naccache, P. Meriaudeau, M. Che, A. J. Tench, *Transactions of the Faraday Society* 1971, 67, 506.
- [111] D. M. Lindsay, D. R. Herschbach, A. L. Kwiram, *The Journal of Chemical Physics* 1974, 60, 315.
- [112] M. Wilkening, V. Epp, A. Feldhoff, P. Heitjans, *The Journal of Physical Chemistry C* 2008, 112, 9291.
- [113] B. Henderson, J. E. Wertz, *Advances in Physics* 1968, 17, 749.
- [114] J. Maier, *Journal of the American Ceramic Society* 1993, 76, 1223.
- [115] M. Leonardt, R. A. De Souza, J. Claus, J. Maier, *Journal of The Electrochemical Society* 2002, 149, J19.
- [116] Y. Zhao, C. Ban, J. Kang, S. Santhanagopalan, G.-H. Kim, S.-H. Wei, A. C. Dillon, *Applied Physics Letters* 2012, 101.
- [117] B. R. Panda, Chattopadhyay, *Journal of Nanoscience and Nanotechnology* 2007, 7, 1911.
- [118] B. D. Cullity, *Elements of x-ray diffraction*, Addison-Wesley Publishing Company, inc., Reading, Massachusetts 1978.
- [119] N. Ohtori, F. Ueno, T. Furukawa, *Electrochemistry* 2005, 73, 597.
- [120] M. Spaeth, K. D. Kreuer, T. Dippel, J. Maier, *Solid State Ionics* 1997, 97, 291.
- [121] T. Bremm, M. Jansen, *Zeitschrift für anorganische und allgemeine Chemie* 1992, 610, 64.
- [122] C. M. Mari, R. M. Cappello, C. Galbiati, *Solid State Ionics* 1998, 111, 93.
- [123] G. F. Carter, J. L. Margrave, D. H. Templeton, *Acta Crystallographica* 1952, 5, 851.
- [124] M. Ziegler, M. Rosenfeld, W. Kanzig, P. Fischer, *Helvetica Physica Acta* 1976, 49, 57.
- [125] C. F. Knights, B. A. Phillips, *Journal of Nuclear Materials* 1979, 84, 196.
- [126] R. Hoppe, K.-H. Arend, *Zeitschrift für anorganische und allgemeine Chemie* 1962, 314, 4.
- [127] D. E. King, *Journal of Vacuum Science & Technology A* 1995, 13, 1247.

- [128] E. Irissou, M.-C. Denis, M. Chaker, D. Guay, *Thin Solid Films* 2005, 472, 49.
- [129] V. Y. Dudarev, A. B. Tsentsiper, M. S. Dobrolyubova, *Kristallografiya* 1973, 18, 759
- [130] S. Kuwata, N. Miura, N. Yamazoe, T. Seiyama, *Chemistry Letters* 1984, 13, 981.
- [131] J. Kuwano, A. Wakagi, M. Kato, *Journal of The Electrochemical Society* 1992, 139, L113.
- [132] H. J. M. Bouwmeester, H. Kruidhof, A. J. Burggraaf, *Solid State Ionics* 1994, 72, Part 2, 185.
- [133] J. A. Kilner, in *Proceedings of the Second International Symposium on Ionic and Mixed Conducting Ceramics*, (Eds: T. A. Ramanarayanan, W. L. Worrell, H. L. Tuller), The Electrochemical Society, Pennington 1994, 174
- [134] N. J. Simrick, A. Bieberle-Hütter, T. M. Ryll, J. A. Kilner, A. Atkinson, J. L. M. Rupp, *Solid State Ionics* 2012, 206, 7.
- [135] P. S. Manning, J. D. Sirman, R. A. De Souza, J. A. Kilner, *Solid State Ionics* 1997, 100, 1.
- [136] B. C. H. Steele, J.-M. Bae, *Solid State Ionics* 1998, 106, 255.
- [137] F. S. Baumann, J. Fleig, H.-U. Habermeier, J. Maier, *Solid State Ionics* 2006, 177, 1071.
- [138] R. Murugan, V. Thangadurai, W. Weppner, *Angewandte Chemie International Edition* 2007, 46, 7778.
- [139] M. S. Whittingham, R. A. Huggins, *The Journal of Chemical Physics* 1971, 54, 414.
- [140] R. Amin, J. Maier, P. Balaya, D. P. Chen, C. T. Lin, *Solid State Ionics* 2008, 179, 1683.
- [141] P. Hartmann, C. L. Bender, J. Sann, A. K. Durr, M. Jansen, J. Janek, P. Adelhelm, *Physical Chemistry Chemical Physics* 2013, 15, 11661.

Abbreviation and Symbols

List of Abbreviations

DSC	-	differential scanning calorimetry
CPE	-	constant phase element
EMF	-	electromotive force
EPR	-	electron paramagnetic resonance spectroscopy
FTIR	-	fourier transformed infrared spectroscopy
ICP-OES	-	inductive coupled plasma – optical emission spectroscopy
SEM	-	scanning electron microscope
XRD	-	x-ray diffraction

List of Symbols

A	-	surface area
a	-	activity
D_{eon}	-	electronic defect diffusivity
D_{ion}	-	ionic defect diffusivity
D^{δ}	-	chemical diffusion coefficient
D_{Knudsen}	-	Knudsen diffusion coefficient
ρ	-	density of the material
ρ_{theo}	-	theoretical density

F	-	Faraday constant
FWHM	-	full width half maximum
k^δ	-	chemical surface reaction rate constant
L	-	diffusion length
λ	-	wavelength
M	-	Molar mass
M_u	-	normalized voltage
Q_{flow}	-	gas flow rate
R	-	ideal gas constant
R_{eon}	-	electronic resistance
R_{ion}	-	ionic resistance
σ_{ac}	-	total bulk conductivity conductivity
σ_{eon}	-	electronic conductivity
σ_{ion}	-	ionic conductivity
τ_δ	-	chemical relaxation time
τ_{flush}	-	reactor flush time
t_{ion}	-	ionic transference number
t_{eon}	-	electronic transference number
T_m	-	melting point
$V_{reactor}$	-	reactor volume

W	-	Warburg diffusion resistance
χ_{eon}	-	electronic trapping factor
χ_{ion}	-	ionic trapping factor
z	-	number of electrons

Acknowledgements

I would like to thank Prof. Joachim Maier for giving me the opportunity to work in his group on this exciting topic as well as for his helpful suggestions in the course of this thesis. I would also like to thank to Prof. Joachim Bill and Prof. Joachim van Slageren for taking their time to be in my examination committee.

I am deeply grateful to Dr. Rotraut Merkle for her overwhelming support, countless suggestions, constructive discussions and for her proof-reading this thesis.

I would also like to thank Dr. Christian Schoen for his help as external supervisor, and Dr. Dominik Samuelis and Dr. Kiran Adepalli for their scientific discussions.

For their technical support, I would like to thank Armin Schulz (Raman spectroscopy), Friedrich Kögel (XRD), Wolfgang König (FTIR), Ewald Schmitt (DSC and metal machining), Annette Fuchs & Sebastian Stämmler (SEM), Albrecht Meyer & Gerhard Werner (ICP-OES), Peter Senk (Swagelok & tube furnaces), Udo Klock (mass flow controller), Uwe Traub (IT) as well the glass work shop, low temperature service, the metal workshop and the crystal preparation group of the Max Planck-Institutes in Stuttgart.

Curriculum Vitae

Personal information

Name: Oliver Gerbig
Date of birth: 27.02.1983
Place of birth: Darmstadt (Germany)

Education

10/2005 – 10/2009 Diploma of Engineering in Material Science
Technische Universität Darmstadt
1/2010 – 3/2014 PhD in Chemistry
Max Planck Institute for Solid State Research in
Stuttgart in the department of Prof. Maier

Publications

- O. Gerbig, R. Merkle, J. Maier, Electron and Ion Transport In Li_2O_2 , Advanced Materials, Volume 25, Issue 22, pages 3129 - 3133.
- A. Kuhn, O. Gerbig, C. Zhu, F. Falkenberg, J. Maier, B.V. Lotsch, Ultrafast Li Electrolytes Based on Abundant Elements: $\text{Li}_{10}\text{SnP}_2\text{S}_{12}$ and $\text{Li}_{11}\text{Si}_2\text{PS}_{12}$, Phys. Chem. Chem. Phys. 2014, 16, 14669–14674.